DYNAMIC ANALYSIS OF GRID-FOLLOWING VSCS UNDER GRID FAULTS

Wang, Xinshuo

DOI (link to publication from Publisher):
10.54337/aau561826513

Publication date:
2023

Document Version
Publisher's PDF, also known as Version of record

DYNAMIC ANALYSIS OF GRID-FOLLOWING VSCS UNDER GRID FAULTS

BY
XINSHUO WANG

DISSERTATION SUBMITTED 2023

AALBORG UNIVERSITY
DENMARK

DYNAMIC ANALYSIS OF GRID-FOLLOWING VSCS UNDER GRID FAULTS

by

Xinshuo Wang

AALBORG UNIVERSITY
DENMARK

Dissertation submitted 2023

Dissertation submitted: July 2023

PhD supervisor:: Prof. Xiongfei Wang
Aalborg University, Denmark

Assistant PhD supervisor: Asst. Prof. Heng Wu
Aalborg University, Denmark

PhD committee: Associate Professor Amin Hajizadeh (Chairman)
Aalborg University

Professor Kai Strunz
Technical University of Berlin, Germany

Professor Pablo Garcia Fernandez
University of Oviedo, Spain

PhD Series: Faculty of Engineering and Science, Aalborg University

Department: AAU Energy

ISSN (online): 2446-1636
ISBN (online): 978-87-7573-669-0

Published by:
Aalborg University Press
Kroghstræde 3
DK – 9220 Aalborg Ø
Phone: +45 99407140
aauf@forlag.aau.dk
forlag.aau.dk

Printed in Denmark by Stibo Complete, 2023

ENGLISH ABSTRACT

Voltage-Source Converters (VSCs) have gained widespread usage in the integration of renewables into modern power systems. This thesis addresses the transient stability of VSCs during grid faults and the transient overvoltage during fault recovery, with a particular focus on the impact of widely used grid-following (GFL) control. The research work in this thesis is of importance for ensuring the secure and reliable operation of power systems, particularly considering the growing integration of VSC-based resources.

The first focus of this thesis is to assess the transient stability of GFL-VSCs during the fault ride-through (FRT) operation, taking into account the dynamics of voltage-dependent current injection (VDCI). To gain a deeper understanding of the effects of dynamic interactions between VDCI and the phase-locked loop (PLL) on the transient stability of GFL-VSCs connected to weak AC grids, a comprehensive analysis is performed. By incorporating the influence of VDCI, a static model is employed to investigate the existence of equilibrium points (EPs) during grid faults. Subsequently, a dynamic model is developed to assess the convergence capability of GFL-VSCs towards EPs during grid faults. The study reveals the impact of the *K*-factor that is resulted from the VDCI characteristic on the transient stability of the system.

Second, this thesis examines the effects of various reactive current injection modes (absolute and relative) on the transient stability of GFL-VSCs during FRT operations. To that end, the dynamic interaction between the current injection profile and the PLL is captured by the developed nonlinear model. The influences of these two current injection modes on the existences of EPs and the transient dynamics is then characterized based on the model. Additionally, to ensure the transient stability of the system, this study provides recommendations for selecting the reactive current injection modes.

Third, this thesis analyzes the transient overvoltage (TOV) phenomenon of GFL-VSCs during fault recovery. The mechanism of TOV is analyzed considering the slow and fast current reference update modes. The necessity of analyzing the influence of modulation saturation (MS) mode on TOV is also highlighted. For the fast current reference update mode, the extended TOV duration is identified, which is resulted from the current reference surge introduced by mode switching from full reactive current injection to VDCI. Then, the TOV mitigation method is developed.

DANSK ABSTRAKT

Voltage-Source Converters (VSC'er) har opnået omfattende anvendelse i integrationen af vedvarende energikilder i moderne kraftsystemer. Denne afhandling adresserer den transiente stabilitet af VSC'er under netfejl og den transiente overspænding under fejlretning, med særlig fokus på virkningen af den almindeligt anvendte grid-following (GFL) kontrol. Forskningsarbejdet i denne afhandling er vigtigt for at sikre sikker og pålidelig drift af kraftsystemer, især med henblik på den voksende integration af VSC-baserede ressourcer.

Det første fokus i denne afhandling er at vurdere den transiente stabilitet af GFL-VSC'er under fejlride-through (FRT) drift, med inddragelse af dynamikken i spændingsafhængig strøminjektion (VDCI). For at opnå en dybere forståelse af virkningerne af dynamiske interaktioner mellem VDCI og phase-locked loop (PLL) på den transiente stabilitet af GFL-VSC'er forbundet til svage vekselstrømsnet udføres en omfattende analyse. Ved at inkorporere indflydelsen af VDCI anvendes en statisk model til at undersøge eksistensen af ligevægtspunkter (EP'er) under netfejl. Derefter udvikles en dynamisk model til at vurdere konvergenskapaciteten af GFL-VSC'er mod EP'er under netfejl. Studiet afslører virkningen af K-faktoren, som er resultatet af VDCI-karakteristikken, på den transiente stabilitet af systemet.

For det andet undersøger denne afhandling virkningerne af forskellige reaktive strøminjektionsmetoder (absolutte og relative) på den transiente stabilitet af GFL-VSC'er under FRT-drift. For at opnå dette fanges den dynamiske interaktion mellem strøminjektionsprofilen og PLL'en af den udviklede ikke-lineære model. Virkningerne af disse to strøminjektionsmetoder på eksistensen af EP'er og den transiente dynamik karakteriseres derefter ud fra modellen. Derudover giver denne afhandling anbefalinger til valg af reaktive strøminjektionsmetoder for at sikre den transiente stabilitet af systemet.

For det tredje analyserer denne afhandling fænomenet transient overspænding (TOV) af GFL-VSC'er under fejlretning. Mekanismen for TOV analyseres med henblik på de langsomme og hurtige opdateringsmetoder til strømreferencer. Nødvendigheden af at analysere indflydelsen af metode til modulationsmætning (MS) på TOV fremhæves også. For den hurtige opdateringsmetode til strømreferencer identificeres den forlængede TOV-varighed, som skyldes strømreferencetoppen introduceret ved skift fra fuld reaktiv strøminjektion til VDCI. Derefter udvikles en metode til at minds TOV.

ACKNOWLEDGEMENTS

This PhD project was carried out in AAU Energy, Aalborg University, Denmark.

First, I would like to express my sincere gratitude to my PhD supervisor, Prof. Xiongfei Wang, for your unwavering patience and professional guidance in me as a struggling PhD student. Throughout the past four years, I vividly recall the challenging period when you initially supervised my PhD project. You generously dedicated your time to enhancing my foundational knowledge and cultivating my research skills to meet rigorous standards. I believe your guidance during my PhD study will have a lifelong impact on me. Furthermore, during moments of anxiety and confusion, you consistently demonstrated concern for my well-being, providing various forms of support that greatly encouraged me to confront and overcome challenges.

Second, I would like to extend my appreciation to my PhD co-supervisor, Asst. Prof. Heng Wu, for your professional guidance and patience throughout my PhD studies. In our regular discussion, I have learned a great deal about critical thinking methodologies from you. Whenever I encountered technical challenges, you consistently emphasized the importance of solving problems step by step through rational thinking, rather than relying on guesswork or assumptions. This guidance has deepened my understanding of the process of producing research outcomes. As a PhD student, I gradually recognize the enhancement of thinking abilities holds greater significance than solely pursuing technological breakthroughs, as thinking and logic gradually steer the realization of technology.

I would also like to express my gratitude to the members of the eGrid research group at AAU Energy. It has been a great honor to be a part of such a formidable research group throughout my PhD studies. While I may not have had sufficient time for in-depth discussions with all of you, I found great inspiration from your presentations during our group meetings. I want to thank the colleagues and staffs at AAU Energy for their assistance with practices throughout my PhD studies.

Finally, I would like to thank my family, whose selfless dedication and unwavering love served as a constant source of inspiration, motivating me to persevere through the challenges of my PhD studies.

Xinshuo Wang
Aalborg University, June 2023

TABLE OF CONTENTS

LIST OF ABBREVIATIONS

A

ac-side voltage control
AVC 17
alternative current
ac 17

C

current source
CS 65

D

dc-side voltage control
DVC 17
direct current
dc 17

E

electromagnetic transient
EMT 21
Equal Area Criterion
EAC 12
equilibrium point
EP 12

F

fault ride-through
FRT 9
full-reactive current injection
FRCI 15

G

grid-following
GFL 9
grid-forming
GFM 9

H

high voltage direct current
HVDC 14

L

line commutated converter
LCC 15
loss of synchronization
LOS 10
low-pass filter
LPF 54

M

modular multilevel converter
MMC 14
modulation saturation
MS 15

N

North American Electric Reliability Corporation
NERC 9

P

phase-locked loop
PLL 9
point of connection
PoC 12
proportional-integral controller
PI controller 66

R

rate of change of the current reference
ROCOCR 65
reactive current injection

S

T

U

V

CHAPTER 1. INTRODUCTION

1.1. BACKGROUND AND CHALLENGES

1.1.1. CHALLENGES OF VSC-DOMINATED POWER SYSTEM

With the ongoing transition towards a low-carbon energy system, the integration of renewable energy resources such as wind and solar power into power systems has witnessed a significant rise [1]-[43]. This integration is facilitated by the utilization of voltage source converters (VSCs) . Consequently, the contemporary power system is experiencing a fundamental transformation from the traditional dominance of synchronous generators (SGs) to a system where converters play a prominent role, as depicted in Figure 1.1 [1]-[43]. The dynamics of VSCs differ from SGs as they are primarily influenced by their control algorithms rather than swing dynamics. This characteristic of VSCs allows for enhanced control flexibility and faster dynamic responses. However, the wide-timescale control dynamics of VSCs may interact with power system dynamics, resulting in system oscillations over a wide frequency range [1]-[43]. Hence, the dynamic analysis of VSC-based power system is crucial for its secure and reliable operation.

Two fundamental control strategies are employed for VSCs, namely grid-forming (GFM) and grid-following (GFL) control [6], [7], [10], [12], [23], [46], [47], [52]. The former operates VSC as a voltage source and utilizes the active power control for grid synchronization [6], [7], [10], [12], [23]. The latter controls the VSC as a current source and synchronizes it with the power grid using the phase-locked loop (PLL) technique [12], [46], [47], [52]. Despite a growing interest in developing GFM control in recent years, most of today's commercial VSCs still adopt GFL control. Therefore, this thesis aims to focus on the dynamics analysis of the GFL-VSCs.

In recent years, there has been significant research on small-signal stability of GFL-VSCs. [44]-[45]. However, the investigation of the dynamic behavior of GFL-VSCs during large grid disturbances, such as grid faults, remains an actively developing area. Further, grid codes are also continually evolving with specific requirements on fault ride-through (FRT) of GFL-VSCs [72]-[73], [75]-[76]. The grid code requirement on the FRT has a critical impact on the reliability of VSC-based systems, as evidenced by recent real-world incidents of tripping VSCs during grid faults [48]-[49], [111]-[113]. For example, the North American Electric Reliability Corporation (NERC) has reported a significant reduction in the active

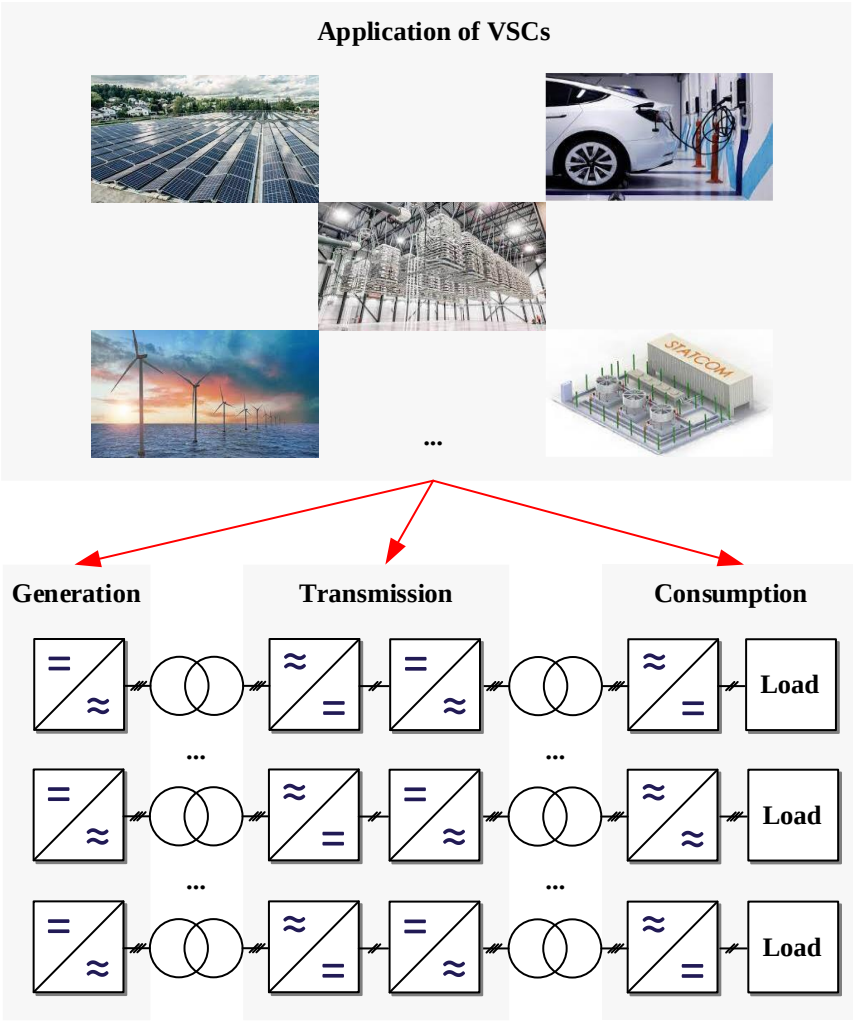

Figure 1.1. Converter-based power system. Source: [1].

power output from solar power plants due to the trip of GFL-VSCs during grid faults [111]. The causes of such VSC tripping have been further investigated therein, and the results are given in Table 1.1 and Figure 1.2 [111]. The loss of synchronization (LOS) and transient overvoltage (TOV) contribute most to the trip of GFL-VSCs. To tackle the challenges, this thesis performs a large-signal dynamics analysis of GFL-VSC from the perspective of grid code compliance. More specifically, the focus of this thesis is to examine the transient stability of GFL-VSCs under grid faults, as well as investigate the TOV phenomena during fault recovery.

Table 1.1. Causes of generation reduction during a disturbance: Detailed capacity reduction and its root causes. Source: [111].

Cause of Reduction	Reduction [MW]
PLL Loss of Synchronism	389
Inverter AC Overvoltage	269
Momentary Cessation	153
Feeder AC Overvoltage	147
Unknown	51
Inverter Underfrequency	48
Not Analyzed	34
Feeder Underfrequency	21

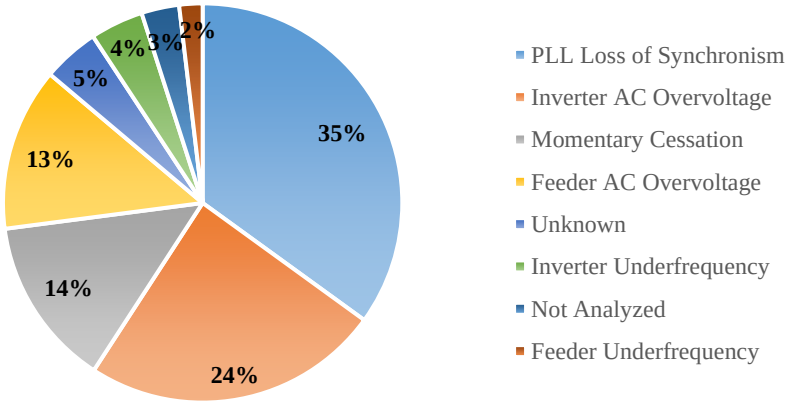

Figure 1.2. Causes of generation reduction during a disturbance: Percentage of each cause. Source: [111].

1.1.2. STATE-OF-THE-ART

1.1.2.1 Transient Stability Analysis of GFL-VSCs

In the context of GFL-VSCs, a PLL is commonly employed as a dedicated unit for synchronizing the converters with the voltage at their point of connection (PoC) [53]. The transient stability of a GFL-VSC refers to its capability to maintain synchronism with the power grid despite large disturbances like grid faults, loss of generator, or large load swing [54]. The first focus of this thesis is to investigate the transient stability of GFL-VSCs during grid faults, which is essential for the effective FRT operation [52]. In weak grids with low short-circuit ratio (SCR), the PoC voltage that is used as the input of PLL is prone to being influenced by the injected current [55]. As a result, the transient stability of GFL-VSCs during grid faults can be affected by both the injected current and the PLL dynamics, especially in low SCR grids [52].

The assessment of transient stability in GFL-VSCs typically encompasses a two-step process.

- The first step is to evaluate the existences of stable equilibrium points (SEPs) [55], [86], [89]. This is a necessary condition for GFL-VSCs to maintain stable operating points during faults [55], [86], [89].
- The subsequent step involves examining the transient dynamics of GFL-VSCs. This implies whether the system can reach SEPs during the transient process [56], [57]. The transient dynamics of the system are influenced by both the initial conditions and the controller parameters of VSCs [58]-[71], [78]-[110].

The existence of equilibrium points (EPs) in GFL-VSCs during grid faults is contingent upon the properties of the grid impedance and current injection profile [55], [60]. Verification of the existence of EPs in GFL-VSCs during grid faults can be achieved by deriving the steady-state solutions of system dynamical model, as evidenced in previous studies [55], [60], [61]. However, the existence of EPs alone does not guarantee the transient stability of GFL-VSCs. It is necessary to conduct further investigate the capability of VSC to converge to these EPs, considering the influence of the PLL dynamics [62]-[65].

In recent years, there has been an increasing research focus on examining the dynamic influence of the PLL on the transient stability of GFL-VSCs [57], [62], [63], [65], [67], [68], [78]-[85], [87]. While the Equal Area Criterion (EAC) has traditionally been utilized to evaluate the transient stability of SGs, its application has extended to the analysis of transient dynamics in GFL-VSCs due to its intuitive physical insights, as demonstrated in previous works [62], [63], [65], [78]-[85]. However, in the application of the EAC, the proportional gain (K_p) of the PLL is

often overlooked, resulting in conservative stability predictions [62], [63]. To address this issue, the proposed EAC method in [80] and [82] considers the effect of K_p. [65] and [81] considers both the impact of K_p and integral gain (K_i) from the perspective of dynamic damping term and is found out that this term could be positive or negative damping based on operating regions. Operating the GFL-VSC within the positive damping region is recommended to improve the transient stability of the system [65]. Nevertheless, it is worth noting that GFL-VSCs possess the capability to achieve stability even in the negative damping region. Thus, while the positive-damping-based stability prediction offers improved accuracy compared to conventional EAC methods, it still exhibits a certain level of conservatism [65]. A method proposed in [84] fully considers the effects of positive and negative damping in the EAC method, leading to a reduction in conservativeness compared to conventional methods. In addition, the phase portrait has been reported in [57], [87] and [88] for more accurate transient stability analysis, providing numerical solutions to the nonlinear differential equations, but offering limited insights for PLL parameter tuning. To offer specific design guidelines for improving transient stability using PLL, researchers have made various efforts to obtain analytical solutions for the system that consider the nonlinear dynamics of the PLL [67], [68]. In a study conducted by [67], the stability boundaries of the system were determined by analytically calculating them using the Taylor-series expansion method, considering various PLL parameters. Analytical insights into the stability margin are obtained using the Hamilton stability criterion in [68].

The existing body of research on transient stability in GFL-VSCs has primarily concentrated on a fixed current injection profile during grid faults, which might not align with grid code stipulations [72]. An important requirement, as stated in [72], involves adapting the reactive current injection dynamically in response to the magnitude of the PoC voltage during FRT, i.e., voltage-dependent current injection (VDCI) [72]. Weak grid conditions with low SCR amplify the sensitivity of the PoC voltage to injected currents due to larger grid impedance. This voltage influence extends beyond PLL synchronization and necessitates the redistribution of current references to adhere to grid code specifications. Consequently, the interaction between VDCI and PLL, which plays a crucial role in the system, significantly influences the analysis of transient stability. However, previous studies have given limited attention to this aspect.

In practical applications, VDCI is typically classified into two modes: absolute reactive current injection (A-RCI) and relative reactive current injection (R-RCI) [72], [73], [76]. These modes display variations in the reactive current bias on the FRT curve [72], [73], [76]. Nevertheless, the current literature lacks investigation into the influence of this bias on the transient stability of GFL-VSCs.

Research gap for this topic can be summarized as follows:

Research Gap 1 Most existing studies on transient stability of GFL-VSCs assumed a fixed current injection during grid faults [64]-[70], [78]-[110]. However, existing grid codes require VDCI [72], [73]. The systematic transient stability analysis under such case is still missing [J1], [C1].

Research Gap 2 The transient stability of GFL-VSCs under various VDCI modes, specifically A-RCI and R-RCI mode, has not yet been studied in relation to the impact of reactive current bias [C2].

1.1.2.2 Transient Overvoltage (TOV) Analysis of GFL-VSCs

In scenarios involving weak grids with high impedance, the voltage at the PoC of GFL-VSCs exhibits increased vulnerability to the injected current. This vulnerability can result in reduced voltage stiffness at the PoC. This may increase the risk of transient overvoltage (TOV) during fault recovery, which has been reported as a leading cause of the tripping of GFL-VSCs [111]-[113].

In recent years, many research efforts have been directed towards understanding and mitigating TOV of grid-connected devices [114]-[125].

The occurrence of TOV in grid-connected devices has garnered significant attention in recent research. Studies have emphasized that improper injection of reactive current or power can induce TOV, as evidenced by several works [114], [115], [118], [120]-[125]. It is widely recognized that the provision of adequate capacitive-reactive current or power from grid-connected devices can effectively support the voltage at the PoC, particularly during grid voltage sags [114], [115], [118], [120]-[125]. However, during the recovery phase of grid faults, an excessive injection of capacitive-reactive current or power can lead to surplus support to the PoC voltage, resulting in TOV. In addition to improper reactive power injection, the slow recovery of active power has also been identified as a contributing factor to TOV, as demonstrated through circuit equations in [115]. Furthermore, the modulation reference of voltage source converters (VSCs) can influence TOV. Specifically, saturation of the *d*-axis modulation reference in the converter station of a modular multilevel converter-VSC-high voltage direct current (HVDC) transmission-based wind power integration system has been found to contribute to TOV at the connection point during fault recovery [116]. Another aspect influencing TOV is the load property. Inadequate capacity ratio between generation from GFL-VSCs and the load under off-grid mode, caused by a grid fault, has been reported to induce TOV [117]. Additionally, inadequate properties of the passive load in a current-controlled standalone inverter during fault recovery can lead to TOV due to poor voltage overshoot performance [119]. Lastly, control delay can trigger TOV. The voltage detection delay in a wind farm has been identified as a cause of inadequate power reference generation during fault recovery, resulting in surplus injection of capacitive-reactive power and subsequent TOV [125].

To mitigate TOV, various strategies have been proposed in the existing literature. [115] presents a coordinated operation strategy involving wind turbines and reactive power compensation devices during fault recovery to achieve TOV mitigation through appropriate injection of capacitive-reactive power. [114] proposes the limitation of the *d*-axis control signal of a line commutated converter (LCC) to mitigate TOV. [116]-[117] propose TOV mitigation methods by limiting the modulation reference of VSCs. [119] proposes a parallel virtual impedance control in standalone inverter to improve voltage overshoot performance at the load side for TOV mitigation. [125] introduces an algorithm for delay improvement in wind farm control to mitigate TOV.

In the context of GFL-VSCs with different control mode, i.e., VDCI mode and full-reactive current injection (FRCI) mode , the update of current references can experience delays due to the implementation of a voltage magnitude detection filter (VMDF) with varying bandwidth during dynamics. Specifically, during fault recovery, the delayed update of current references can result in excessive capacitive-reactive current injection, potentially leading to TOV at the PoC. However, this scenario arises only when the output current of GFL-VSCs is under control. In practice, the voltage swell occurring during fault recovery, as a large disturbance, may trigger the modulation limiter, which imposes restrictions on the tracking of current references. Consequently, it becomes crucial to undertake a systematic investigation that incorporates the impact of modulation saturation (MS) mode in GFL-VSCs under different speed of current reference update. The existing literature lacks such comprehensive analysis and understanding of this aspect.

Research gap for this topic can be summarized as follows:

Research Gap 3 Limited investigation has been undertaken to delve into the impact of MS on TOV analysis of GFL-VSCs during grid fault recovery. The effect of different speed of current reference update on TOV during MS mode is also not well understood. The upper boundary of TOV during MS mode also need to be calculated to predict the severity of TOV.

1.2. RESEARCH QUESTIONS AND OBJECTIVES

Several research questions and corresponding objectives can be formulated in Table 1.2 based on the research gaps identified in section 1.1.

Table 1.2. Research questions and objectives. Source: [J1], [C1], [C2], [C3].

Research Questions	Research Objectives
Q1. How will the VDCI requirement affect the transient stability of GFL-VSCs during grid faults?	Develop a large-signal model of GFL-VSC, encompasses the dynamics of both VDCI and PLL.
	Clarify the influence of VDCI on the existence of EPs.
	Evaluate the dynamic trajectory of the GFL-VSC system and elucidate the parametric effect of VDCI and PLL on the transient stability of GFL-VSC.
Q2. What are the impacts of different reactive current injection modes on the transient stability of GFL-VSCs?	Develop a large-signal model of GFL-VSC system accounting for the different reactive current injection modes.
	Identify the influences of reactive current injection modes on the existences of EPs
	Compute the dynamic trajectory of the system and analyze the effect of reactive current injection modes on the transient dynamics of GFL-VSCs.
	Provide recommendation on the selection of reactive current injection mode (R-RCI or A-RCI) from the perspective of transient stability.

Table 1.2. Research questions and objectives, continued. Source: [J1], [C1], [C2], [C3].

Research Questions	Research Objectives
Q3. How to analyze the TOV of GFL-VSCs during fault recovery considering different control (VDCI and FRCI mode) and operation (MS mode) modes?	Quantify the upper boundary of the TOV at the PoC of GFL-VSCs under MS mode.
	Elaborate the effect of slow and fast update of current reference on dynamics of PoC voltage during fault recovery under MS mode.
	Develop TOV mitigation strategy.

1.3. PROJECT LIMITATIONS

The limitations in this PhD project can be listed as follows.

- The focus of this PhD project is on the the current control loop and PLL of the GFL-VSC during FRT scenarios. Specifically, the investigations are limited to severe grid voltage sags. Under such conditions, the primary objective of GFL-VSCs is to provide FRT functionality by injecting reactive current to support the voltage at PoC [72], [73]. Consequently, the outer control loops, including power control, dc-side voltage control (DVC), and ac-side voltage control (AVC), are typically disabled during severe grid voltage sags [57]. However, it is worth noting that the impact of the outer control loops may become significant in cases of non-severe grid voltage sags [126], which exceed the scope of this thesis.
- This PhD project focuses on investigating the transient behavior within the infinite grid bus scenario, which assumes a simplified representation of the grid as an ideal voltage source connected in series with an impedance. However, it is crucial to acknowledge that practical grids encompass a multitude of components, such as SGs, GFM- and GFL-VSCs. These additional components introduce greater complexity to the dynamics of the grid, making the analysis of transient behavior significantly more intricate. Consequently, providing clear and definitive insights becomes more challenging due to the increased complexity arising from the existence of these diverse grid elements.

1.4. STRUCTURE OF THE THESIS

The structure of this thesis is presented in Table 1.3.

Table 1.3. Structure of the thesis. Source: [J1], [C1], [C2], [C3].

Chapters	Title	Main Content	Corresponding Publications
1	Introduction	Background and challenges	
		Research questions and objectives	
		Project limitations	
		Structure of the thesis	
		List of publications	
2	Transient Stability Analysis of GFL-VSCs Considering VDCI	Introduction	[J1] [C1]
		System description	
		Analysis of EPs	
		Analysis of transient dynamics	
		Case studies and discussion	
		Summary	
3	Impact of Reactive Current Injection Modes on Transient Stability of Grid-Following VSCs	Introduction	[C2]
		Analysis of EPs	
		Analysis of transient dynamics	

Table 1.3. Structure of the thesis, continued. Source: [J1], [C1], [C2], [C3].

Chapters	Title	Main Content	Corresponding Publications
3	Impact of Reactive Current Injection Modes on Transient Stability of Grid-Following VSCs	Case studies and discussion	[C2]
		Summary	
4	TOV Analysis of Grid-Following VSCs during Fault Recovery	Introduction	[C3]
		System description	
		TOV analysis	
		Summary	
5	Conclusions and future works	Summarize contribution of the thesis and provide future works	

1.5. LIST OF PUBLICATIONS

Journal paper:

[J1] X. Wang, H. Wu, X. Wang, L. Dall, and J. B. Kwon, "Transient stability analysis of grid-following VSCs considering voltage-dependent current injection during fault ride-through," in *IEEE Trans. Energy Convers.*, vol. 37, no. 4, pp. 2749-2760, Dec. 2022.

Conference paper:

[C1] X. Wang, H. Wu, X. Wang, L. Dall, and J. B. Kwon, "Dynamic impact of voltage-dependent current injection on fault-ride-through of grid-following converters," in *Proc. 2021 IEEE Energy Conversion Congress and Exposition (ECCE)*, Vancouver, BC, Canada, 2021, pp. 369-374.

[C2] X. Wang, H. Wu, and X. Wang, "Impact of reactive current injection modes on transient stability of grid-following VSCs during fault ride-through," in *Proc. 2022 IEEE 13th International Symposium on Power Electronics for Distributed Generation Systems (PEDG)*, Kiel, Germany, 2022, pp. 1-7.

[C3] X. Wang, H. Wu, and X. Wang, “Transient overvoltage analysis of grid-following VSCs during fault recovery,” in *Proc. 2023 International Conference on Power Electronics (ICPE 2023-ECCE Asia)*, Jeju, Korea, 2023, pp. 1-6.

CHAPTER 2. TRANSIENT STABILITY ANALYSIS OF GFL-VSCS CONSIDERING VDCI

2.1. INTRODUCTION

Despite the considerable amount of research dedicated to the transient stability of GFL-VSCs, most existing studies have focused on the assumption of a fixed active/reactive current injection profile during grid faults, which may not align with the requirements outlined in the grid code [72], [73]. An example of such considerations is the VDCI requirement specified in [72], which necessitates the dynamic adjustment of the reactive current injected by GFL-VSCs during FRT in accordance with the detected magnitude of the PoC voltage. In scenarios characterized by weak grid conditions, the voltage at the PoC exhibits a high sensitivity to the active and reactive currents injected, owing to the voltage drop across the grid impedance [J1], [C1]. The impact of the affected PoC voltage extends beyond the synchronization dynamics of the PLL, as it also necessitates the redistribution of active and reactive current references in accordance with the requirements outlined in the grid code [J1], [C1]. The redistribution of the current reference, coupled with the output phase angle of the PLL, further introduces updates to both the injected current profile and the dynamics of the PoC voltage [J1], [C1]. Therefore, the dynamic interaction between VDCI and PLL plays a pivotal role in the transient stability analysis of GFL-VSCs; however, it has been largely overlooked in previous investigations [J1], [C1]. The study conducted in [73] investigated the influence of VDCI dynamics on the FRT performance of GFL-VSCs through electromagnetic transient (EMT) simulations. While the study in [73] made contribution in this area, its reliance on simulation-based observations limited its generalizability and analytical insights, rendering the findings case-specific.

This chapter presents the study conducted in [J1] and [C1] that specifically focus on addressing the challenge of analyzing the impact of VDCI on transient stability of GFL-VSCs during FRT. An analytical model is developed in this study, incorporating the dynamics of both PLL and VDCI during symmetrical grid faults [J1], [C1]. The developed model is subsequently employed to examine the existence of EPs and analyze the transient dynamics of the system, placing emphasis on the *K*-factor, which governs the nature of VDCI [J1], [C1]. The range of acceptable *K*-factor values is further determined to ensure the transient stability [J1], [C1]. Ultimately, the theoretical analysis is validated through time-domain simulations and experiments.

2.2. SYSTEM DESCRIPTION

Figure 2.1 illustrates the employed control scheme in the GFL-VSC. The implementation of a single-loop current control strategy ensures accurate tracking of the current reference (I_{refdq}) during transient dynamics. The PoC and grid voltage are represented by v_c and v_g, respectively [J1], [C1]. V_{cm} and V_{gm} represent the magnitudes of these two voltages [J1], [C1]. The filter inductance is denoted as L_f, while the grid inductance and grid resistance are represented by L_g and R_g, respectively [J1], [C1]. The synchronization of the VSC with the power grid is achieved through the utilization of a dedicated synchronization unit, referred to as the synchronous reference frame PLL (SRF-PLL) [74], as depicted in Figure 2.2 [J1], [C1]. The nominal grid frequency is denoted as ω_g, while the frequency deviation ($\Delta\omega$), output phase angle (θ_{PLL}), and output frequency (ω_{PLL}) of the PLL are also presented in Figure 2.2 [J1], [C1]. The parameter K_p represents the proportional gain of the PLL controller, while K_i represents the integral gain of the PLL controller [J1], [C1].

The control strategy employed by the GFL-VSC during steady-state operation prior to the occurrence of a grid fault involves injecting the active current with rated value (I_{lim}) and zero reactive current, i.e., I_{refd} (active current reference) = I_{lim} and I_{refq} (reactive current reference) = 0. In this study, the grid fault scenario is emulated by introducing a voltage sag from the grid side, resulting in a decreased voltage at the PoC. Several existing grid codes [72], [75] mandate the injection of capacitive-reactive current by the VSC to compensate the decreased PoC voltage. This capability, known as FRT functionality, prevents the VSC from tripping during grid faults. The magnitude of the injected reactive current needs to be dynamically regulated in accordance with V_{cm} [J1], [C1]. Figure 2.3 (a) depicts two FRT curves exhibiting different K-factors, which dictate the slope of the FRT curve and are typically chosen within the range of 0 to 10 [73], [75], [76]. During FRT, the active current is also regulated by vector limitation to prevent overcurrent. Hence, I_{refdq} during FRT is calculated using (2.1) and (2.2) [76]. In Figure 2.3 (a), the solid dot signifies a potential operating point observed during FRT, denoting V_{cm0} as the nominal magnitude of the PoC voltage [J1], [C1].

$$I_{refq} = \begin{cases} \min\left[\dfrac{KI_{lim}}{V_{cm0}}\left(V_{cm}-V_{cm0}\right),\ I_{lim}\right] \\ \text{when}\left(V_{cm}-V_{cm0}\right)>0 \\ \max\left[\dfrac{KI_{lim}}{V_{cm0}}\left(V_{cm}-V_{cm0}\right),\ -I_{lim}\right] \\ \text{when}\left(V_{cm}-V_{cm0}\right)<0 \end{cases} \tag{2.1}$$

$$I_{\mathrm{refd}} = \sqrt{I_{\mathrm{lim}}{}^2 - I_{\mathrm{refq}}{}^2} \tag{2.2}$$

Figure 2.3 (b) depicts the vector diagram of the VSC-grid system while undergoing FRT [J1], [C1]. The angle between I_{refd} and I_{ref} is defined as θ_{FRT}, i.e., $\theta_{\mathrm{FRT}}=-\arctan(I_{\mathrm{refq}}/I_{\mathrm{refd}})$ [J1], [C1]. Additionally, the power angle δ is defined as the angle between θ_{PLL} and that of the grid voltage (θ_{g}), i.e., $\delta=\theta_{\mathrm{PLL}}-\theta_{\mathrm{g}}$ [J1], [C1].

Considering the substantial difference in bandwidth between the current control loop and the PLL, it is reasonable to assume the ideal current reference tracking, i.e., $I_{\mathrm{gdq}}=I_{\mathrm{refdq}}$ [66]. By adopting this assumption, the VSC can be regarded as a regulated current source. The magnitude of the current source is dictated by vector current limitation, while the phase angle is governed by both the PLL and VDCI, as depicted in Figure 2.4 [J1], [C1].

The interaction between the VSC and the grid offers a clear comprehension of the system's synchronization dynamics, which is elaborated below [J1], [C1]. As previously mentioned, during FRT, I_{refdq} is modified according to (2.1) and (2.2). The injection of active and reactive current subsequently influences the voltage drop across the grid impedance, which in turn impacts V_{cm} and redistributes I_{refdq} according to (2.1) and (2.2) [J1], [C1]. Moreover, the altered phase angle of v_{c} (θ_{vc}) further affects the synchronization dynamics of the PLL [J1], [C1]. These iterative responses persist until the system attains a stable or unstable state during FRT, as depicted in Figure 2.5 [J1], [C1].

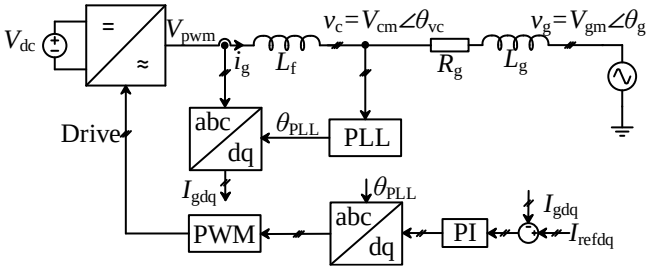

Figure 2.1. Control scheme of the GFL-VSC. Source: [J1].

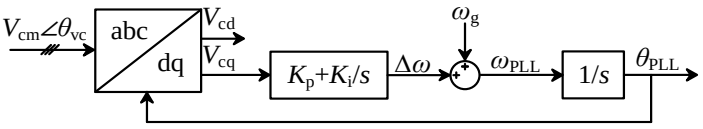

Figure 2.2. Control scheme of SRF-PLL. Source: [J1].

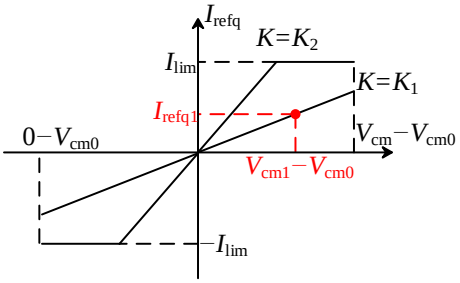

(a)

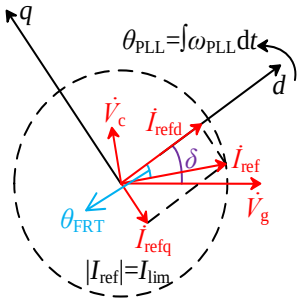

(b)

Figure 2.3. Current injection during FRT. (a) VDCI curves [74]. (b) Vector diagram. Source: [J1].

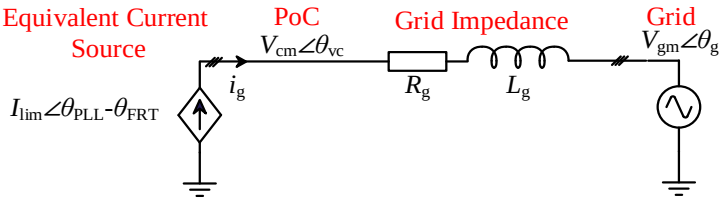

Figure 2.4. Equivalent VSC-grid system. Source: [J1].

2.3. ANALYSIS OF EPS

2.3.1. DERIVATION OF EPS

The EPs of the VSC-grid system refer to steady-state operating points where the current and voltage remain constant within the *dq* frame under grid fault conditions [J1], [C1].

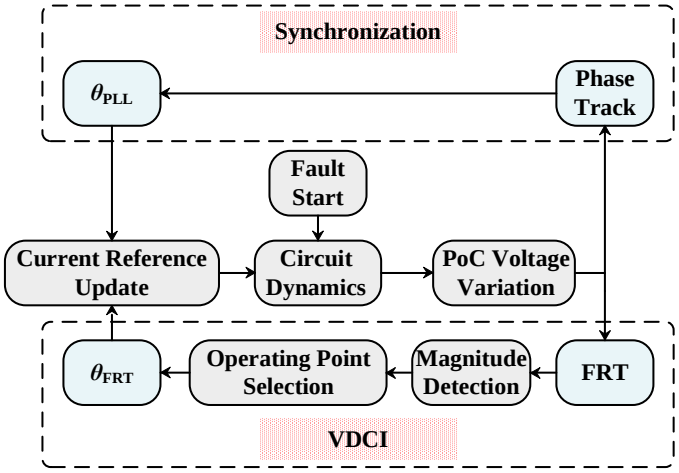

Figure 2.5. Synchronization dynamics affected by VDCI. Source: [J1].

Furthermore, at these EPs, ω_{PLL} converges to ω_g. The synchronization of the GFL-VSC with the grid is achieved by employing the PLL to regulate the *q*-axis component of the PoC voltage (V_{cq}) and maintain it at zero [55]. Consequently, the evaluation of EPs entails the voltage balance equation on *q*-axis, which is the focus of this subsection.

The expression of V_{cq}=0 can be formulated as (2.3) through the consideration of the voltage drop across the grid impedance (V_{gimq}) and grid voltage (V_{gq}) on *q*-axis [J1], [C1].

$$V_{cq} = V_{gimq} + V_{gq} = 0 \tag{2.3}$$

Subsequently, the expressions for V_{gimq} and V_{gq} can be further expanded in (2.4) and (2.5), respectively [J1], [C1].

$$V_{gimq} = I_{gd}\omega_g L_g + I_{gq}R_g = I_{lim}\cos\theta_{FRT}\omega_g L_g - I_{lim}\sin\theta_{FRT}R_g \tag{2.4}$$

$$V_{gq} = -V_{gm}\sin\delta \tag{2.5}$$

By substituting (2.4) and (2.5) into (2.3), a new expression (2.6) can be obtained [J1], [C1].

$$\underbrace{I_{lim}\cos\theta_{FRT}\omega_g L_g - I_{lim}\sin\theta_{FRT}R_g}_{V_{gimq}} \underbrace{-V_{gm}\sin\delta}_{V_{gq}} = 0 \tag{2.6}$$

(2.6) contains two unknown variables, namely δ and θ_{FRT}, making it impossible to determine their values using a single equation. Hence, to establish the relationship between δ and θ_{FRT}, it is necessary to derive it by considering the current reference generation method presented in (2.1) and (2.2). The detailed explanation of this relationship is presented below.

The PoC voltage in the $\alpha\beta$ frame can be represented by (2.7) and (2.8) [J1], [C1].

$$V_{c\alpha} = I_{\mathrm{lim}}\omega_{\mathrm{g}}L_{\mathrm{g}}\cos\left(\theta_{\mathrm{PLL}} - \theta_{\mathrm{FRT}} + \frac{\pi}{2}\right) + I_{\mathrm{lim}}R_{\mathrm{g}}\cos\left(\theta_{\mathrm{PLL}} - \theta_{\mathrm{FRT}}\right) + V_{\mathrm{gm}}\cos\left(\theta_{\mathrm{PLL}} - \delta\right) \tag{2.7}$$

$$V_{c\beta} = I_{\mathrm{lim}}\omega_{\mathrm{g}}L_{\mathrm{g}}\cos\left(\theta_{\mathrm{PLL}} - \theta_{\mathrm{FRT}}\right) + I_{\mathrm{lim}}R_{\mathrm{g}}\cos\left(\theta_{\mathrm{PLL}} - \theta_{\mathrm{FRT}} - \frac{\pi}{2}\right) + V_{\mathrm{gm}}\cos\left(\theta_{\mathrm{PLL}} - \delta - \frac{\pi}{2}\right) \tag{2.8}$$

By applying coordinate transformation to (2.7) and (2.8), the dq component of the PoC voltage can be obtained, as presented in (2.9) [J1], [C1].

$$\begin{pmatrix} V_{\mathrm{cd}} \\ V_{\mathrm{cq}} \end{pmatrix} = I_{\mathrm{lim}}\omega_{\mathrm{g}}L_{\mathrm{g}}\begin{pmatrix} \sin\theta_{\mathrm{FRT}} \\ \cos\theta_{\mathrm{FRT}} \end{pmatrix} + I_{\mathrm{lim}}R_{\mathrm{g}}\begin{pmatrix} \cos\theta_{\mathrm{FRT}} \\ -\sin\theta_{\mathrm{FRT}} \end{pmatrix} + V_{\mathrm{gm}}\begin{pmatrix} \cos\delta \\ -\sin\delta \end{pmatrix} \tag{2.9}$$

Then, V_{cm} can be expressed using (2.10) [J1], [C1].

$$V_{\mathrm{cm}} = \sqrt{V_{\mathrm{cd}}{}^2 + V_{\mathrm{cq}}{}^2} \tag{2.10}$$

(2.11) provides the expression for θ_{FRT}, considering the current reference generation method specified in (2.1) and (2.2) [J1], [C1].

According to (2.11), the variable θ_{FRT} is influenced by K-factor. To establish a relationship between δ and θ_{FRT}, (2.9) and (2.10) can be substituted into (2.11), as presented in (2.12). By solving the system of equations comprising (2.6) and (2.12), the EPs can be determined, with δ and θ_{FRT} serving as the two unknown variables [J1], [C1].

2.3.2. INFLENCE OF *K*-FACTOR ON THE EXISTENCE OF EPS

Obtaining an analytical solution for the EPs is complex since (2.12) is an implicit equation involving two unknown variables, δ and θ_{FRT}, posing a significant challenge [J1], [C1].

$$\theta_{\mathrm{FRT}}=\begin{cases}-\arctan\left(\dfrac{KI_{\mathrm{lim}}\left(\dfrac{V_{\mathrm{cm}}}{V_{\mathrm{cm0}}}-1\right)}{I_{\mathrm{lim}}\sqrt{1-\left[K\left(\dfrac{V_{\mathrm{cm}}}{V_{\mathrm{cm0}}}-1\right)\right]^2}}\right) \\ \text{when}-\dfrac{1}{K}V_{\mathrm{cm0}}<\left(V_{\mathrm{cm}}-V_{\mathrm{cm0}}\right)<\dfrac{1}{K}V_{\mathrm{cm0}} \\ -\dfrac{\pi}{2} \\ \text{when}\left(V_{\mathrm{cm}}-V_{\mathrm{cm0}}\right)\geq\dfrac{1}{K}V_{\mathrm{cm0}} \\ \dfrac{\pi}{2} \\ \text{when}\left(V_{\mathrm{cm}}-V_{\mathrm{cm0}}\right)\leq-\dfrac{1}{K}V_{\mathrm{cm0}}\end{cases} \tag{2.11}$$

Hence, an alternative graphical method is utilized to evaluate the EPs. Specifically, the intersection of the V_{gimq}-δ curve and $V_{\mathrm{gm}}\sin\delta$ curve, as designated in (2.6), is checked to determine the EPs. To obtain the V_{gimq}-δ curve, θ_{FRT} in (2.4) can be substituted with the result of (2.12), and the curve can be numerically determined.

The relationship between the V_{gimq}-δ curves, characterized by different K-factors, and the $V_{\mathrm{gm}}\sin\delta$ curve is depicted in Figure 2.6. Based on (2.4), the maximum value of V_{gimq} occurs when K=0, which corresponds to the scenario of injecting full active current [J1], [C1]. The maximum value of V_{gimq}, denoted as V_{gimqmax}, is derived as $I_{\mathrm{lim}}\omega_{\mathrm{g}}L_{\mathrm{g}}$ from (2.4) [J1], [C1]. Conversely, the minimum value of V_{gimq} is obtained when full capacitive-reactive current is injected ($K\rightarrow\infty$), and it can be expressed as $V_{\mathrm{gimqmin}}=-I_{\mathrm{lim}}R_{\mathrm{g}}$ [J1], [C1]. Industrial practice typically restricts K to the range of 0 to 10 [73], [75], [76]. Figure 2.6 illustrates the relationship between the V_{gimq}-δ curves and the K-factor, indicating that a higher K-factor leads to increased injection of capacitive-reactive current for a given magnitude dip in the PoC voltage, resulting in a decline in the curves [J1], [C1].

Figure 2.7 depicts the V_{gimq}-δ curve and the $V_{\mathrm{gm}}\sin\delta$ curve, where the SEP and unstable equilibrium point (UEP) can be identified based on their intersection. The SEP is denoted by solid dots, while the UEP is represented by open circles [J1], [C1]. It is important to emphasize that stable operation of the VSC-grid system can be ensured solely at the SEPs during grid faults, as reported in previous studies [57], [66].

Based on the previously presented formulation, it can be observed that the range of $V_{\mathrm{gm}}\sin\delta$ is restricted to $[-V_{\mathrm{gm}}, V_{\mathrm{gm}}]$, whereas the range of V_{gimq}-δ affected by the K-

$$\theta_{\mathrm{FRT}}=\begin{cases}-\arctan\left(\dfrac{K\left(\dfrac{\sqrt{\left(I_{\lim}\omega_{\mathrm{g}}L_{\mathrm{g}}\sin\theta_{\mathrm{FRT}}+I_{\lim}R_{\mathrm{g}}\cos\theta_{\mathrm{FRT}}+V_{\mathrm{gm}}\cos\delta\right)^{2}+\left(I_{\lim}\omega_{\mathrm{g}}L_{\mathrm{g}}\cos\theta_{\mathrm{FRT}}-I_{\lim}R_{\mathrm{g}}\sin\theta_{\mathrm{FRT}}-V_{\mathrm{gm}}\sin\delta\right)^{2}}}{V_{\mathrm{cm0}}}-1\right)}{\sqrt{1-\left[K\left(\dfrac{\sqrt{\left(I_{\lim}\omega_{\mathrm{g}}L_{\mathrm{g}}\sin\theta_{\mathrm{FRT}}+I_{\lim}R_{\mathrm{g}}\cos\theta_{\mathrm{FRT}}+V_{\mathrm{gm}}\cos\delta\right)^{2}+\left(I_{\lim}\omega_{\mathrm{g}}L_{\mathrm{g}}\cos\theta_{\mathrm{FRT}}-I_{\lim}R_{\mathrm{g}}\sin\theta_{\mathrm{FRT}}-V_{\mathrm{gm}}\sin\delta\right)^{2}}}{V_{\mathrm{cm0}}}-1\right)\right]^{2}}}\right) \\ \text{when}-\dfrac{1}{K}V_{\mathrm{cm0}}<\left(V_{\mathrm{cm}}-V_{\mathrm{cm0}}\right)<\dfrac{1}{K}V_{\mathrm{cm0}} \\ -\dfrac{\pi}{2} \\ \text{when}\left(V_{\mathrm{cm}}-V_{\mathrm{cm0}}\right)\geq\dfrac{1}{K}V_{\mathrm{cm0}} \\ \dfrac{\pi}{2} \\ \text{when}\left(V_{\mathrm{cm}}-V_{\mathrm{cm0}}\right)\leq-\dfrac{1}{K}V_{\mathrm{cm0}}\end{cases} \tag{2.12}$$

factor is limited to $[-I_{\lim}R_{\mathrm{g}}, I_{\lim}\omega_{\mathrm{g}}L_{\mathrm{g}}]$. Hence, an inappropriate value for the K-factor may lead to a failure in the intersection of the V_{gimq}-δ and $V_{\mathrm{gm}}\sin\delta$ curves, consequently causing the loss of equilibrium points (EPs). Specifically, four possible scenarios may arise:

- **Scenario 1**. When the inequality $-V_{\mathrm{gm}}<-I_{\lim}R_{\mathrm{g}}<I_{\lim}\omega_{\mathrm{g}}L_{\mathrm{g}}<V_{\mathrm{gm}}$ is satisfied, the V_{gimq}-δ curve intersects with the $V_{\mathrm{gm}}\sin\delta$ curve across the entire range of K-factor values from 0 to $+\infty$, as depicted in Figure 2.8(a) [J1]. As a result, the system consistently exhibits EPs during grid faults [J1].
- **Scenario 2**. When the inequality $-V_{\mathrm{gm}}<-I_{\lim}R_{\mathrm{g}}<V_{\mathrm{gm}}<I_{\lim}\omega_{\mathrm{g}}L_{\mathrm{g}}$ is fulfilled, the intersection between the V_{gimq}-δ curve and the $V_{\mathrm{gm}}\sin\delta$ curve persists, even as the K-factor approaches $+\infty$ [corresponds to $V_{\mathrm{gimq}}=-I_{\lim}R_{\mathrm{g}}$] [J1]. However, there exists a lower limit of K-factor ($K_{\min}$) below which the intersection of $V_{\mathrm{gm}}\sin\delta$ and V_{gimq}-δ curves is not guaranteed, as illustrated in Figure 2.8 (b) [J1].

- **Scenario 3**. When the inequality $-I_{lim}R_g<-V_{gm}<I_{lim}\omega_g L_g<V_{gm}$ is satisfied, the intersection between the V_{gimq}-δ curve and the $V_{gm}\sin\delta$ curve occurs specifically at K=0 [corresponds to $V_{gimq}=I_{lim}\omega_g L_g$] [J1]. Nonetheless, there exists an upper limit of K-factor (K_{max}) above which the intersection of $V_{gm}\sin\delta$ and V_{gimq}-δ curves is not guaranteed, as illustrated in Figure 2.8 (c) [J1].
- **Scenario 4**. When the inequality $-I_{lim}R_g<-V_{gm}<V_{gm}<I_{lim}\omega_g L_g$ is satisfied, the existence of EPs is ensured by considering both the upper and lower limits of K-factors [J1]. This scenario is depicted in Figure 2.8 (d) [J1].

Therefore, apart from scenario 1, the existence of EPs is subject to constraints on the K-factor.

2.4. ANALYSIS OF TRANSIENT DYNAMICS

The existence of EPs serves as a prerequisite for ensuring the transient stability of the system [J1], [C1]. Even if the EPs exist, the ability of the GFL-VSC to reach the SEP is still influenced by its transient dynamics, which will be discussed in detail in this section [J1], [C1].

2.4.1. LARGE-SIGNAL MODELING

The objective of this subsection is to establish a comprehensive large-signal model of the GFL-VSC that considers the impact of both the PLL and VDCI during transient dynamics [J1], [C1]. Unlike the steady-state model described in Section 2.3, where θ_{FRT}, ω_{PLL}, δ and V_{cm} are assumed to have constant values, these variables exhibit time-varying behavior during transient dynamics.

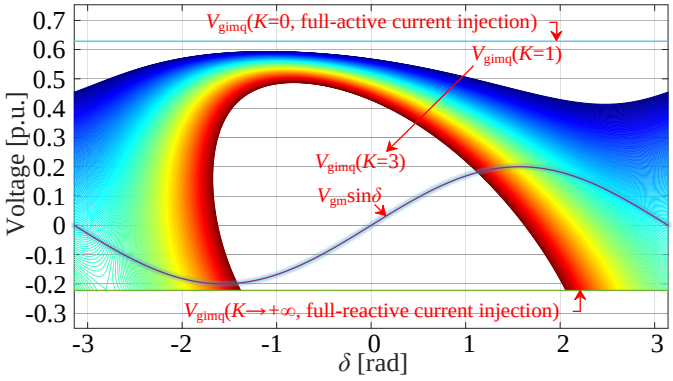

Figure 2.6. Relationship between V_{gimq} and $V_{gm}\sin\delta$ curve. Source:[J1].

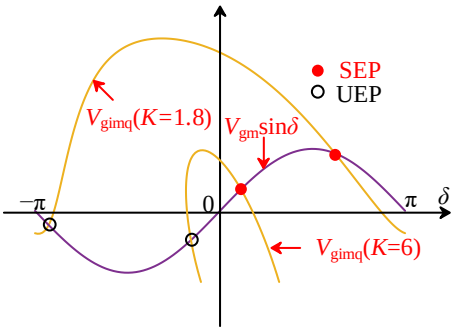

Figure 2.7. SEP and UEP. Source:[J1].

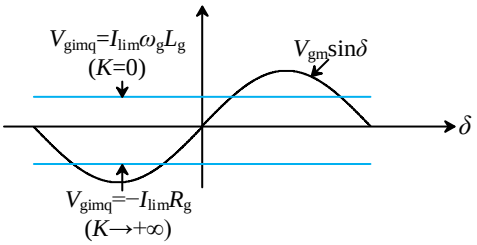

(a)

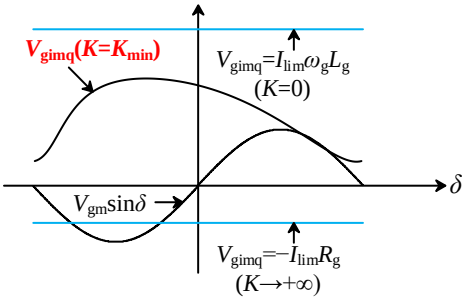

(b)

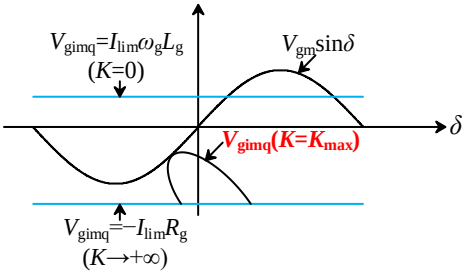

(c)

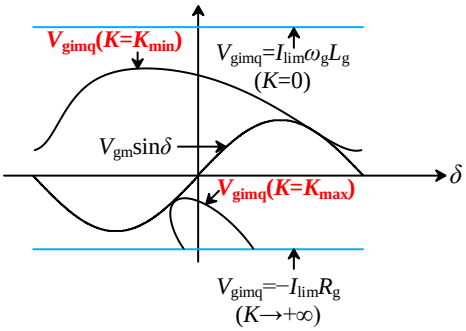

(d)

Figure 2.8. Conditions of existence of EPs by comparing V_{gimq} and $V_{gm}\sin\delta$ curve. (a) $-V_{gm}<-I_{lim}R_g<I_{lim}\omega_g L_g<V_{gm}$, the system always has EPs. (b) $-V_{gm}<-I_{lim}R_g<V_{gm}<I_{lim}\omega_g L_g$, $K_{min}<K<+\infty$ for the existence of EPs. (c) $-I_{lim}R_g<-V_{gm}<I_{lim}\omega_g L_g<V_{gm}$, $0<K<K_{max}$ for the existence of EPs. (d) $-I_{lim}R_g<-V_{gm}<V_{gm}<I_{lim}\omega_g L_g$, $K_{min}<K<K_{max}$ for the existence of EPs. Source:[J1].

The dynamic equation of the PLL, as depicted in Figure 2.2, can be expressed as shown in (2.13) [J1], [C1].

$$\theta_{PLL}=\int\omega_{PLL}\mathrm{d}t=\int\left(\omega_g+\Delta\omega\right)\mathrm{d}t=\int\left[\omega_g+\left(K_pV_{cq}+K_i\int V_{cq}\mathrm{d}t\right)\right]\mathrm{d}t \tag{2.13}$$

where V_{cq} can be further expanded in (2.14) [J1], [C1].

$$\begin{aligned}V_{cq}&=V_{gimq}+V_{gq}=I_{gd}\omega_{PLL}L_g+I_{gq}R_g-V_{gm}\sin\delta\\&=I_{gd}\left(\omega_g+\Delta\omega\right)L_g+I_{gq}R_g-V_{gm}\sin\delta\\&=I_{lim}\cos\theta_{FRT}\left(\omega_g+\Delta\omega\right)L_g-I_{lim}\sin\theta_{FRT}R_g-V_{gm}\sin\delta\end{aligned} \tag{2.14}$$

By considering the phase angle of the grid voltage, denoted as $\theta_g=\int\omega_g\mathrm{d}t$, it is straightforward to derive (2.15) [J1], [C1].

$$\theta_{PLL}=\theta_g+\int\Delta\omega\mathrm{d}t\Rightarrow\dot{\delta}=\Delta\omega \tag{2.15}$$

The dynamic equation of the PLL can be reconstructed by substituting (2.14) and (2.15) into (2.13), resulting in (2.16) [J1], [C1].

$$\begin{aligned}\dot{\delta}&=K_p\left[I_{lim}\cos\theta_{FRT}\left(\omega_g+\dot{\delta}\right)L_g-I_{lim}\sin\theta_{FRT}R_g-V_{gm}\sin\delta\right]\\&+K_i\int\left[I_{lim}\cos\theta_{FRT}\left(\omega_g+\dot{\delta}\right)L_g-I_{lim}\sin\theta_{FRT}R_g-V_{gm}\sin\delta\right]\mathrm{d}t\end{aligned} \tag{2.16}$$

By substituting ω_g with $\omega_{PLL}=\omega_g+\Delta\omega$, the expression for the PoC voltage during the transient dynamics can be derived as presented in equation (2.17) [J1], [C1].

$$\begin{pmatrix} V_{cd} \\ V_{cq} \end{pmatrix} = I_{lim}\omega_{PLL}L_g \begin{pmatrix} \sin\theta_{FRT} \\ \cos\theta_{FRT} \end{pmatrix} + I_{lim}R_g \begin{pmatrix} \cos\theta_{FRT} \\ -\sin\theta_{FRT} \end{pmatrix} + V_{gm} \begin{pmatrix} \cos\delta \\ -\sin\delta \end{pmatrix} \tag{2.17}$$

Substituting (2.10) and (2.17) into (2.11), the relationship between θ_{FRT} and δ can be determined, which is expressed in (2.18) [J1].

$$\theta_{FRT} = \begin{cases} -\arctan\left(\dfrac{K\left(\dfrac{\sqrt{\left(I_{lim}\left(\omega_g+\dot{\delta}\right)L_g\sin\theta_{FRT}+I_{lim}R_g\cos\theta_{FRT}+V_{gm}\cos\delta\right)^2+\left(I_{lim}\left(\omega_g+\dot{\delta}\right)L_g\cos\theta_{FRT}-I_{lim}R_g\sin\theta_{FRT}-V_{gm}\sin\delta\right)^2}}{V_{cm0}}-1\right)}{\sqrt{1-\left[K\left(\dfrac{\sqrt{\left(I_{lim}\left(\omega_g+\dot{\delta}\right)L_g\sin\theta_{FRT}+I_{lim}R_g\cos\theta_{FRT}+V_{gm}\cos\delta\right)^2+\left(I_{lim}\left(\omega_g+\dot{\delta}\right)L_g\cos\theta_{FRT}-I_{lim}R_g\sin\theta_{FRT}-V_{gm}\sin\delta\right)^2}}{V_{cm0}}-1\right)\right]^2}} \right) \\ \text{when } -\dfrac{1}{K}V_{cm0} < \left(V_{cm}-V_{cm0}\right) < \dfrac{1}{K}V_{cm0} \\ -\dfrac{\pi}{2} \\ \text{when } \left(V_{cm}-V_{cm0}\right) \geq \dfrac{1}{K}V_{cm0} \\ \dfrac{\pi}{2} \\ \text{when } \left(V_{cm}-V_{cm0}\right) \leq -\dfrac{1}{K}V_{cm0} \end{cases} \tag{2.18}$$

The transient dynamics of the GFL-VSC, considering the influence of both the PLL and VDCI, are captured by the equations (2.16) and (2.18), which describe the system's large-signal behavior [J1], [C1]. Previous works have only considered fixed values of θ_{FRT}, such as $\pi/2$, indicating full reactive current injection. However, in this study, the time-varying nature of θ_{FRT} is considered, as it is coupled with δ

through the dynamics of VDCI, as illustrated in equation (2.18). Furthermore, (2.18) shows that *K*-factor also affects the dynamics of θ_{FRT}. Hence, the value of the *K*-factor plays a crucial role in determining the GFL-VSC's ability to converge to the SEP, which will be comprehensively discussed in the subsequent analysis [J1], [C1].

2.4.2. IMPACT OF *K*-FACTOR ON SYSTEM TRANSIENT DYNAMICS

To gain a deeper understanding of the dynamic effects of *K*-factors, (2.16) is transformed into a standard form resembling the swing equation of SGs by taking derivatives of both sides [70], as presented in (2.19) [J1].

$$V_{\mathrm{gimq}} - V_{\mathrm{gq}} - D_{\mathrm{eq}}\left(\delta, \theta_{\mathrm{FRT}}\right)\dot{\delta} = \frac{1}{K_{\mathrm{i}}}\ddot{\delta} \tag{2.19}$$

The dynamic damping coefficient, denoted as D_{eq} in (2.19), is affected by various factors including the parameters of the PLL, the impedance of the grid, the residual grid voltage, and the *K*-factor [J1]. The detailed expression for D_{eq} is provided in (2.20) [J1]. Previous studies have typically neglected the dynamic influence of the VDCI by assuming a constant value for θ_{FRT} during grid faults, which implies that the rate of change of θ_{FRT} with respect to time, $\mathrm{d}\theta_{\mathrm{FRT}}/\mathrm{dt}$, is equal to zero [J1]. Hence, the dynamic damping coefficient can be simplified to $D_{\mathrm{eq}}=(K_{\mathrm{p}}/K_{\mathrm{i}})V_{\mathrm{gm}}\cos\delta$ [57], which can be viewed as a specific instance within the context of the current study [J1].

Based on (2.20), D_{eq}-δ curves can be plotted for different *K*-factors, as demonstrated in Figure 2.9. It is a well-established fact that larger values of D_{eq} are beneficial for the system's transient stability when EPs exist. However, as depicted in Figure 2.9, the dynamic damping coefficient, D_{eq}, is not a constant value but rather exhibits variation with respect to δ [J1]. It is worth noting that, according to (2.20), D_{eq} is a periodic function with a fundamental period of 2π [J1]. Consequently, to capture the overall damping effect of the system, the average value of D_{eq} within the interval

$$D_{\mathrm{eq}}\left(\delta, \theta_{\mathrm{FRT}}\right)\dot{\delta} = \begin{cases} \dfrac{K_{\mathrm{p}}}{K_{\mathrm{i}}} V_{\mathrm{gm}} \cos\delta\,\dot{\delta} + \dfrac{K_{\mathrm{p}}}{K_{\mathrm{i}}} I_{\mathrm{lim}}\left(\omega_{\mathrm{g}} L_{\mathrm{g}} \sin\theta_{\mathrm{FRT}} + R_{\mathrm{g}} \cos\theta_{\mathrm{FRT}}\right)\dot{\theta}_{\mathrm{FRT}} \\ \text{when}\left(|V_{\mathrm{cm}} - V_{\mathrm{cm0}}|\right) < \dfrac{1}{K} V_{\mathrm{cm0}} \\ \dfrac{K_{\mathrm{p}}}{K_{\mathrm{i}}} V_{\mathrm{gm}} \cos\delta\,\dot{\delta} \\ \text{when}\left(|V_{\mathrm{cm}} - V_{\mathrm{cm0}}|\right) \geq \dfrac{1}{K} V_{\mathrm{cm0}} \end{cases}$$

(2.20.1)

$$\dot{\theta}_{\mathrm{FRT}}=\frac{\dfrac{K}{V_{\mathrm{cm}}V_{\mathrm{cm0}}\sqrt{1-K^{2}\left(1-\dfrac{V_{\mathrm{cm}}}{V_{\mathrm{cm0}}}\right)^{2}}}\begin{bmatrix}I_{\mathrm{lim}}\omega_{\mathrm{g}}L_{\mathrm{g}}V_{\mathrm{gm}}\cos\left(\delta-\theta_{\mathrm{FRT}}\right)\\+I_{\mathrm{lim}}R_{\mathrm{g}}V_{\mathrm{gm}}\sin\left(\delta-\theta_{\mathrm{FRT}}\right)\end{bmatrix}}{1+\dfrac{K}{V_{\mathrm{cm}}V_{\mathrm{cm0}}\sqrt{1-K^{2}\left(1-\dfrac{V_{\mathrm{cm}}}{V_{\mathrm{cm0}}}\right)^{2}}}\begin{bmatrix}I_{\mathrm{lim}}\omega_{\mathrm{g}}L_{\mathrm{g}}V_{\mathrm{gm}}\cos\left(\delta-\theta_{\mathrm{FRT}}\right)\\+I_{\mathrm{lim}}R_{\mathrm{g}}V_{\mathrm{gm}}\sin\left(\delta-\theta_{\mathrm{FRT}}\right)\end{bmatrix}}\dot{\delta} \tag{2.20.2}$$

$[-\pi, \pi]$ is employed, denoted as $D_{\text{eq-ave}}$, and it is presented in (2.21) [J1].

$$D_{\text{eq-ave}}=\frac{1}{2\pi}\int D_{\text{eq}}\left(\delta\right)\mathrm{d}\delta \tag{2.21}$$

The $D_{\text{eq-ave}}$ values with various K-factors are shown in Figure 2.10. It is evident that $D_{\text{eq-ave}}$ initially increases and then decreases with an increase in K-factor. Hence, choosing an excessively small or large K-factor can lead to insufficient damping, thereby resulting in a loss of synchronization (LOS) during grid faults, despite the existence of EPs [J1]. Nevertheless, it is important to acknowledge that $D_{\text{eq-ave}}$ serves as a qualitative indicator employed to assess the transient dynamic performance for the purpose of providing intuitive understanding [J1]. To obtain a more accurate assessment of transient dynamics, the developed analytical model must be checked, which considers both PLL and VDCI dynamics, as given in (2.16) and (2.18) [J1].

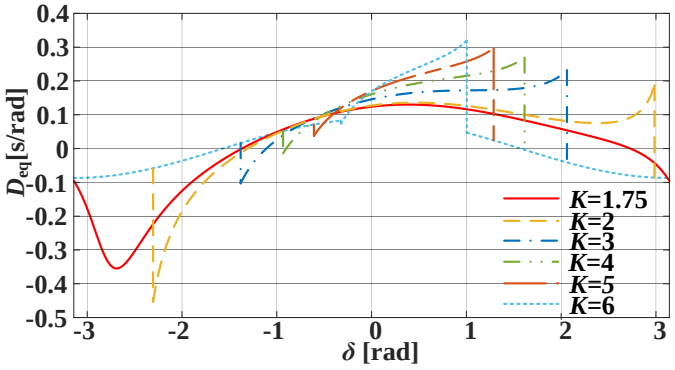

Figure 2.9. Dynamic damping curves. Source:[J1].

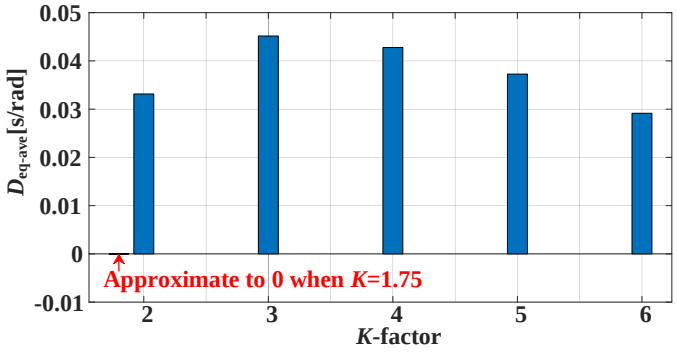

Figure 2.10. Average value of dynamic damping curves. Source:[J1].

2.4.3. IMPACT OF PLL ON THE SELECTION OF *K*-FACTOR

Considering the influence of both PLL parameters and the *K*-factor on the transient dynamic performance of the system, it becomes crucial to establish a formulation that accounts for the impact of PLL parameters in the selection of the *K*-factor [J1]. To ensure clarity, the available ranges of the *K*-factor that guarantee the existence of EPs and the capability to converge to EPs can be denoted as (K_{min0}, K_{max0}) and (K_{min1}, K_{max1}) respectively [J1]. It can be concluded that $K_{min0} \leq K_{min1} < K_{max1} \leq K_{max0}$, as the existence of EPs is a prerequisite for the convergence of the system's transient dynamics [J1]. The impact of PLL parameters on these ranges is discussed below.

- The determination of the system's EPs is based on (2.6) and (2.12), which reveals that the existence of EPs relies solely on the steady-state operation of the system and remains unaffected by the PLL parameters [J1]. Therefore, the range of *K*-factor (K_{min0}, K_{max0}) remains unaffected by the PLL parameters.
- As discussed in sections 2.4.1 and 2.4.2, the system's ability to converge to EPs, despite their existence, is determined by the transient dynamics, which is influenced by both the *K*-factor and the PLL parameters [J1]. Enhancing the transient dynamics performance of the system can be achieved by increasing the settling time and damping ratio of the PLL, as suggested in prior research [57].

In conclusion, the optimization of PLL parameters has the potential to broaden the ranges of *K*-factors, denoted as (K_{min1}, K_{max1}), which guarantee transient stability of the system [J1]. However, the extension of this range is limited by the existence of EPs, which restricts the available range of *K*-factors to (K_{min0}, K_{max0}) [J1].

Theoretical calculations are conducted to analyze the transient dynamics of the GFL-VSC during grid faults, specifically when V_{gm} decreases to 0.2 p.u., considering

various *K*-factor scenarios [system parameters are listed in Table 2.1] [J1]. The corresponding results are illustrated in Figure 2.11. It is important to highlight that all the considered *K*-factor values at here can ensure the existence of EPs of the GFL-VSC [J1]. However, selecting *K*=1.75 leads to LOS of the GFL-VSC due to the nearly zero $D_{\text{eq-ave}}$ [refer to Figure 2.10]. On the contrary, the transient stability of the GFL-VSC is preserved within the range of *K*-factors from 2 to 6 [J1]. It is observed that the overshoot in the dynamic response exhibits a non-monotonic property as the *K*-factor increases [J1]. Initially, the overshoot decreases, followed by an increase, which can be roughly attributed to the changing trend of $D_{\text{eq-ave}}$ shown in Figure 2.10 [J1].

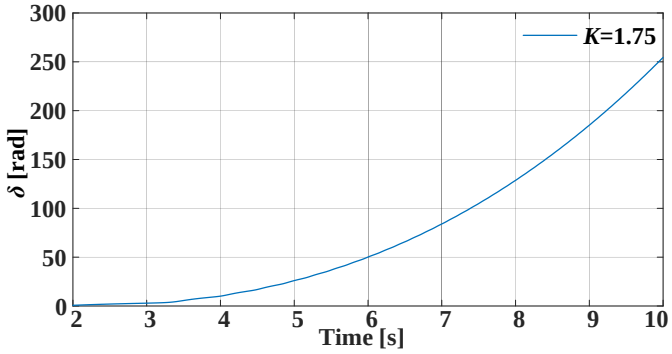

(a)

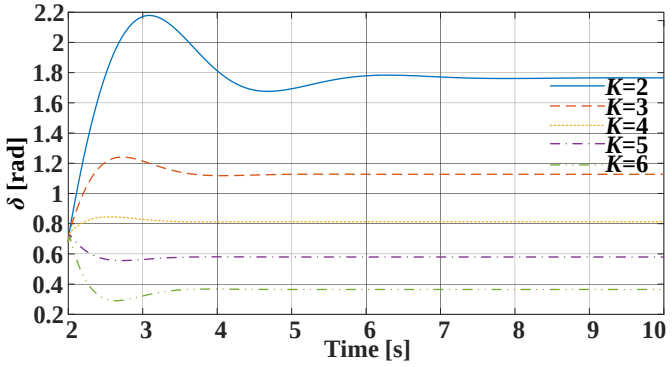

(b)

Figure 2.11. Theoretically calculated dynamics of GFL-VSC under grid faults with different *K*-factors [same PLL parameters are adopted for all the cases, i.e., t_s=1, ξ=1], where V_{gm} drops to 0.2 p.u. (a) Diverged response. (b) Converged response. Source: [J1].

2.5. CASE STUDIES AND DISCUSSION

To validate the theoretical analysis, a PSCAD/EMTDC simulation model was developed to emulate the behavior of a two-level GFL-VSC [J1]. The simulation was conducted on a personal computer with the following configuration: Intel(R) Core (TM) i5-8250U CPU @ 1.60GHz 1.80 GHz and 8 GB RAM [J1]. The simulation step was set to 1 μs, and the software version used was 4.6.3 (64-bit) [J1]. Table 2.1 provides the relevant parameters for the case studies in the EMT simulation [J1]. To simulate a grid fault scenario, the magnitude of the grid voltage was reduced to 0.2 p.u. [J1]. For each case study, the existence of EPs and the response of the transient dynamics were examined [J1].

Table 2.1 Parameters in case studies. Source:[J1].

Symbol	Description	Value (p.u.)
I_{lim}	Current rating value of the VSC	15.72 A (1.00 p.u.)
L_{g}	Grid inductance	9.00 mH (0.63 p.u.)
L_{f}	Filter inductance	3.00 mH (0.21 p.u.)
R_{g}	Grid resistance	1.00 Ω (0.22 p.u.)
V_{gms}	Grid voltage magnitude during steady state	70.71 V (1.00 p.u.)
V_{gm}	Residual grid voltage magnitude	14.14 V (0.20 p.u.)
t_{s}	Settling time of PLL	1s
ξ	Damping ratio of PLL	1 and 10
K_{p}	Proportional gain of PLL	0.13
K_{i}	Integral gain of PLL	0.30 for ξ=1 / 0.0030 for ξ=10
$f_{\text{B\_PLL}}$	Bandwidth of PLL	1.51 Hz for ξ=1 / 1.46 Hz for ξ=10

Table 2.1 Parameters in case studies, continued. Source:[J1].

Symbol	Description	Value (p.u.)
K_{pi}	Proportional gain of current loop controller	18.85
K_{ii}	Integral gain of current loop controller	0.38
f_{B_cc}	Bandwidth of current control loop	1000 Hz
V_{cm0}	Nominal magnitude of PoC voltage	70.71 V (1.00 p.u.)
V_{dc}	DC-side voltage	600V
ω_g	Nominal grid frequency	100π rad/s
SCR	Short circuit ratio during steady state	1.50
K	*K*-factor	from 1 to 6
f_s	Switching frequency of the VSC	10 kHz

It is worth mentioning that the selection of PLL parameters (K_p and K_i) in this study follows the established guidelines outlined in [77], which considers settling time (t_s) and damping ratio (ξ) [$t_s=9.2V_{cm0}/K_p$, $\xi = 0.5K_p\sqrt{V_{cm0}/K_i}$] [J1].

Experimental investigations were carried out using the DS1007 dSPACE system, employing the parameters specified in Table 2.1 [J1].

2.5.1. RANGES OF *K*-FACTORS THAT GUARANTEES SYSTEM TRANSIENT STABILITY

2.5.1.1 Existence of EPs

The calculation of EPs for the VSC-grid system under various *K*-factors during grid faults was performed using equations (2.6) and (2.12), and the corresponding results are tabulated in Table 2.2. The analysis reveals that the system exhibits EPs when the *K*-factor exceeds 1.7, and the specific locations of these EPs are dependent on *K*-factor. This observation is further illustrated in Figure 2.12, where the V_{gimq}-δ curves and $V_{gm}\sin\delta$ curve intersect for *K*-factors greater than 1.7, thereby signifying the existence of EPs [J1].

2.5.1.2 Convergence to EPs

Based on the calculations derived from equations (2.16) and (2.18), it is determined that the convergence to SEPs in the GFL-VSC system is only possible when $K \geq 2$, as illustrated in Figure 2.11. In the case where $1.7<K<2$, the system lacks damping and thus LOS is still unavoidable, despite the existence of SEPs. These theoretical predictions will be validated in section 2.5.2 through simulation and experimental results [J1].

2.5.2. SIMULATION AND EXPERIMENTAL RESULTS

The theoretical analysis was verified through EMT simulations, and the corresponding results are illustrated in Figure 2.13. During the grid fault, the system exhibits instability when $K=1.7$ due to the lack of EPs, as evidenced by the diverging values of δ, $\Delta\omega$ and θ_{FRT}, as depicted in Figure 2.13 (a) [J1]. While increasing *K* to1.75 restores the existence of EPs, the insufficient dynamic damping persists, leading to LOS as illustrated in Figure 2.13 (b) [J1]. The system finally achieves stability by further increasing *K* to 2, as illustrated in Figure 2.13 (c) [J1].

Table 2.2. Results of EPs calculation. Source:[J1].

***K*-factor**	**δ(rad)**	**θ_{FRT}(rad)**	***K*-factor**	**δ(rad)**	**θ_{FRT}(rad)**
1	None	None	3	1.13	0.96
1.7	None	None	4	0.81	1.01
1.75	2.28	1.00	5	0.58	1.07
2	1.76	0.93	6	0.36	1.12

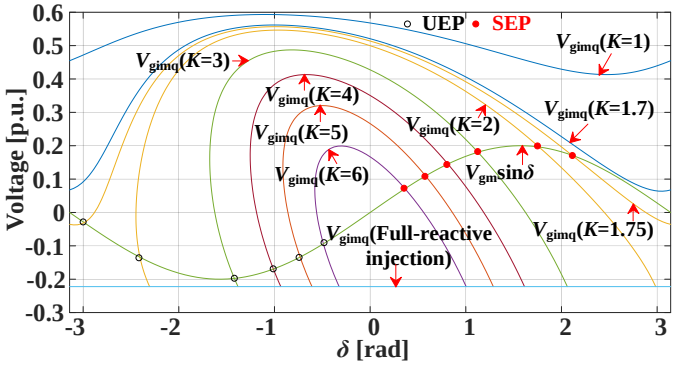

Figure 2.12. Graph-based EPs analysis. Source: [J1].

Furthermore, enhancing the damping ratio of the PLL to 10 achieves stability in the system, even when K=1.75, as depicted in Figure 2.13 (d) [J1]. This validates that by optimizing the PLL parameters, the minimum K-factor ensures transient stability of the system can be extended from 2 to 1.75, as discussed in subsection 2.4.3 [J1].

The stability predictions made based on the theoretical model are verified with acceptable accuracy through cross-validation, as depicted in Figure 2.14. The figure presents the simulated and theoretically calculated results of the GFL-VSC during grid faults for four different cases [J1].

The slight mismatch between calculated and simulated results in Figure 2.14 can be attributed to the omission of current control loop in the theoretical model [J1]. Nevertheless, the mismatch is negligible given that the bandwidth of the current control loop (1000Hz) and PLL (approximately 1.5Hz) indicates their decoupled nature [J1]. The theoretical analysis presented in Figure 2.14 demonstrates that the disregarded current control loop has little impact on the results [J1].

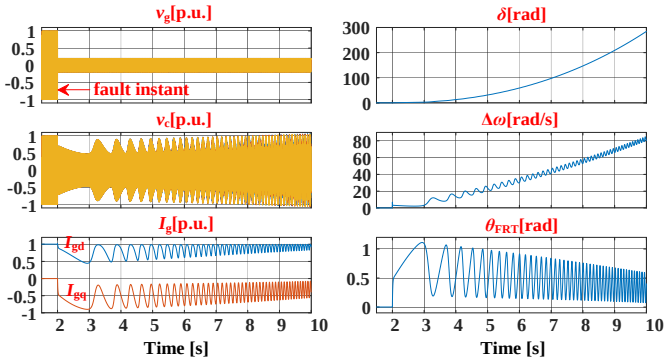

(a)

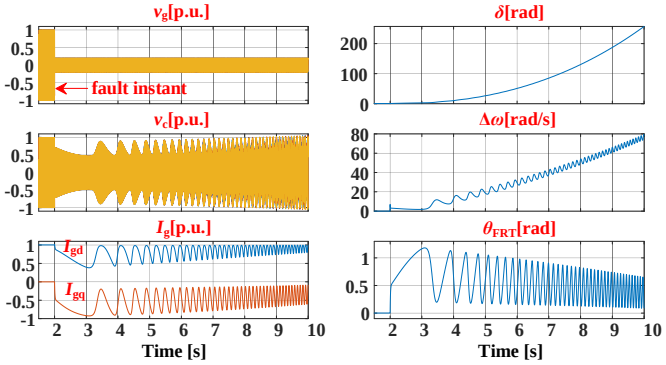

(b)

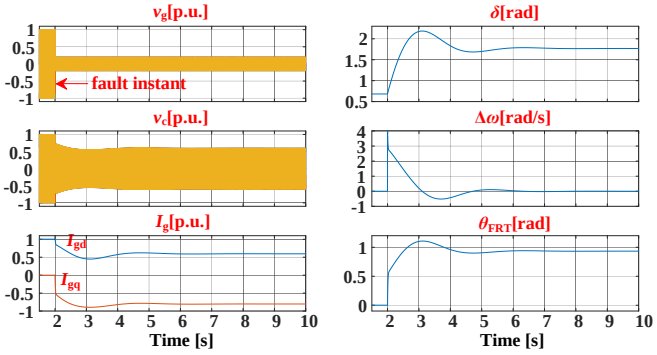

(c)

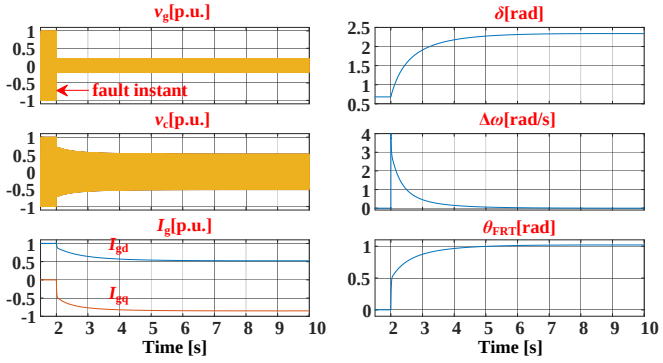

(d)

Figure 2.13. Simulation results of transient dynamics, where V_{gm} drops to 0.2 p.u. (a) K=1.7, t_s=1, ξ=1, unstable. (b) K=1.75, t_s=1, ξ=1, unstable. (c) K=2, t_s=1, ξ=1, stable. (d) K=1.75, t_s=1, ξ=10, stable. Source: [J1].

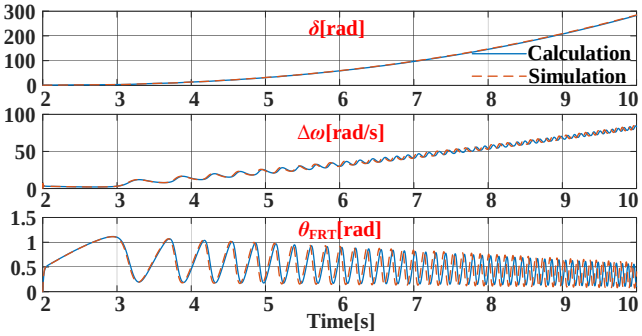
δ[rad]
Calculation
Simulation
Δω[rad/s]
θFRT[rad]
Time[s]

(a)

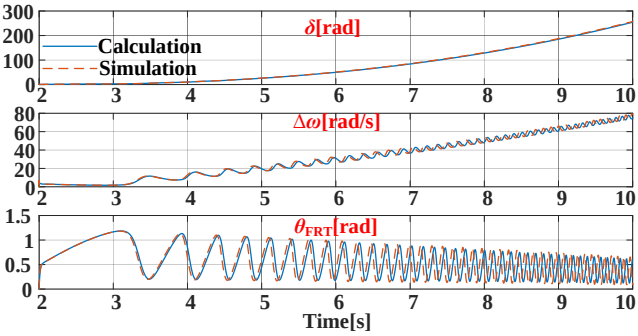
δ[rad]
Calculation
Simulation
Δω[rad/s]
θFRT[rad]
Time[s]

(b)

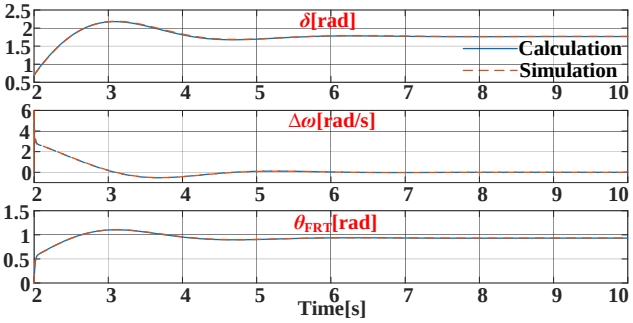
δ[rad]
Calculation
Simulation
Δω[rad/s]
θFRT[rad]
Time[s]

(c)

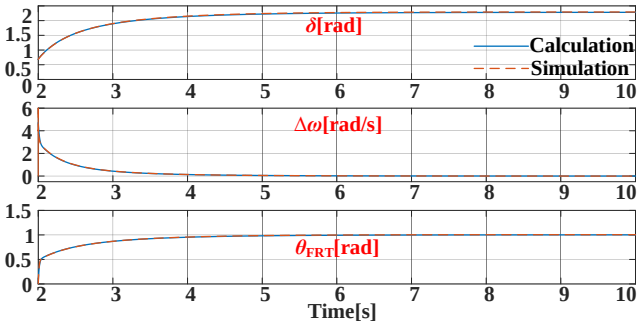

(d)

Figure 2.14. Theoretically calculated and simulated transient dynamics of GFL-VSC during grid faults, where V_{gm} drops to 0.2 p.u. (a) K=1.7, t_s=1, ξ=1, unstable. (b) K=1.75, t_s=1, ξ=1, unstable. (c) K=2, t_s=1, ξ=1, stable. (d) K=1.75, t_s=1, ξ=10, stable. Source: [J1].

Therefore, the developed theoretical model, exhibiting a computational speed approximately ten times faster than EMT simulations (as indicated in Table 2.3), is suitable for conducting transient stability evaluations of the system [J1].

Table 2.3. Comparison of time consumption for one case study. Source:[J1].

	EMT simulation	**Theoretical calculation**
Duration	around 100s	around 10s

To further corroborate the proposed theoretical analysis, experimental investigations are performed utilizing the setup depicted in Figure 2.15. The control scheme is implemented on the DS1007 dSPACE system, with voltage and current measurements conducted using the DS2004 A/D board [J1]. The waveforms are generated by the DS2102 D/A board and visualized on the oscilloscope for analysis [J1]. A constant DC voltage supply is applied to the DC-side, while the grid voltage is emulated using a Chroma 61850 grid simulator [J1].

Figure 2.16. presents the experimental results that correspond to the four simulation cases shown in Figure 2.13. In the experiments, symmetrical grid faults were emulated by changing the voltage magnitude in the grid simulator to from 1 p.u. to 0.2 p.u. at the instant of the fault [J1].

By comparing Figure 2.13 and Figure 2.16, it can be observed that the experimental results match well with the simulation results obtained under different K-factors and

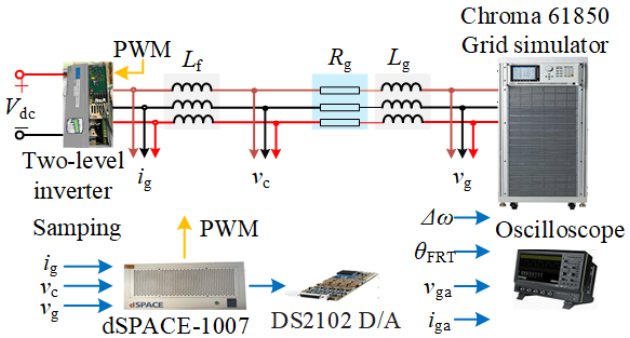

Figure 2.15. Experimental setup. Source: [J1].

PLL parameters, thereby providing further validation for the correctness of the proposed theoretical analysis [J1]. The comparison between Figure 2.13 and Figure 2.16 reveals a match between the experimental and simulation results across various *K*-factors and PLL parameters, which further supports the effectiveness of the proposed theoretical analysis [J1].

2.5.3. SENSITIVITY ANALYSIS

The transient stability of the VSC-grid system is influenced by the characteristics of the grid impedance, as demonstrated in (2.16) and (2.18) [J1]. Nevertheless, due to the uncertain and time-variant nature of grid impedance in practical power systems, it is necessary to conduct a sensitivity analysis to establish the relationship between the acceptable ranges of the *K*-factor to ensure transient stability and the varying grid impedance [J1]. Figure 2.17 visualizes this relationship, indicating that a smaller SCR, which implies a larger grid impedance, imposes more constraints on the acceptable *K*-factor ranges [J1]. This conclusion is intuitive when examining Figure 2.5, where an increased grid impedance results in greater fluctuations in the PoC voltage due to the injected current [J1]. This stronger interaction with the dynamics of the PLL and VDCI further leads to a higher risk of transient instability [J1].

2.6. SUMMARY

This chapter provides a comprehensive analysis of the transient stability of the GFL-VSC under FRT condition, taking into account the influence of VDCI. The investigation reveals the impact of the *K*-factors employed in the VDCI algorithm on the existence of EPs and the transient dynamics of the GFL-VSC [J1]. To gain a deeper understanding and offer guidance in selecting suitable *K*-factors that guarantee the transient stability of the GFL-VSC, an analytical model is developed, considering both PLL and VDCI dynamics [J1]. The effectiveness of the proposed analytical model is validated through case studies conducted using both EMT

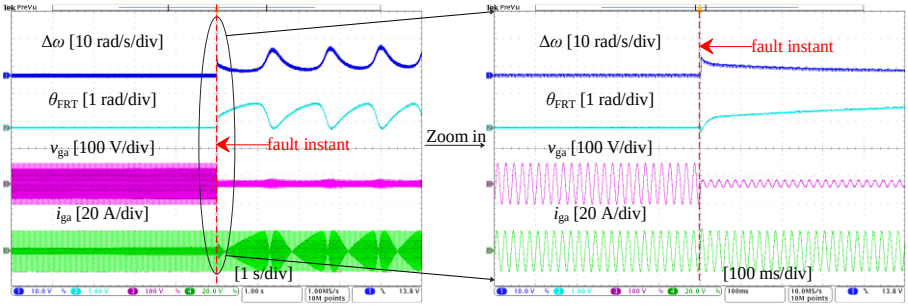
Δω [10 rad/s/div]
θFRT [1 rad/div]
vga [100 V/div]
iga [20 A/div]
fault instant
[1 s/div]
Zoom in
Δω [10 rad/s/div]
fault instant
θFRT [1 rad/div]
vga [100 V/div]
iga [20 A/div]
[100 ms/div]

(a)

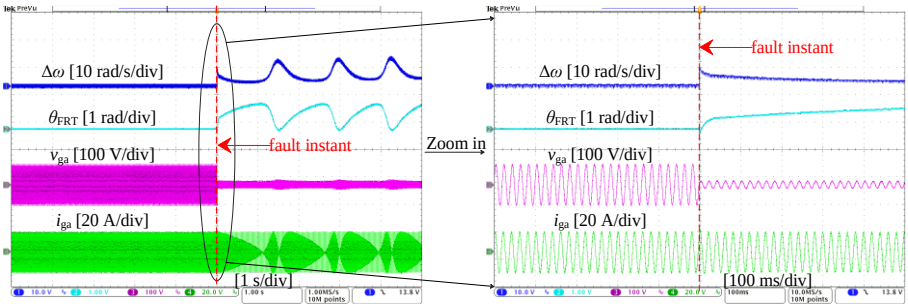
Δω [10 rad/s/div]
θFRT [1 rad/div]
vga [100 V/div]
iga [20 A/div]
fault instant
[1 s/div]
Zoom in
fault instant
Δω [10 rad/s/div]
θFRT [1 rad/div]
vga [100 V/div]
iga [20 A/div]
[100 ms/div]

(b)

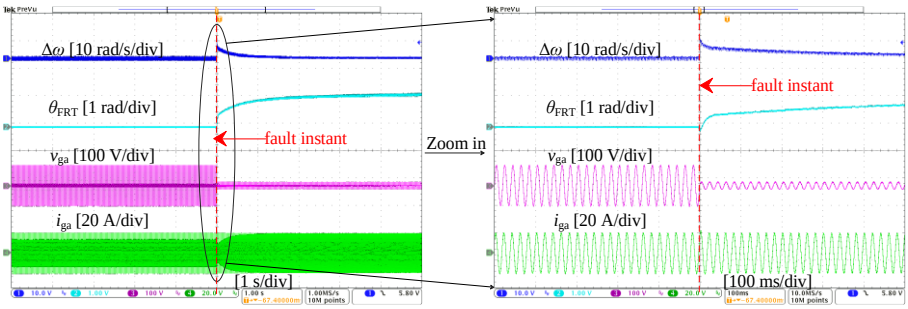
Δω [10 rad/s/div]
θFRT [1 rad/div]
vga [100 V/div]
iga [20 A/div]
fault instant
[1 s/div]
Zoom in
Δω [10 rad/s/div]
fault instant
θFRT [1 rad/div]
vga [100 V/div]
iga [20 A/div]
[100 ms/div]

(c)

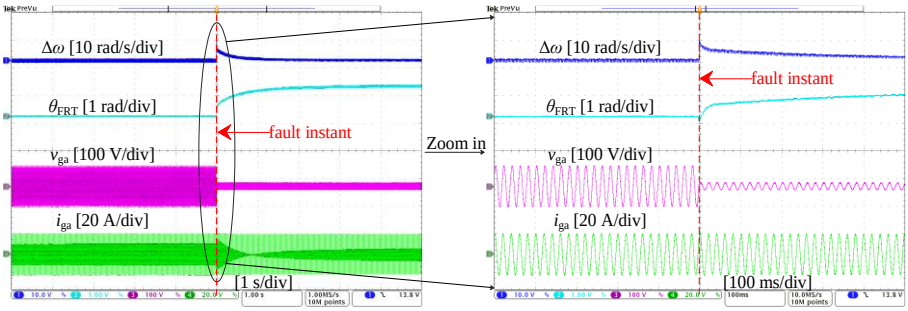

(d)

Figure 2.16. Experimental results of transient dynamics, where V_{gm} drops to 0.2 p.u. (a) K=1.7, t_s=1, ξ=1, unstable. (b) K=1.75, t_s=1, ξ=1, unstable. (c) K=2, t_s=1, ξ=1, stable. (d) K=1.75, t_s=1, ξ=10, stable. Source: [J1].

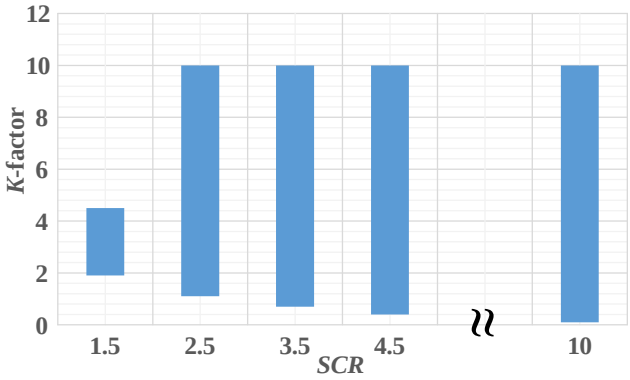

Figure 2.17. Relationship between acceptable ranges of K-factor that guarantee the system transient stability in respect to SCR. Source: [J1].

simulations and experimental tests [J1]. The validation demonstrates that the analytical model not only yields accurate outcomes for assessing transient stability but also exhibits computational efficiency [J1].

CHAPTER 3. IMPACT OF REACTIVE CURRENT INJECTION MODES ON TRANSIENT STABILITY OF GFL-VSCS

3.1. INTRODUCTION

In practical applications, VDCI is often classified into two distinct modes: A-RCI and R-RCI mode. These modes display variations in the reactive current bias along the FRT curve, as documented in [72], [76]. Despite the extensive research on transient stability analysis of GFL-VSCs, the investigation into how this bias influences the transient stability of such systems remains largely unexplored in the existing literature [C2]. This research gap emphasizes the need for a comprehensive examination of the effects of the reactive current bias on the dynamic behavior and stability performance of GFL-VSCs during FRT events [C2]. By addressing this knowledge gap, researchers can gain insights into the design and operation of VDCI strategies in grid-connected systems, ensuring the reliability of the GFL-VSC [C2].

To address this research gap, the study in [C2] conducts a comprehensive investigation of the transient stability of GFL-VSCs utilizing both A-RCI and R-RCI modes during FRT. The findings of this study are summarized in this chapter. The study indicates that the R-RCI mode is better suited for improving transient stability when the VSC operates with capacitive-reactive current injection during normal operation [C2]. On the other hand, the A-RCI mode is found to be more suitable in other scenarios [C2]. These results provide guidance for selecting the appropriate mode based on the operational characteristics of the VSC. Finally, the theoretical findings are validated by performing case studies.

3.2. SYSTEM DESCRIPTION

The schematic diagram (Figure 3.1) and synchronization unit (Figure 3.2) utilized in this study are identical to those presented in chapter 2. The GFL-VSC employs a single-loop current control scheme to ensure fast tracking of the output current during transient dynamics, as shown in Figure 3.1. Additionally, Figure 3.2 depicts the utilization of an SRF-PLL for synchronizing the GFL-VSC with the grid [C2]. To emulate fault operation, a magnitude sag in the grid voltage (V_g) is applied at the instant of the grid fault [C2]. As the variables in Figure 3.1 and Figure 3.2 correspond to those introduced in chapter 2, this chapter refrains from providing a detailed explanation of them.

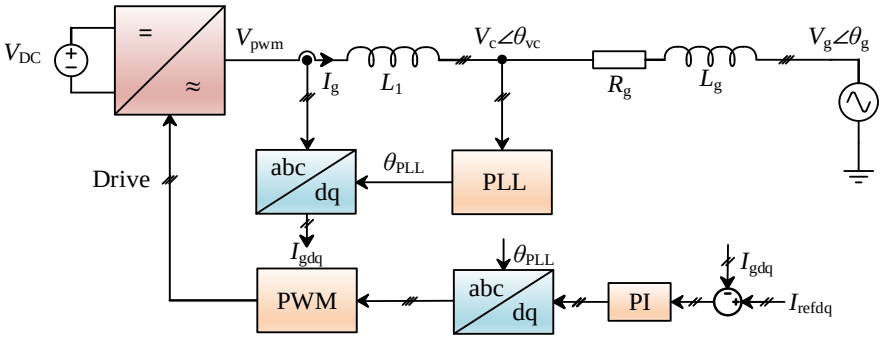

Figure 3.1. Control scheme of the GFL-VSC. Source: [C2].

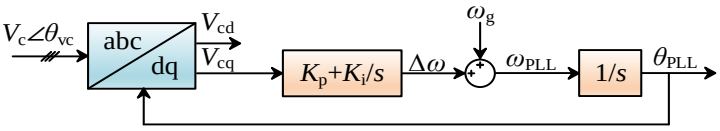

Figure 3.2. Synchronous reference frame PLL (SRF-PLL). Source: [C2].

In the event of grid faults, several existing grid codes require GFL-VSCs to implement VDCI for the provision of capacitive-reactive current during FRT conditions, as depicted in Figure 3.3 [73], [75], [76]. As a result, the current reference (I_{refdq}) during the FRT considering the effect of reactive current bias (I_{refqb}) and current limitation (I_{lim}) can be expressed as (3.1) [C2].

$$I_{refq}=\begin{cases}\min\left(\dfrac{KI_{lim}}{|V_{cn}|}\left(|V_c|-|V_{cn}|\right)+I_{refqb},\ I_{lim}\right)\\ \text{when}\left(|V_c|-|V_{cn}|\right)>0\\ \max\left(\dfrac{KI_{lim}}{|V_{cn}|}\left(|V_c|-|V_{cn}|\right)+I_{refqb},\ -I_{lim}\right)\\ \text{when}\left(|V_c|-|V_{cn}|\right)<0\end{cases} \tag{3.1.1}$$

$$I_{refd}=\sqrt{I_{lim}{}^2-I_{refq}{}^2} \tag{3.1.2}$$

where $|V_{cn}|$ and $|V_c|$ represents the nominal voltage magnitude at PoC and detected voltage magnitude at PoC respectively [C2]. The slope of FRT curves shown in Figure 3.3 in per unit system is normally called *K*-factor [73], [75], [76]. The *K*-factor, typically selected between 0 and 10 [72], [76], represents the responsiveness of the injected reactive current to the voltage drop at the PoC, where a higher *K*-

factor corresponds to a greater amount of reactive current injected by the GFL-VSC for a given magnitude of voltage drop [C2]. The determination of I_{refqb} varies depending on the reactive current injection mode: in the case of R-RCI, I_{refqb} corresponds to the reactive current injection level of the GFL-VSC during normal operation, while for A-RCI, I_{refqb} is set to zero [C2].

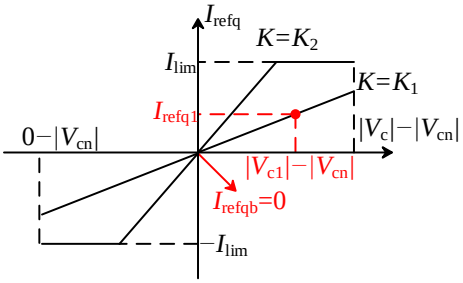

(a)

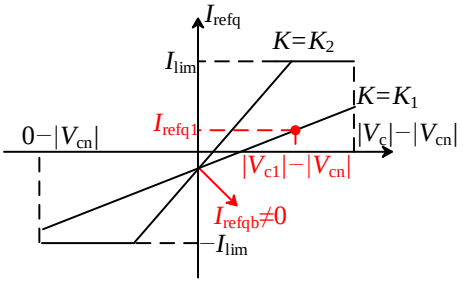

(b)

Figure 3.3. FRT curves. (a) A-RCI mode. (b) R-RCI mode. Source: [C2].

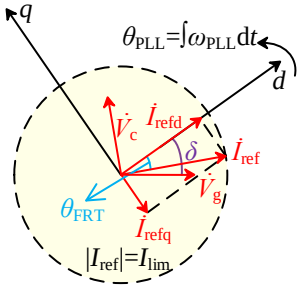

Figure 3.4. Vector diagram. Source: [C2].

Figure 3.4 depicts the vector diagram of the VSC-grid system during FRT, providing a visual representation of variables in the system [C2]. The power angle (δ) is defined as the angle between the *d*-axis and the grid voltage ($\delta=\theta_{PLL}-\theta_g$). The angle of current vector is expressed by θ_{FRT} in (3.2) [C2].

$$\theta_{FRT} = -\arctan\left(\frac{I_{refq}}{I_{refd}}\right) \tag{3.2}$$

Substituting (3.1) into (3.2) yields (3.3) [C2].

$$\theta_{FRT} = \begin{cases} -\arctan\left(\dfrac{KI_{lim}\left(\dfrac{|V_c|}{|V_{cn}|}-1\right)+I_{refqb}}{I_{lim}\sqrt{1-\left[K\left(\dfrac{|V_c|}{|V_{cn}|}-1\right)+\dfrac{I_{refqb}}{I_{lim}}\right]^2}}\right) \\ \text{when } \dfrac{1}{K}\left(-1-\dfrac{I_{refqb}}{I_{lim}}\right)|V_{cn}| < (|V_c|-|V_{cn}|) < \dfrac{1}{K}\left(1-\dfrac{I_{refqb}}{I_{lim}}\right)|V_{cn}| \\ -\dfrac{\pi}{2} \\ \text{when } (|V_c|-|V_{cn}|) \geq \dfrac{1}{K}\left(1-\dfrac{I_{refqb}}{I_{lim}}\right)|V_{cn}| \\ \dfrac{\pi}{2} \\ \text{when } (|V_c|-|V_{cn}|) \leq \dfrac{1}{K}\left(-1-\dfrac{I_{refqb}}{I_{lim}}\right)|V_{cn}| \end{cases} \tag{3.3}$$

The value of θ_{FRT}, as indicated by a positive value, signifies the injection of capacitive-reactive current by the GFL-VSC into the grid [C2]. It is evident from (3.3) that the value of θ_{FRT} is influenced by both the *K*-factor and the chosen mode of reactive current injection.

Under the assumption that the current control loop's bandwidth is considerably higher than that of the PLL, it can be inferred that the ideal tracking of current reference is attained, with $I_{gd}=I_{refd}$, $I_{gq}=I_{refq}$ [C2]. Considering this assumption, the equivalent circuit is shown in Figure 3.5.

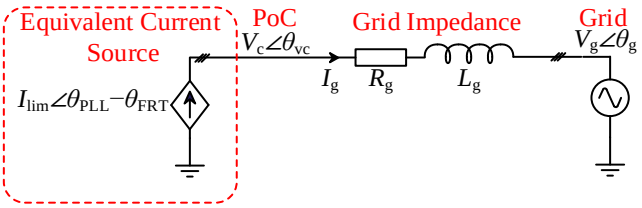

Figure 3.5. Equivalent VSC-grid system. Source: [C2].

3.3. ANALYSIS OF EPS

3.3.1. EPS CALCULATION

The procedure for calculating EPs is similar with chapter 2 but is repeated here for clarity of this chapter. To calculate the EPs, V_{cq}=0 can be represented as (3.4) [C2].

$$V_{cq} = V_{gimq} + V_{gq} = 0 \tag{3.4}$$

V_{gimq} and V_{gq} can be further expressed in (3.5) [C2].

$$V_{gimq} = I_{gd}\omega_g L_g + I_{gq}R_g = I_{lim}\cos\theta_{FRT}\omega_g L_g - I_{lim}\sin\theta_{FRT}R_g \tag{3.5.1}$$

$$V_{gq} = -V_g \sin\delta \tag{3.5.2}$$

Substituting (3.5) into (3.4), which yields (3.6) [C2].

$$\underbrace{I_{lim}\cos\theta_{FRT}\omega_g L_g - I_{lim}\sin\theta_{FRT}R_g}_{V_{gimq}} = \underbrace{V_g \sin\delta}_{-V_{gq}} \tag{3.6}$$

To solve (3.6), it is necessary to derive the relationship between δ and θ_{FRT} based on VDCI algorithm characterized by (3.1), which is elaborated below [C2].

$|V_c|$ can be calculated by using (3.7) [C2].

$$|V_c| = \sqrt{V_{cd}^{\ 2} + V_{cq}^{\ 2}} \tag{3.7}$$

where V_{cd} and V_{cq} represent the PoC voltages in the dq axis, respectively. These voltages can be further expressed by adding the grid voltage and the voltage across the grid impedance, as represented by (3.8) [C2].

$$\begin{pmatrix} V_{\mathrm{cd}} \\ V_{\mathrm{cq}} \end{pmatrix} = I_{\mathrm{lim}}\omega_{\mathrm{g}}L_{\mathrm{g}}\begin{pmatrix} \sin\theta_{\mathrm{FRT}} \\ \cos\theta_{\mathrm{FRT}} \end{pmatrix} + I_{\mathrm{lim}}R_{\mathrm{g}}\begin{pmatrix} \cos\theta_{\mathrm{FRT}} \\ -\sin\theta_{\mathrm{FRT}} \end{pmatrix} + V_{\mathrm{g}}\begin{pmatrix} \cos\delta \\ -\sin\delta \end{pmatrix} \tag{3.8}$$

The relationship between δ and θ_{FRT} can be derived in (3.9) through substituting (3.7) and (3.8) into (3.6) [C2]. The EPs are then solved by the algebraic equations composed of (3.6) and (3.9).

$$\theta_{\mathrm{FRT}} = \begin{cases} -\arctan\left(\dfrac{K\left(\dfrac{\sqrt{\left(I_{\mathrm{lim}}\omega_{\mathrm{g}}L_{\mathrm{g}}\sin\theta_{\mathrm{FRT}} + I_{\mathrm{lim}}R_{\mathrm{g}}\cos\theta_{\mathrm{FRT}} + V_{\mathrm{g}}\cos\delta\right)^2 + \left(I_{\mathrm{lim}}\omega_{\mathrm{g}}L_{\mathrm{g}}\cos\theta_{\mathrm{FRT}} - I_{\mathrm{lim}}R_{\mathrm{g}}\sin\theta_{\mathrm{FRT}} - V_{\mathrm{g}}\sin\delta\right)^2}}{|V_{\mathrm{cn}}|} - 1 \right) + \dfrac{I_{\mathrm{refqb}}}{I_{\mathrm{lim}}}}{\sqrt{1 - \left[K\left(\dfrac{\sqrt{\left(I_{\mathrm{lim}}\omega_{\mathrm{g}}L_{\mathrm{g}}\sin\theta_{\mathrm{FRT}} + I_{\mathrm{lim}}R_{\mathrm{g}}\cos\theta_{\mathrm{FRT}} + V_{\mathrm{g}}\cos\delta\right)^2 + \left(I_{\mathrm{lim}}\omega_{\mathrm{g}}L_{\mathrm{g}}\cos\theta_{\mathrm{FRT}} - I_{\mathrm{lim}}R_{\mathrm{g}}\sin\theta_{\mathrm{FRT}} - V_{\mathrm{g}}\sin\delta\right)^2}}{|V_{\mathrm{cn}}|} - 1 \right) + \dfrac{I_{\mathrm{refqb}}}{I_{\mathrm{lim}}} \right]^2}} \right) \\ \text{when } \dfrac{1}{K}\left(-1 - \dfrac{I_{\mathrm{refqb}}}{I_{\mathrm{lim}}}\right)|V_{\mathrm{cn}}| < \left(|V_{\mathrm{c}}| - |V_{\mathrm{cn}}|\right) < \dfrac{1}{K}\left(1 - \dfrac{I_{\mathrm{refqb}}}{I_{\mathrm{lim}}}\right)|V_{\mathrm{cn}}| \\ -\dfrac{\pi}{2} \\ \text{when } \left(|V_{\mathrm{c}}| - |V_{\mathrm{cn}}|\right) \geq \dfrac{1}{K}\left(1 - \dfrac{I_{\mathrm{refqb}}}{I_{\mathrm{lim}}}\right)|V_{\mathrm{cn}}| \\ \dfrac{\pi}{2} \\ \text{when } \left(|V_{\mathrm{c}}| - |V_{\mathrm{cn}}|\right) \leq \dfrac{1}{K}\left(-1 - \dfrac{I_{\mathrm{refqb}}}{I_{\mathrm{lim}}}\right)|V_{\mathrm{cn}}| \end{cases} \tag{3.9}$$

3.3.2. GRAPHICAL METHOD-BASED EPS ANALYSIS

Equations (3.6) and (3.9) reveal the dependence of the existence and position of EPs on both the *K*-factor and I_{refqb} [C2]. The influence of the *K*-factor has been previously discussed in chapter 2, while the impact of I_{refqb} is specifically analyzed in this chapter.

As discussed in subsection 3.3.1, EPs can be obtained as the solutions of the algebraic equation system given by (3.6) and (3.9). These solutions can be graphically obtained as the intersection points between the V_{gimq}-δ curve, which can be derived by replacing the θ_{FRT} in (3.5.1) with δ according to (3.9), and $V_{\mathrm{g}}\sin\delta$ curve.

Figure 3.6 presents the V_{gimq}-δ curves depicting various VSC operating modes during FRT. These modes include the R-RCI mode with capacitive (I_{refqb}<0) or inductive (I_{refqb}>0) reactive current injection prior to grid faults, along with the A-RCI (I_{refqb}=0) mode during FRT [C2]. A noticeable trend in the V_{gimq}-δ curves is the downward shift with a decrease in I_{refqb}. This behavior can be explained by the fact that smaller I_{refqb} leads to more negative I_{gq} under the same voltage magnitude sag at PoC, as expressed in (3.5.1). The more negative I_{gq} will further lower V_{gimq}-δ curves,

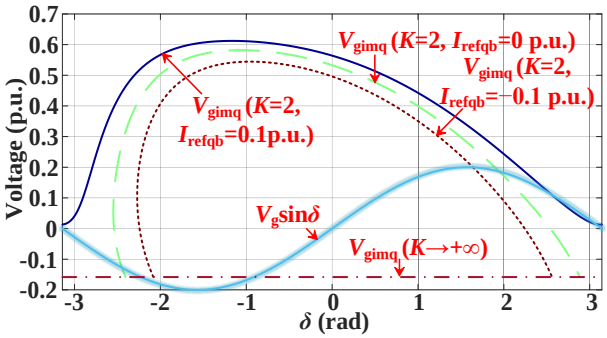

Figure 3.6. V_{gimq}-δ curve and $V_g \sin\delta$ curves. Source: [C2].

as presented in Figure 3.6. As the lower V_{gimq}-δ curve has a higher possibility of intersecting with the $V_g \sin\delta$ curve, the likelihood of the existence of EPs is also increased. Based on the findings, it is advisable to employ the R-RCI mode for GFL-VSCs that utilize capacitive-reactive current injection prior grid faults, while the A-RCI mode is more suitable for other scenarios [C2].

3.4. ANALYSIS OF TRANSIENT DYNAMICS

3.4.1. DYNAMIC MODEL DEVELOPMENT

This subsection introduces the large-signal model of GFL-VSC, which incorporates the dynamics of synchronization and the profile of current injection [C2]. During the transient dynamics, θ_{FRT}, ω_{PLL}, δ and $|V_c|$ become time-varying, which is different from static model presented in section 3.3 [C2].

The dynamic equation of the PLL is expressed in (3.10) [C2].

$$\theta_{PLL} = \int \omega_{PLL} \mathrm{d}t = \int \left(\omega_g + \Delta\omega\right)\mathrm{d}t = \int \left[\omega_g + \left(K_p V_{cq} + K_i \int V_{cq}\mathrm{d}t\right)\right]\mathrm{d}t \tag{3.10}$$

where V_{cq} can be expressed in (3.11) [C2].

$$\begin{aligned} V_{cq} &= V_{gimq} + V_{gq} \\ &= I_{gd}\omega_{PLL}L_g + I_{gq}R_g - V_g \sin\delta \\ &= I_{gd}\left(\omega_g + \dot{\delta}\right)L_g + I_{gq}R_g - V_g \sin\delta \\ &= I_{lim}\cos\theta_{FRT}\left(\omega_g + \dot{\delta}\right)L_g - I_{lim}\sin\theta_{FRT}R_g - V_g \sin\delta \end{aligned} \tag{3.11}$$

Considering the phase angle of grid voltage $\theta_g = \int \omega_g \mathrm{d}t$, the following expression can be derived [C2].

$$\theta_{\mathrm{PLL}} = \theta_{\mathrm{g}} + \int \Delta\omega \mathrm{d}t \Rightarrow \dot{\delta} = \Delta\omega \tag{3.12}$$

The PLL's dynamic equation can be reconstructed as (3.13) through substituting (3.11) and (3.12) into (3.10) [C2].

$$\begin{aligned} \dot{\delta} &= K_{\mathrm{p}}\left[I_{\mathrm{lim}} \cos\theta_{\mathrm{FRT}} \left(\omega_{\mathrm{g}} + \dot{\delta}\right) L_{\mathrm{g}} - I_{\mathrm{lim}} \sin\theta_{\mathrm{FRT}} R_{\mathrm{g}} - V_{\mathrm{g}} \sin\delta \right] \\ &+ K_{\mathrm{i}} \int \left[I_{\mathrm{lim}} \cos\theta_{\mathrm{FRT}} \left(\omega_{\mathrm{g}} + \dot{\delta}\right) L_{\mathrm{g}} - I_{\mathrm{lim}} \sin\theta_{\mathrm{FRT}} R_{\mathrm{g}} - V_{\mathrm{g}} \sin\delta \right] \mathrm{d}t \end{aligned} \tag{3.13}$$

The voltage at the PoC and its respective components in the *d* and *q* axis can be represented similarly to (3.7) and (3.8) by substituting ω_{g} with $\omega_{\mathrm{PLL}}=\omega_{\mathrm{g}}+\Delta\omega$. For the sake of simplicity, these equations will not be repeated here.

To mitigate the impact of magnitude detection noise, it is necessary to utilize a first-order low-pass filter (LPF) [C2].

$$|V_{\mathrm{c}}| = \frac{|\dot{V}_{\mathrm{cf}}|}{\omega_{\mathrm{p}}} + |V_{\mathrm{cf}}| \tag{3.14}$$

where the filtered magnitude of the PoC voltage, denoted as $|V_{\mathrm{cf}}|$, along with its first-order differential, $|\dot{V}_{\mathrm{cf}}|$, and the cut-off frequency of the first-order LPF, represented as ω_{p}, in (3.14) [C2]. Replacing $|V_{\mathrm{c}}|$ by $|V_{\mathrm{cf}}|$ in (3.3), the relationship between θ_{FRT} and $|V_{\mathrm{cf}}|$ can be expressed as (3.15) [C2].

$$\theta_{\mathrm{FRT}} = \begin{cases} -\arctan\left(\dfrac{KI_{\mathrm{lim}}\left(\dfrac{|V_{\mathrm{cf}}|}{|V_{\mathrm{cn}}|}-1\right)+I_{\mathrm{refqb}}}{I_{\mathrm{lim}}\sqrt{1-\left[K\left(\dfrac{|V_{\mathrm{cf}}|}{|V_{\mathrm{cn}}|}-1\right)+\dfrac{I_{\mathrm{refqb}}}{I_{\mathrm{lim}}}\right]^2}}\right) \\ \text{when } \dfrac{1}{K}\left(-1-\dfrac{I_{\mathrm{refqb}}}{I_{\mathrm{lim}}}\right)|V_{\mathrm{cn}}| < \left(|V_{\mathrm{cf}}|-|V_{\mathrm{cn}}|\right) < \dfrac{1}{K}\left(1-\dfrac{I_{\mathrm{refqb}}}{I_{\mathrm{lim}}}\right)|V_{\mathrm{cn}}| \\ -\dfrac{\pi}{2} \\ \text{when } \left(|V_{\mathrm{cf}}|-|V_{\mathrm{cn}}|\right) \geq \dfrac{1}{K}\left(1-\dfrac{I_{\mathrm{refqb}}}{I_{\mathrm{lim}}}\right)|V_{\mathrm{cn}}| \\ \dfrac{\pi}{2} \\ \text{when } \left(|V_{\mathrm{cf}}|-|V_{\mathrm{cn}}|\right) \leq \dfrac{1}{K}\left(-1-\dfrac{I_{\mathrm{refqb}}}{I_{\mathrm{lim}}}\right)|V_{\mathrm{cn}}| \end{cases} \tag{3.15}$$

Finally, the differential equation system, which includes equations (3.13), (3.14), and (3.15), can be used to solve the transient dynamics.

3.4.2. MODEL CROSS VALIDATION

To assess the efficacy of the proposed large-signal dynamic model, a cross-validation process is conducted, comparing the results obtained from EMT simulation and numerical calculations based on (3.13), (3.14), and (3.15) [C2]. The validation outcomes are presented in Figure 3.7. To emulate grid faults, a deliberate grid voltage drop is introduced at 2s, enabling the observation of transient dynamics over a duration of 4s. The comparison between the EMT simulation and calculation results, as depicted in Figure 3.7, demonstrates an agreement in both the A-RCI and R-RCI modes for stable and unstable scenarios [C2]. Hence, the developed large-signal model can be effectively employed to assess the system's transient stability [C2]. It is important to acknowledge that minor deviations between the simulation and calculation are acceptable, given that the fast dynamics of the current control loop are not considered in the theoretical calculation [C2].

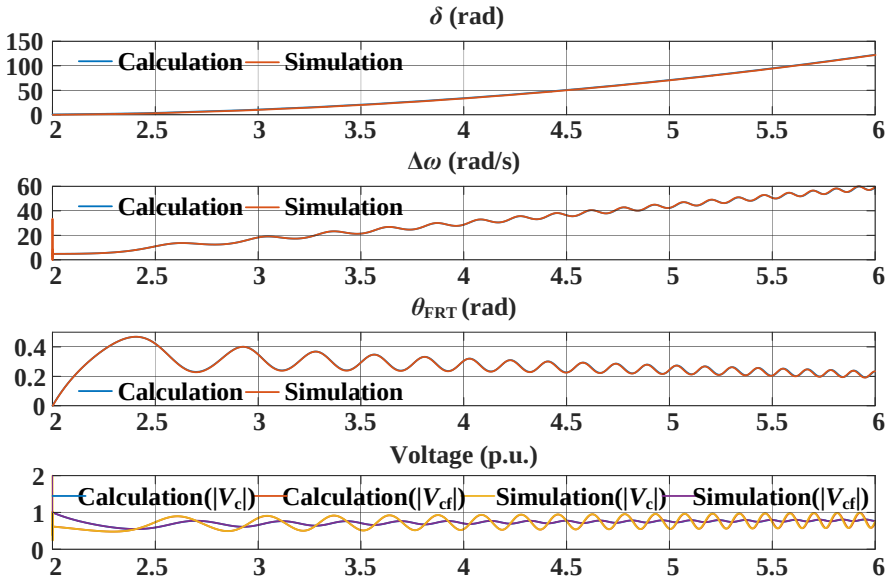

(a)

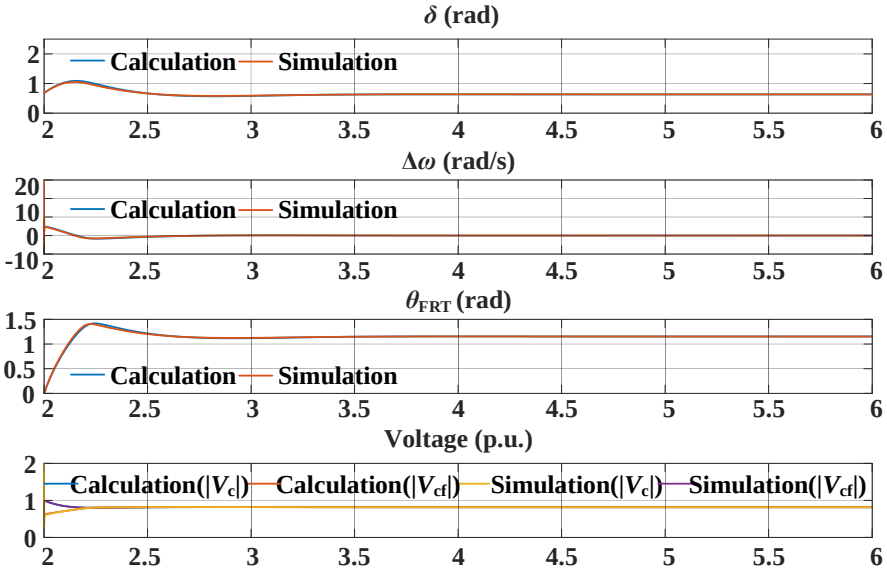
δ (rad)
Calculation
Simulation
Δω (rad/s)
Calculation
Simulation
θFRT (rad)
Calculation
Simulation
Voltage (p.u.)
Calculation(|Vc|)
Calculation(|Vcf|)
Simulation(|Vc|)
Simulation(|Vcf|)

(b)

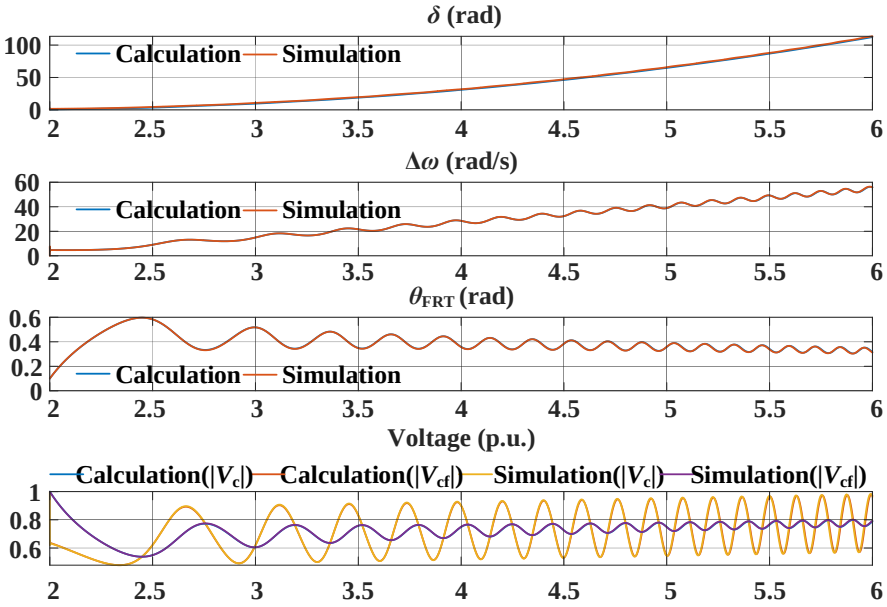
δ (rad)
Calculation
Simulation
Δω (rad/s)
Calculation
Simulation
θFRT (rad)
Calculation
Simulation
Voltage (p.u.)
Calculation(|Vc|)
Calculation(|Vcf|)
Simulation(|Vc|)
Simulation(|Vcf|)

(c)

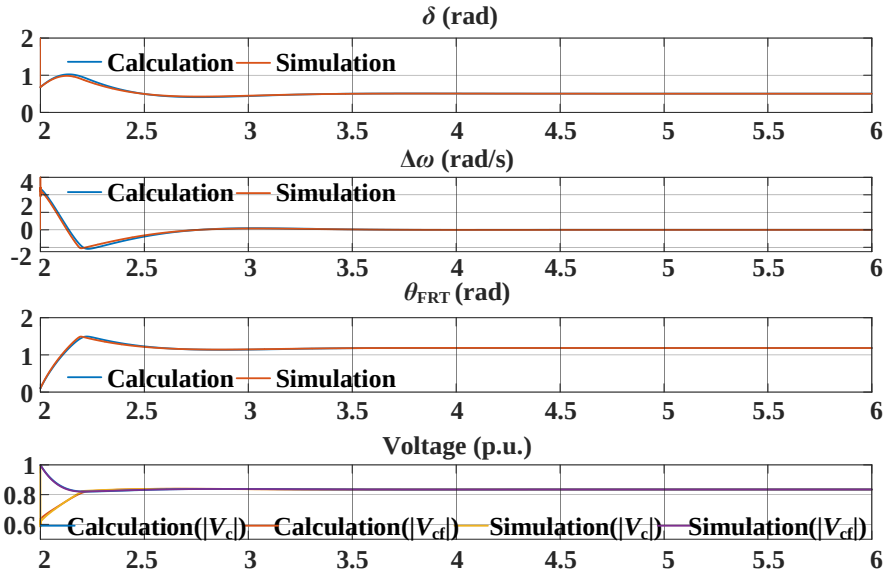

(d)

Figure 3.7. Cross validation results. (a) A-RCI mode (K=1, I_{refqb}= 0 p.u.). (b) A-RCI mode (K=5, I_{refqb}= 0 p.u.). (c) R-RCI mode (K=1, I_{refqb}=−0.1 p.u.). (d) R-RCI mode (K=5, I_{refqb}=−0.1 p.u.). Source:[C2].

3.5. CASE STUDIES AND DISCUSSION

The case studies in this chapter utilize the parameters specified in Table 3.1. The objective of case studies is to examine the existence of EPs and investigate the transient dynamics during FRT conditions by employing various reactive current injection modes, which will be elaborated in this section [C2].

Table 3.1. Parameters list. Source:[C2].

Symbol	Description	Value (p.u.)
I_{lim}	Rating current of VSC	20.00 A (1.00 p.u.)
L_g	Grid inductance	32.19 mH (0.65 p.u.)
R_g	Grid resistance	2.50 Ω (0.16 p.u.)

Table 3.1 Parameters list, continued. Source:[C2].

Symbol	Description	Value (p.u.)
V_{gs}	Grid voltage magnitude during steady state	311.13 V (1.00 p.u.) for capacitive-reactive current injection
		349.11 V (1.12 p.u.) for inductive-reactive current injection
V_g	Residual grid voltage magnitude	62.23 V (0.20 p.u.)
K_p	Proportional gain of PLL	0.012
K_i	Integral gain of PLL	0.026
$\|V_{cn}\|$	Rating magnitude of PoC voltage	311.13 V (1.00 p.u.)
ω_g	Nominal grid frequency	100π rad/s
SCR	Short circuit ratio during steady state	1.50
K	*K*-factor of FRT curves	1 to 5
I_{refqb}	Reactive current reference bias	2A (0.1 p.u.)
ω_p	Cut-off frequency of LPF for magnitude detection	2π rad/s

3.5.1. ANALYSIS ON EXISTENCE OF EPS

Figure 3.8 presents the V_{gimq}-δ curves and $V_g\sin\delta$ curve for different *K*-factors, showcasing both the A-RCI and R-RCI modes [C2]. As discussed in section 3.3, the intersection between V_{gimq}-δ curves and $V_g\sin\delta$ curve is more likely to occur when I_{refqb} is more negative, increasing the likelihood of the existence of EPs. The graphical representation in Figure 3.8 confirms this statement. The existence of EPs

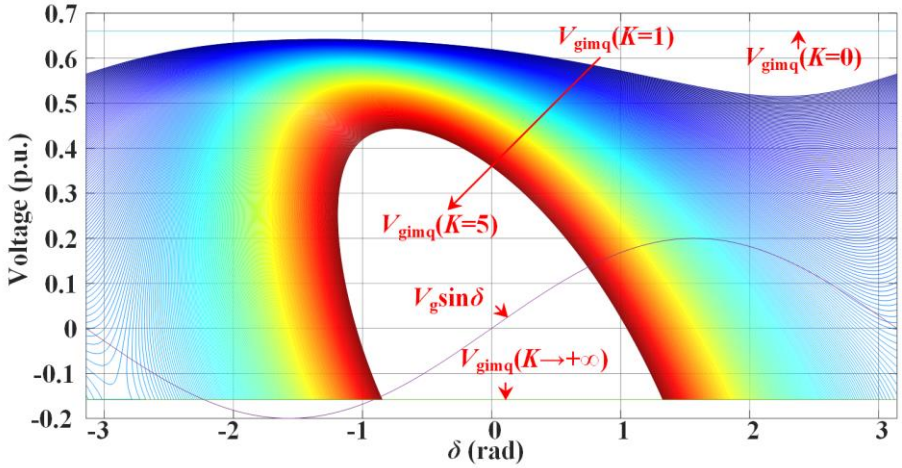
$V_{gimq}(K=1)$
$V_{gimq}(K=0)$
$V_{gimq}(K=5)$
$V_g \sin\delta$
$V_{gimq}(K\to+\infty)$
Voltage (p.u.)
δ (rad)

(a)

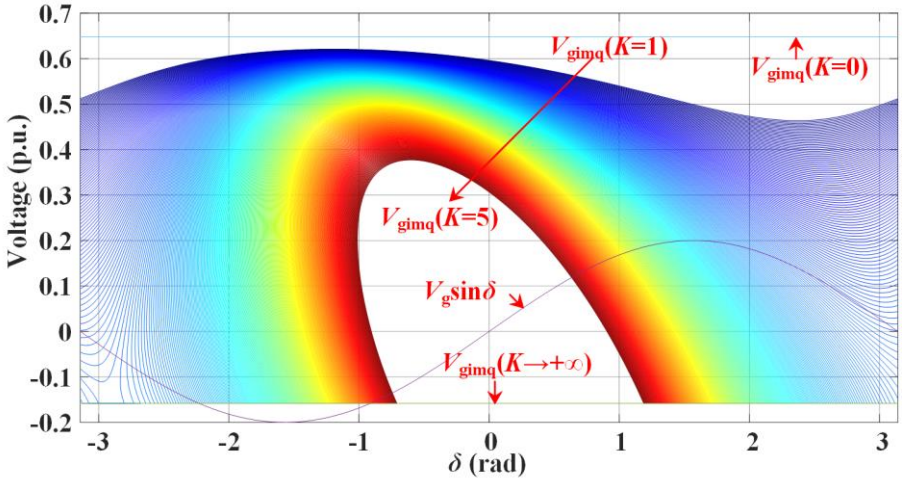
$V_{gimq}(K=1)$
$V_{gimq}(K=0)$
$V_{gimq}(K=5)$
$V_g \sin\delta$
$V_{gimq}(K\to+\infty)$
Voltage (p.u.)
δ (rad)

(b)

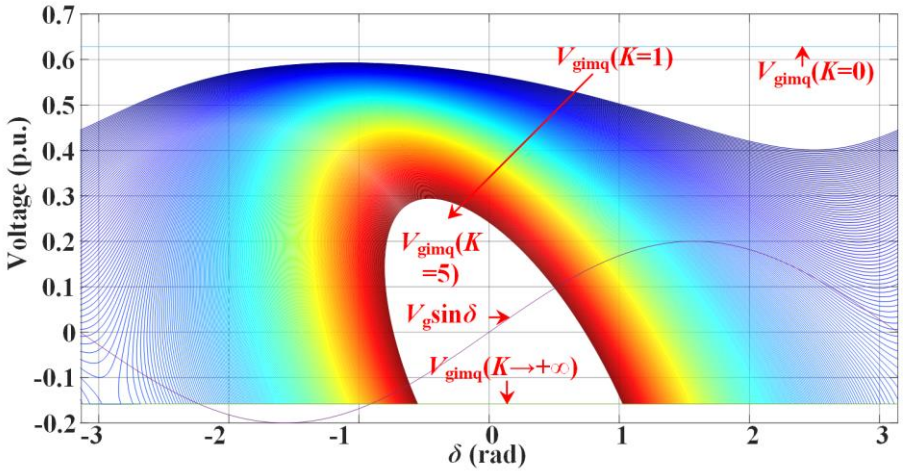

(c)

Figure 3.8. V_{gimq}-δ curve and $V_g \sin\delta$ curves (K from 1 to 5). (a) R-RCI (I_{refqb}=0.1 p.u.). (b) A-RCI (I_{refqb}=0 p.u.). (c) R-RCI (I_{refqb}=−0.1 p.u.). Source:[C2].

requires a minimum K-factor of 2 in the R-RCI (I_{refqb}=0.1 p.u.) mode, 1.8 in the A-RCI (I_{refqb}=0 p.u.) mode, and 1.7 in the R-RCI (I_{refqb}=−0.1 p.u.) mode [C2]. Hence, for enhanced transient stability of the system, it is advisable to employ the R-RCI mode when the GFL-VSC operates with capacitive-reactive current injection during normal operation, and the A-RCI mode when the GFL-VSC operates with inductive-reactive current injection during normal operation [C2].

3.5.2. TRANSIENT DYNAMICS EVALUATION

The existence of EPs is solely an essential requirement for ensuring the transient stability of the system [C2]. The ability of the system to reach and converge to EPs during grid faults depends on its transient dynamics performance, which are assessed in the following analysis. To assess the transient dynamics of the system, a grid voltage drop is intentionally introduced at 2s, and the observation period spans 4s [C2]. The calculation of transient dynamics' trajectory is conducted using the large-signal model introduced in section 3.4, and the obtained results are depicted in Figure 3.9 for both A-RCI and R-RCI modes [C2]. Based on the calculations, two key points can be drawn [C2]:

- The reactive current injection modes have impact on the initial state of the system's transient dynamics. This effect is demonstrated in Figure 3.9, where different modes of operation result in zero, positive, and negative initial values of θ_{FRT}. Specifically, the A-RCI mode (I_{refqb}= 0 p.u.) exhibits a

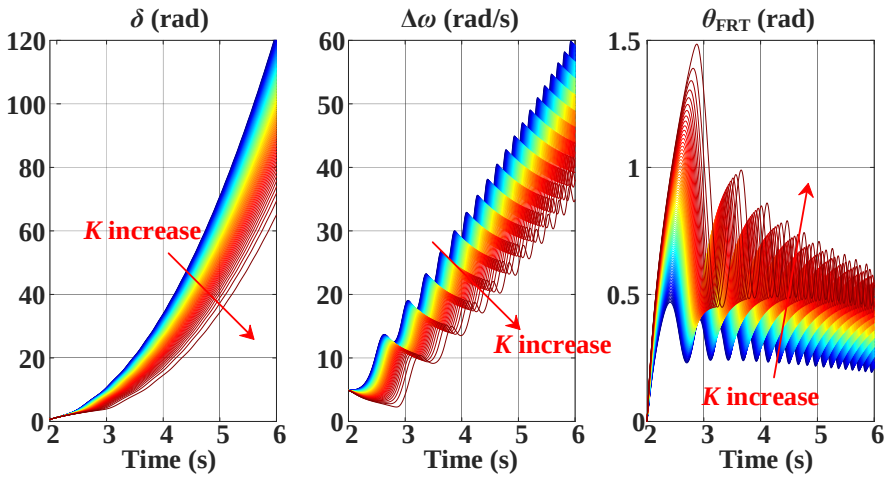
δ (rad)
Δω (rad/s)
θFRT (rad)
K increase
K increase
K increase
Time (s)
Time (s)
Time (s)

(a)

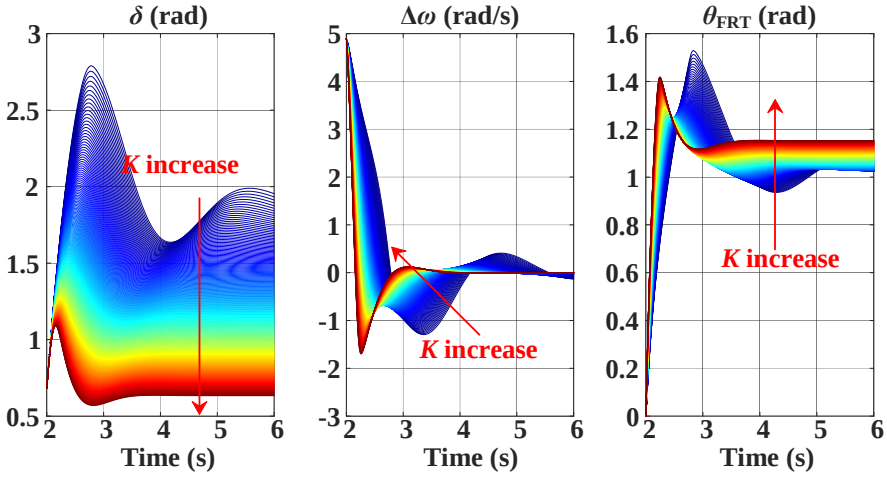
δ (rad)
Δω (rad/s)
θFRT (rad)
K increase
K increase
K increase
Time (s)
Time (s)
Time (s)

(b)

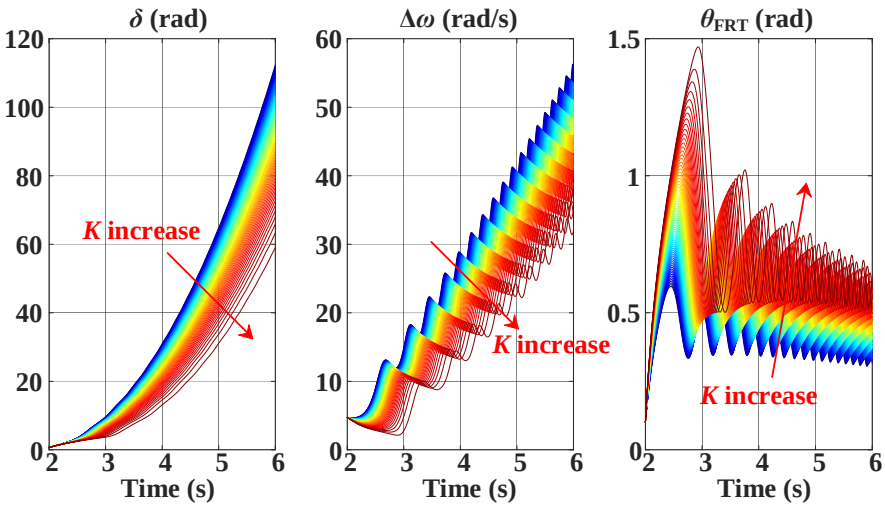
δ (rad)
Δω (rad/s)
θFRT (rad)
K increase
K increase
K increase
Time (s)
Time (s)
Time (s)

(c)

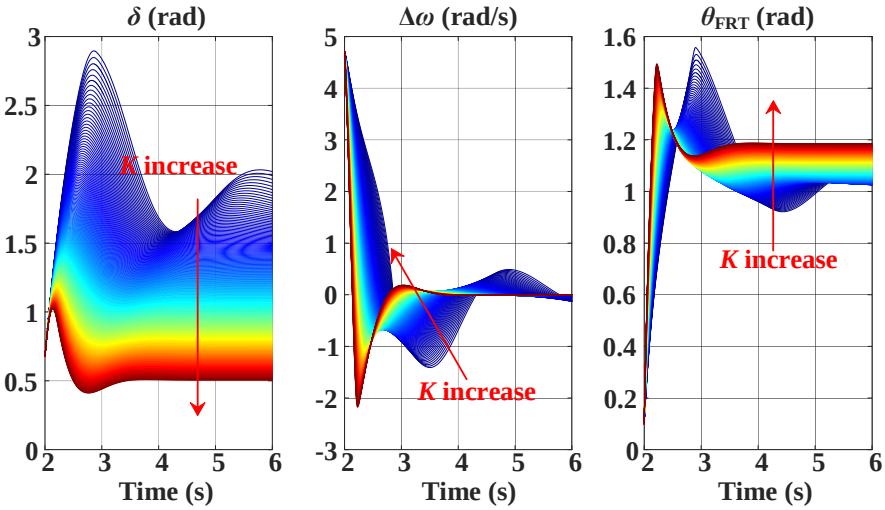
δ (rad)
Δω (rad/s)
θFRT (rad)
K increase
K increase
K increase
Time (s)
Time (s)
Time (s)

(d)

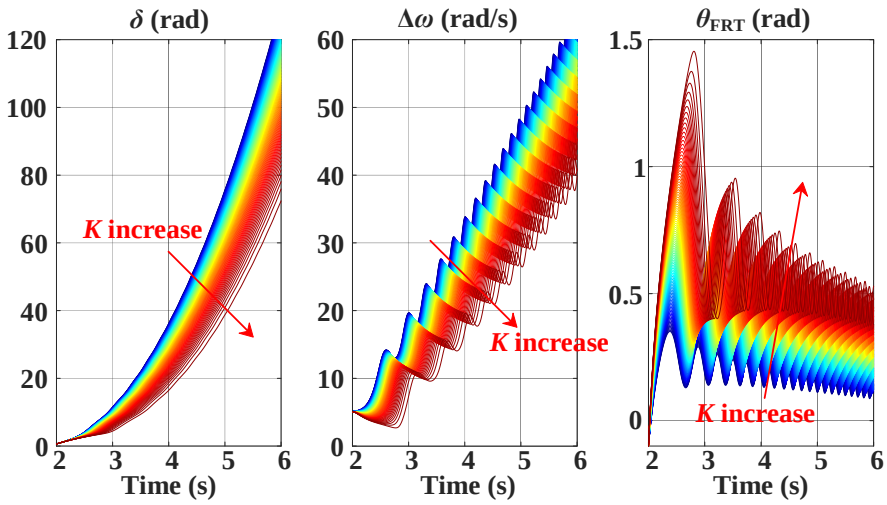

(e)

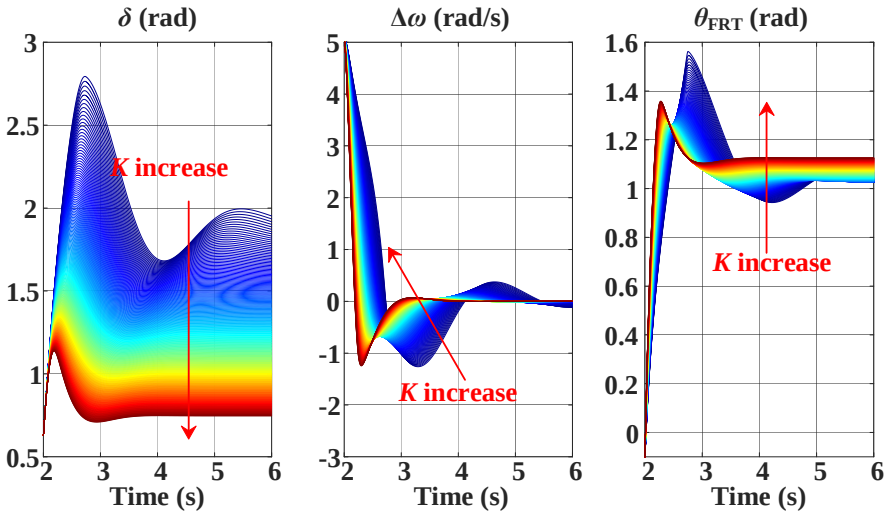

(f)

Figure 3.9. Transient dynamics. (a) A-RCI mode (K from 1 to 1.92, I_{refqb}=0 p.u.). (b) A-RCI mode (K from 2.03 to 5, I_{refqb}=0 p.u.). (c) R-RCI mode (K from 1 to 1.72, I_{refqb}=−0.1 p.u.). (d) R-RCI mode (K from 1.79 to 5, I_{refqb}=−0.1 p.u.). (e) R-RCI mode (K from 1 to 2.12, I_{refqb}=0.1 p.u.). (f) R-RCI mode (K from 2.25 to 5, I_{refqb}=0.1 p.u.). Source: [C2].

zero initial value, the R-RCI mode (I_{refqb}= −0.1p.u.) shows a positive initial value, and the R-RCI mode (I_{refqb}= 0.1p.u.) displays a negative initial value. This finding validates the applicability of the developed model in evaluating the influence of the smooth transition between normal operation and fault operation of GFL-VSC on the performance of transient dynamics.

- Furthermore, the reactive current injection modes have an impact on the minimum value of *K*-factor (denoted as $K_{minstable}$) that guarantees transient stability of the system. In Figure 3.9, $K_{minstable}$ approximates to 2.03, 1.79 and 2.25 for A-RCI mode (I_{refqb}=0p.u.), R-RCI mode (I_{refqb}=−0.1p.u.) and R-RCI mode (I_{refqb}=0.1p.u.), respectively. This suggests that the selection of the appropriate *K*-factor to ensure satisfactory dynamic performance of the system should be adjusted based on the chosen reactive current injection mode.

3.6. SUMMARY

This chapter provides an investigation into the transient stability of GFL-VSCs considering different modes of reactive current injection [C2]. To accomplish this objective, a comprehensive large-signal model incorporating the dynamics of the PLL, and current injection profile is formulated [C2]. The findings of this work demonstrate that the choice of reactive current injection mode significantly affects both the existence of EPs and the transient dynamics of GFL-VSC during FRT [C2]. Furthermore, additional case studies are conducted to validate the theoretical findings presented in this work [C2].

CHAPTER 4. TOV ANALYSIS OF GFL-VSCS DURING FAULT RECOVERY

4.1. INTRODUCTION

Many previous research on TOV analysis of grid-connected devices has concluded that the excessive capacitive-reactive current injection during grid fault recovery is the main cause of TOV [114], [115], [118], [120]-[125], and pointed out that the fast reduction of reactive current injection upon fault clearing could be the straightforward solution to mitigate TOV. However, it is important to note that the conclusion is applicable to GFL-VSCs operating as current sources (CS) during TOV analysis, where the output current can effectively track the current reference. Nevertheless, this conclusion cannot be generalized if the modulation limiter of the GFL-VSC is activated during fault recovery, indicating the operation of the GFL-VSC under the modulation saturation (MS) mode [C3]. In such cases, different considerations and analyses are required to accurately assess the TOV of the GFL-VSC.

To address the research gap, this chapter, thus, performs a comprehensive TOV analysis of GFL-VSC by considering the impact of MS. The main contributions are:

1) A rigorous calculation of the magnitude of PoC voltage (V_c) of GFL-VSC is performed under CS and MS mode. It is found out that when the GFL-VSC is operated under the MS mode, the output current cannot follow its reference. Hence, the modulation limiter primarily influences V_c, while its correlation with the current reference settings of the GFL-VSC is indirect.
2) The faster reduction of reactive current reference does not necessarily lead to a better mitigation of TOV. This is attributed to the fact that a rapid change in the current reference makes it more challenging for the accurate tracking of the reference by the output current of the GFL-VSC, leading to prolonged duration of MS and, consequently, an extended duration of TOV. Specifically, it is discovered that a high rate of change of the current reference (ROCOCR) is introduced when the current reference generation of GFL-VSC switches from FRCI mode to VDCI mode during fault recovery. This mode switching causes a longer TOV duration compared to the scenario where the current reference of GFL-VSC consistently operates in the VDCI mode.

In the end, it is suggested that the ROCOCR should be moderate to ensure a better mitigation of TOV.

4.2. SYSTEM DESCRIPTION

Figure 4.1 illustrates the system diagram of a GFL-VSC connected to a grid with inductive grid impedance. The output current (I_g) of the VSC is regulated in the SRF through the utilization of a proportional-integral (PI) controller [C3]. Synchronization between the VSC and the grid is achieved through an SRF-PLL [C3], as depicted in Figure 4.2. Basic operation of the utilized system in this chapter is same with chapter 2 and 3. Thus, similar details for system description will not be repeated hereafter. One distinction between this chapter and its preceding counterparts lies in the trigger state of the modulation limiter. The modulation limitation can be triggered when the output of current controller is large enough during dynamics, which is the focus of this chapter.

Figure 4.3 demonstrates the adjustment of the injected reactive current in GFL-VSCs during FRT, which is based on the deviation (V_c-V_{cn}) between the measured voltage magnitude (V_c) and the nominal voltage magnitude (V_{cn}) at the PoC [73], [75], [76]. Thus, the current references (I_{refd} and I_{refq}) during FRT can be expressed in (4.1) [C3].

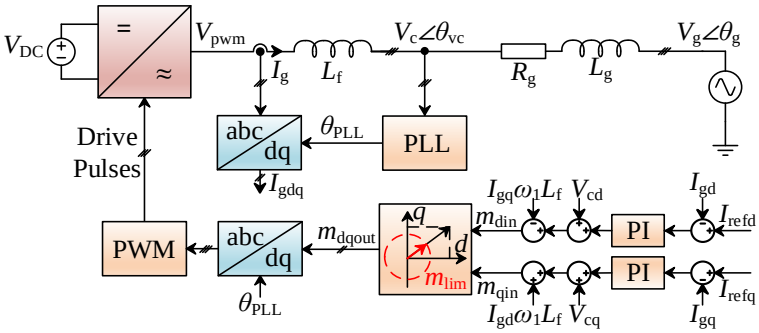

Figure 4.1. Control scheme of the GFL-VSC. Source: [C3].

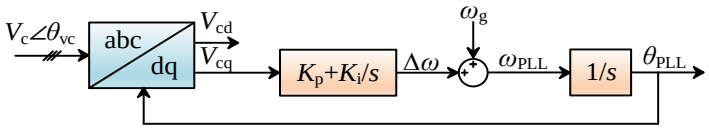

Figure 4.2. Synchronous reference frame PLL (SRF-PLL). Source: [C3].

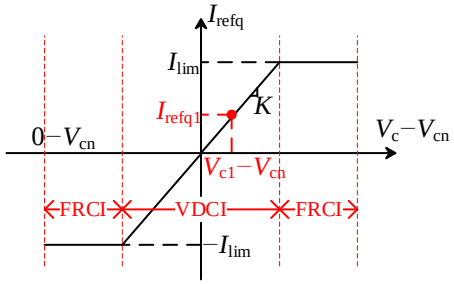

Figure 4.3. Current injection requirement [73], [75], [76].

$$I_{refq}=\begin{cases} I_{lim}, & \text{if } \dfrac{KI_{lim}}{V_{cn}}\left(V_c-V_{cn}\right)>I_{lim} \\ \dfrac{KI_{lim}}{V_{cn}}\left(V_c-V_{cn}\right), & \text{if } -I_{lim}\le\dfrac{KI_{lim}}{V_{cn}}\left(V_c-V_{cn}\right)\le I_{lim} \\ -I_{lim}, & \text{if } \dfrac{KI_{lim}}{V_{cn}}\left(V_c-V_{cn}\right)<-I_{lim} \end{cases} \tag{4.1.1}$$

$$I_{refd}=\sqrt{I_{lim}{}^2-I_{refq}{}^2} \tag{4.1.2}$$

The slope of the curve of current injection requirement in the per-unit system, known as the *K*-factor (*K*), typically ranges from 0 to 10 voltage [73], [75], [76]. The GFL-VSC has two control modes during FRT, the VDCI mode if $-I_{lim}<I_{refq}<I_{lim}$ and the FRCI mode when I_{refq} triggers the current limitation, as shown in Figure 4.3 and (4.1).

The upper and lower boundaries for the voltage magnitude (V_{cupper} and V_{clower}) that result in the switching of control modes can be determined using (4.1), which is expressed as (4.2) [C3].

$$V_{cupper}=\left(1+\frac{1}{K}\right)V_{cn}, \tag{4.2.1}$$

$$V_{clower}=\left(1-\frac{1}{K}\right)V_{cn}. \tag{4.2.2}$$

The detection of voltage magnitude is commonly achieved using a first-order LPF in practical applications, which is given in (4.3) [C3].

$$V_{cf}=\frac{s}{s+2\pi f_c}V_c \tag{4.3}$$

In (4.3), the filtered PoC voltage magnitude and the cut-off frequency of the VMDF is represented by V_{cf} and f_c, respectively. The value of V_{cf} is used to modify the injected reactive current, rather than V_c in (4.1). Therefore, the VMDF dynamics would affect the dynamics of current reference update during the fault recovery.

Figure 4.4 illustrates the vector diagram of the VSC-grid system during FRT, which formulates the physical quantities within the system in a graphical representation.

There are two operation modes of GFL-VSCs, which result in different equivalent circuit:

CS mode. Under the assumption of the current loop having a much higher control bandwidth compared to the PLL, it is reasonable to consider ideal tracking current reference, i.e., $I_{gd}=I_{refd}$, $I_{gq}=I_{refq}$, provided that the modulation limiter remains inactivated [57]. In this scenario, the GFL-VSC can be considered as a regulated current source, where its output current accurately tracks the specified current reference settings, as depicted in Figure 4.5 [57].

MS mode. The assumption on the idealized current control loop no longer holds in the event of activation of the modulation limiter, leading to changes in the equivalent circuit, as demonstrated in Figure 4.6 (L_f represents the filter inductance) [C3]. The principle of vector limitation of modulation reference is depicted in Figure 4.7. The output magnitude of the modulation limiter (m_{out}) is restricted to the dashed line circle with a corresponding radius of m_{lim}, in situations where the input magnitude of the modulation limiter (m_{in}) exceeds its limit.

The *dq*-axis component of the unlimited modulation vector is represented by m_{dqin}, whereas m_{dqout} refers to the *dq*-axis component of the limited modulation vector. The angle between the *d*-axis and the modulation vector is denoted by θ_m [C3].

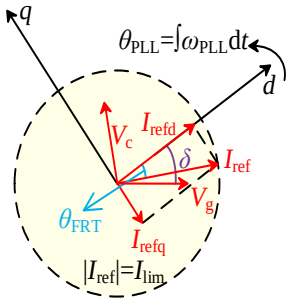

Figure 4.4. Vector diagram of physical quantities of GFL-VSC system during FRT. Source: [C3].

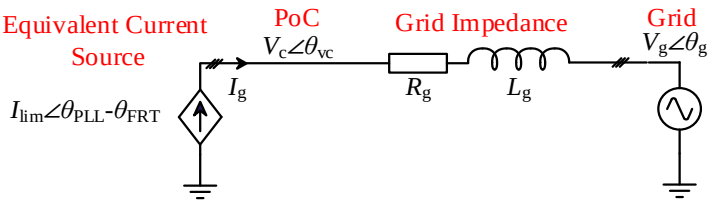

Figure 4.5. Equivalent circuit of the GFL-VSC system under CS mode. Source: [C3].

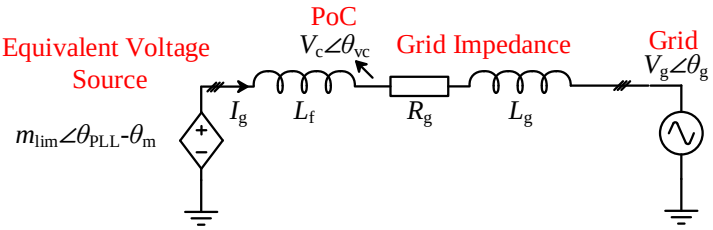

Figure 4.6. Equivalent circuit of the GFL-VSC system under MS mode. Source: [C3].

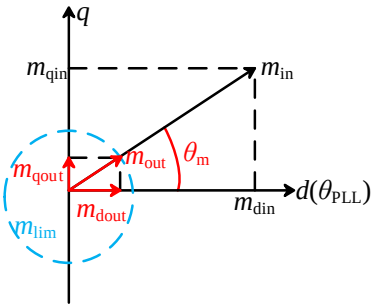

Figure 4.7. Vector limitation of modulation reference. Source: [C3].

4.3. TOV ANALYSIS

4.3.1. MAGNITUDE OF POC VOLTAGE UNDER DIFFERENT OPERATION MODES OF THE GFL-VSC

To compute the voltage magnitude at PoC, the power angle and the current injected by the VSC are utilized to express $V_{cd}(t)$ and $V_{cq}(t)$, as illustrated in (4.4) [C3].

$$V_{cd}(t) = V_g \cos\delta(t) + R_g I_{gd}(t) - \omega_{PLL}(t) L_g I_{gq}(t) + L_g \frac{dI_{gd}(t)}{dt} \qquad (4.4.1)$$

$$V_{\mathrm{cq}}(t) = -V_{\mathrm{g}}\sin\delta(t) + R_{\mathrm{g}} I_{\mathrm{gq}}(t) + \omega_{\mathrm{PLL}}(t) L_{\mathrm{g}} I_{\mathrm{gd}}(t) + L_{\mathrm{g}} \frac{\mathrm{d}I_{\mathrm{gq}}(t)}{\mathrm{d}t} \tag{4.4.2}$$

The relationship between m_{out} and V_{c} can be formulated as (4.5) [C3].

$$m_{\mathrm{dout}}(t) = -\omega_{\mathrm{PLL}}(t) L_{\mathrm{f}} I_{\mathrm{gq}}(t) + L_{\mathrm{f}} \frac{\mathrm{d}I_{\mathrm{gd}}(t)}{\mathrm{d}t} + V_{\mathrm{cd}}(t) \tag{4.5.1}$$

$$m_{\mathrm{qout}}(t) = \omega_{\mathrm{PLL}}(t) L_{\mathrm{f}} I_{\mathrm{gd}}(t) + L_{\mathrm{f}} \frac{\mathrm{d}I_{\mathrm{gq}}(t)}{\mathrm{d}t} + V_{\mathrm{cq}}(t) \tag{4.5.2}$$

By considering the impact of modulation and the injected current of the VSC, V_{c} can be expressed more comprehensively by combining equations (4.4) and (4.5), as presented in (4.6) [C3].

$$V_{\mathrm{cd}}(t) = \frac{R_{\mathrm{g}} L_{\mathrm{f}}}{L_{\mathrm{g}} + L_{\mathrm{f}}} I_{\mathrm{gd}}(t) + \frac{L_{\mathrm{g}}}{L_{\mathrm{g}} + L_{\mathrm{f}}} m_{\mathrm{dout}}(t) + \frac{L_{\mathrm{f}} V_{\mathrm{g}}}{L_{\mathrm{g}} + L_{\mathrm{f}}} \cos\delta(t) \tag{4.6.1}$$

$$V_{\mathrm{cq}}(t) = \frac{R_{\mathrm{g}} L_{\mathrm{f}}}{L_{\mathrm{g}} + L_{\mathrm{f}}} I_{\mathrm{gq}}(t) + \frac{L_{\mathrm{g}}}{L_{\mathrm{g}} + L_{\mathrm{f}}} m_{\mathrm{qout}}(t) - \frac{L_{\mathrm{f}} V_{\mathrm{g}}}{L_{\mathrm{g}} + L_{\mathrm{f}}} \sin\delta(t) \tag{4.6.2}$$

This research work employs an inductive grid impedance. As a result, the impact of the coefficient of the injected current terms ($R_{\mathrm{g}}L_{\mathrm{f}}/L_{\mathrm{g}}+L_{\mathrm{f}}$) is deemed negligible when compared to the coefficients of the modulation terms ($L_{\mathrm{g}}/L_{\mathrm{g}}+L_{\mathrm{f}}$) and grid voltage terms ($L_{\mathrm{f}}V_{\mathrm{g}}/L_{\mathrm{g}}+L_{\mathrm{f}}$) [C3]. Consequently, it is feasible to disregard the effect of injected current terms ($R_{\mathrm{g}}L_{\mathrm{f}}I_{\mathrm{gdq}}(t)/L_{\mathrm{g}}+L_{\mathrm{f}}$) when estimating the magnitude of TOV, as stated in (4.7) [C3].

$$\begin{aligned} V_{\mathrm{c}}(t) &= \sqrt{V_{\mathrm{cd}}^{\,2}(t) + V_{\mathrm{cq}}^{\,2}(t)} \\ &\approx \sqrt{\left(\frac{L_{\mathrm{g}}}{L_{\mathrm{g}}+L_{\mathrm{f}}} m_{\mathrm{out}}(t)\right)^2 + \left(\frac{L_{\mathrm{f}}}{L_{\mathrm{g}}+L_{\mathrm{f}}} V_{\mathrm{g}}\right)^2 + 2\frac{L_{\mathrm{g}}}{L_{\mathrm{g}}+L_{\mathrm{f}}} m_{\mathrm{dout}}(t) \frac{L_{\mathrm{f}}}{L_{\mathrm{g}}+L_{\mathrm{f}}} V_{\mathrm{g}}\cos\delta(t) - 2\frac{L_{\mathrm{g}}}{L_{\mathrm{g}}+L_{\mathrm{f}}} m_{\mathrm{qout}}(t) \frac{L_{\mathrm{f}}}{L_{\mathrm{g}}+L_{\mathrm{f}}} V_{\mathrm{g}}\sin\delta(t)} \\ &= \sqrt{\left(\frac{L_{\mathrm{g}}}{L_{\mathrm{g}}+L_{\mathrm{f}}} m_{\mathrm{out}}(t)\right)^2 + \left(\frac{L_{\mathrm{f}}}{L_{\mathrm{g}}+L_{\mathrm{f}}} V_{\mathrm{g}}\right)^2 + 2\frac{L_{\mathrm{g}}}{L_{\mathrm{g}}+L_{\mathrm{f}}} m_{\mathrm{out}}(t) \frac{L_{\mathrm{f}}}{L_{\mathrm{g}}+L_{\mathrm{f}}} V_{\mathrm{g}}\cos\left[\theta_{\mathrm{m}}(t) - \delta(t)\right]} \end{aligned} \tag{4.7}$$

where $m_{\mathrm{out}}(t)$ in (4.7) can be expressed by its dq-axis components in (4.8) [C3].

$$m_{\mathrm{out}}(t) = \sqrt{m^2{}_{\mathrm{dout}}(t) + m^2{}_{\mathrm{qout}}(t)} \tag{4.8}$$

For CS mode, $m_{\mathrm{out}} < m_{\mathrm{lim}}$ in (4.7) always holds since the modulation limiter is not triggered, which yields (4.9).

$$V_{\mathrm{c}}(t) \le \frac{L_{\mathrm{g}}}{L_{\mathrm{g}}+L_{\mathrm{f}}} m_{\mathrm{out}}(t) + \frac{L_{\mathrm{f}}}{L_{\mathrm{g}}+L_{\mathrm{f}}} V_{\mathrm{g}} < \frac{L_{\mathrm{g}}}{L_{\mathrm{g}}+L_{\mathrm{f}}} m_{\mathrm{lim}} + \frac{L_{\mathrm{f}}}{L_{\mathrm{g}}+L_{\mathrm{f}}} V_{\mathrm{g}} \tag{4.9}$$

For MS mode, $m_{\mathrm{out}}=m_{\mathrm{lim}}$ is yielded. Moreover, as the absolute value of the function $\cos(\theta_{\mathrm{m}}(t)-\delta(t))$ in (4.7) is less than or equal to 1, the upper boundary of the PoC voltage magnitude (V_{cub}) can be calculated by considering $|\cos(\theta_{\mathrm{m}}(t)-\delta(t))|\le 1$, which yields (4.10).

$$V_{\mathrm{c}}(t) \le V_{\mathrm{cub}} \approx \frac{L_{\mathrm{g}}}{L_{\mathrm{g}}+L_{\mathrm{f}}} m_{\mathrm{lim}} + \frac{L_{\mathrm{f}}}{L_{\mathrm{g}}+L_{\mathrm{f}}} V_{\mathrm{g}} \tag{4.10}$$

It is worth noting that V_{cub} can be also considered as the upper boundary of the PoC voltage magnitude under CS mode since (4.9) always holds under CS mode.

Figure 4.8 depicts the relationship between the estimated V_{cub}, derived from (4.10), and L_{g}. The results indicate that a weaker grid may increase the risk of higher TOV.

However, in previous work, the constrains $m_{\mathrm{out}}<m_{\mathrm{lim}}$ is often omitted in calculating PoC voltage magnitude together with the assumption of $I_{\mathrm{gd}}(t)=I_{\mathrm{refd}}(t)$, $I_{\mathrm{gq}}(t)=I_{\mathrm{refq}}(t)$. In such case, V_{c} can be calculated based on (4.4), which yields (4.11).

$$\begin{aligned} V_{\mathrm{c}}(t) &= \sqrt{V_{\mathrm{cd}}^{\,2}(t)+V_{\mathrm{cq}}^{\,2}(t)} \\ &= \sqrt{\left[V_{\mathrm{g}}\cos\delta(t)+R_{\mathrm{g}}I_{\mathrm{refd}}(t)-\omega_{\mathrm{PLL}}(t)L_{\mathrm{g}}I_{\mathrm{refq}}(t)+L_{\mathrm{g}}\frac{\mathrm{d}I_{\mathrm{refd}}(t)}{\mathrm{d}t}\right]^2} \\ &\quad \sqrt{+\left[-V_{\mathrm{g}}\sin\delta(t)+R_{\mathrm{g}}I_{\mathrm{refq}}(t)+\omega_{\mathrm{PLL}}(t)L_{\mathrm{g}}I_{\mathrm{refd}}(t)+L_{\mathrm{g}}\frac{\mathrm{d}I_{\mathrm{refq}}(t)}{\mathrm{d}t}\right]^2} \end{aligned} \tag{4.11}$$

(4.11) is equivalent to (4.7) if the modulation limiter is not triggered. However, when the modulation limiter is triggered, the calculation based on (4.11) would lead to an inaccurate prediction of V_{c}.

Finally, the mode switching of the GFL-VSC can be summarized in Figure 4.9. When the GFL-VSC operates with CS mode, I_{g} can track current reference. The PoC voltage in such case can be calculated based on either (4.7) or (4.11) considering the effect of current reference and grid voltage. However, when the GFL-VSC operates with MS mode, I_{g} cannot track current reference. Then, the PoC voltage can be only calculated by (4.7) considering the effect of modulation limitation and grid voltage [C3].

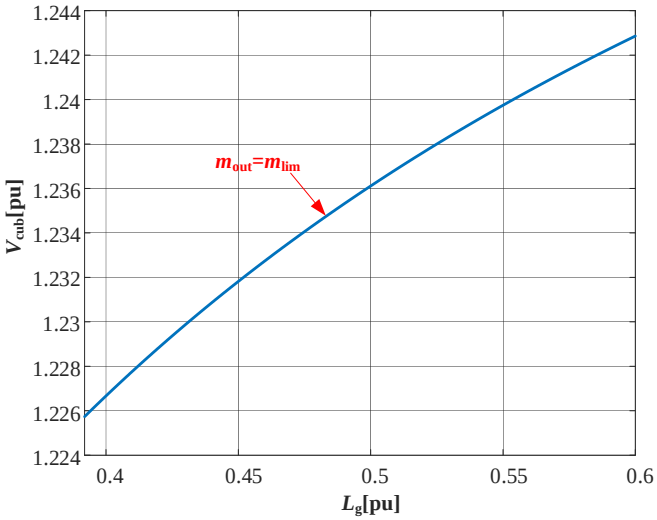

Figure 4.8. Relationship between estimated V_{cub} by (4.10) and L_g (K=3).

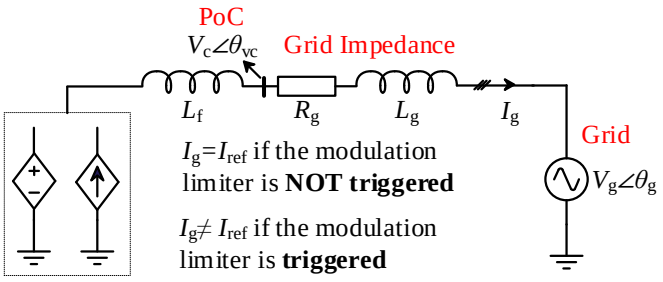

Figure 4.9. Mode switching of the GFL-VSC.

4.3.2. TOV ANALYSIS UNDER THE CASE WITH SLOW UPDATE OF CURRENT REFERENCE

Figure 4.10 depicts the voltage magnitude response of GFL-VSC at PoC and control details when the grid voltage recovers from 0.2 p.u. to 1 p.u. at 2.5s with slow update of current reference case (to emulate the slow update of current reference, f_c=0.1Hz is selected). The system parameters list in this study is shown in Table 4.1. Due to the slow update of current reference, the GFL-VSC is kept injecting excessive capacitive-reactive current during the fault recovery with I_{refd} =0 p.u. and I_{refq} = -1 p.u., which may lead to the TOV. However, it is also clear from Figure 4.10 that the modulation limiter is triggered in this scenario due to $m_{in}>m_{out}$, and hence, calculating V_c based on (4.11), i.e., without considering the modulation limiter, yields V_c =1.367 p.u. at 2.58s, which is much higher than the simulation results

where V_c =1.186 p.u. at 2.58s. In contrast, the calculation results based on (4.7) with the modulation limiter considered agree with the simulation results, as shown in Table 4.2 and Figure 4.10. The case study here further validates the necessity to consider the effect of MS on TOV during fault recovery.

4.3.3. TOV ANALYSIS UNDER THE CASE WITH FAST UPDATE OF CURRENT REFERENCE

To explore the characteristic of TOV response under fast update of current reference case, f_c is increased to 10Hz. Corresponding voltage response and control details are shown in Figure 4.11. Although the speed of voltage magnitude detection is increased, the TOV still occurs due to the unavoidable-triggered MS mode during grid fault recovery [C3]. Different from slow update response in 4.3.2, where the current reference of the GFL-VSC is kept at the FRCI mode upon the fault clearance, the effect of control mode switching from FRCI to VDCI on TOV response in Figure 4.11 also need to be considered, which is elaborated below.

4.3.3.1 Current Reference Surge Caused by Control Mode Switching

In Figure 4.11, initially, the output magnitude of the modulation limiter is constrained, as indicated by the limited m_{out} in the final set of waveforms. The current reference adheres to the FRCI mode, with I_{refd} maintained at 0 and I_{refq} kept at -1 p.u. from 2.5s to 2.502s. When V_{cf} surpasses V_{clower} (0.67p.u.), I_{refd} and I_{refq} increase with a higher rate of change of current reference (ROCOCR) than in subsequent dynamics, as shown by the blue curves in the third and fifth set of waveforms in Figure 4.11. At 2.502s, they switch to the VDCI mode. This process can be explained by differentiating (4.1) with respect to time t within the VDCI mode, which yields (4.12) [C3].

$$\frac{\mathrm{d}I_{\mathrm{refq}}(t)}{\mathrm{d}t} = \frac{KI_{\mathrm{lim}}}{V_{\mathrm{cn}}} \frac{\mathrm{d}V_{\mathrm{cf}}(t)}{\mathrm{d}t} \tag{4.12.1}$$

$$\frac{\mathrm{d}I_{\mathrm{refd}}(t)}{\mathrm{d}t} = \frac{-I_{\mathrm{refq}}(t)\dfrac{\mathrm{d}I_{\mathrm{refq}}(t)}{\mathrm{d}t}}{\sqrt{I^2_{\mathrm{lim}} - I^2_{\mathrm{refq}}(t)}} = -\frac{KI_{\mathrm{lim}}}{V_{\mathrm{cn}}} \frac{I_{\mathrm{refq}}(t)}{I_{\mathrm{refd}}(t)} \frac{\mathrm{d}V_{\mathrm{cf}}(t)}{\mathrm{d}t} \tag{4.12.2}$$

According to (4.12.2), $\mathrm{d}I_{refd}(t)/\mathrm{d}t$ is dependent on the ratio of $I_{refq}(t)$ to $I_{refd}(t)$. In the initial phase of the VDCI mode, $I_{refd}(t)$ approaches zero while $I_{refq}(t)$ approaches $-I_{lim}$, leading to an extremely high value for the ratio $I_{refq}(t)/I_{refd}(t)$. Simultaneously, $\mathrm{d}V_{cf}(t)/\mathrm{d}t$ is positive due to the current reference being switched from the FRCI mode to the VDCI mode [C3]. The combination of the very high ratio $I_{refq}(t)/I_{refd}(t)$ and the non-zero $\mathrm{d}V_{cf}(t)/\mathrm{d}t$ results in a considerable increase in $\mathrm{d}I_{refd}(t)/\mathrm{d}t$, causing a

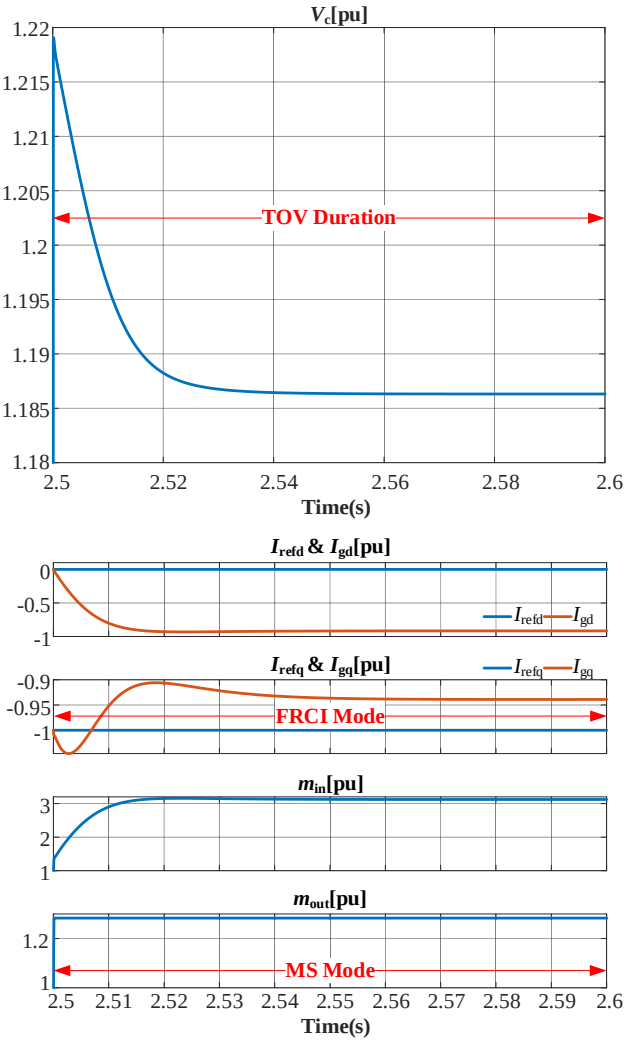

Figure 4.10. Detailed simulation waveforms with slow update of current reference (f_c=0.1Hz, K=3). Source: [C3].

surge in $I_{refd}(t)$. Additionally, $I_{refq}(t)$ also undergoes a rapid increase during this time according to (4.1) [C3].

The rapid increase in current reference leads to an extended duration of the saturated output magnitude of the modulation limiter, as depicted in Figure 4.12 [C3]. Specifically, in Figure 4.12, the moment at which the current reference surge corresponds to a transition point of increasing rate on the m_{in} waveform.

Table 4.1 Parameters in case studies. Source:[C3]

Symbol	Description	Value (p.u.)
I_{lim}	Current rating magnitude of the VSC	500 A (1.00 p.u.)
L_g	Grid inductance	3.30 mH (0.44 p.u.)
L_f	Filter inductance	0.76 mH (0.1 p.u.)
R_g	Grid resistance	0.24 Ω (0.1 p.u.)
V_{cn}	Nominal grid voltage magnitude	1200 V (1.00 p.u.)
V_{gr}	Residual grid voltage magnitude during grid fault	240 V (0.20 p.u.)
t_s	Settling time of PLL	0.1 s
ξ	Damping ratio of PLL	5
k_p	Proportional gain of PLL	0.077
k_i	Integral gain of PLL	0.071
f_{B_PLL}	Bandwidth of PLL	14.6 Hz
k_{pc}	Proportional gain of current loop controller	4.8
k_{ic}	Integral gain of current loop controller	0.096
f_{B_cc}	Bandwidth of current control loop	1000 Hz
ω_g	Nominal grid frequency	100π rad/s (1.00 p.u.)
SCR	Short circuit ratio during steady state	2.24
K	K-factor	2 or 3
f_c	Bandwidth of VMDF	0.1 or 10 Hz

Table 4.2 Comparison of V_c calculation results.

Calculation result provided by (4.7)	Calculation result provided by (4.11)	Simulation result in Figure 4.10
1.186 p.u.	1.367 p.u.	1.186 p.u.

This transition point further results in the prolonged duration of both the MS mode and TOV [C3].

In contrast, Figure 4.13 presents comprehensive simulation results for the scenario where K=2. In this scenario, the current reference dynamics directly initiate from the VDCI mode after the grid fault clearance at 2.5s. Notably, the duration of TOV is reduced as the rapid increase of current reference is prevented.

4.3.3.2 TOV Mitigation

As highlighted in subsection 4.3.3.1, the current reference surge in the control algorithm can extend the duration of modulation limiter saturation and TOV [C3]. Therefore, alleviating the TOV may be possible by reducing the ROCOCR during MS [C3]. Figure 4.14 depicts the simulation results, corresponding to Figure 4.11, with a reduced ROCOCR (where the maximum increasing rate of I_{refd} is limited at 10 p.u./s) [C3]. Evidently, the duration of TOV in Figure 4.14 is shorter, thereby validating the feasibility of adjusting ROCOCR in the control algorithm to mitigate TOV [C3].

4.4. SUMMARY

This chapter investigates the transient overvoltage of GFL-VSCs during fault recovery. The analysis indicates that TOV response of GFL-VSCs is highly influenced by MS mode, under both slow and fast update of current reference scenario. Furthermore, for fast update of current reference scenario, the duration of TOV is extended by the current reference surge. Mitigating the TOV may be achievable by reducing ROCOCR [C3]. Additionally, the upper boundary of TOV can be estimated by a constant value during the MS mode to provide intuitive insight for TOV prediction [C3]. Thus, from the perspective of TOV mitigation, update of current reference with moderate speed and smooth mode switching is preferred.

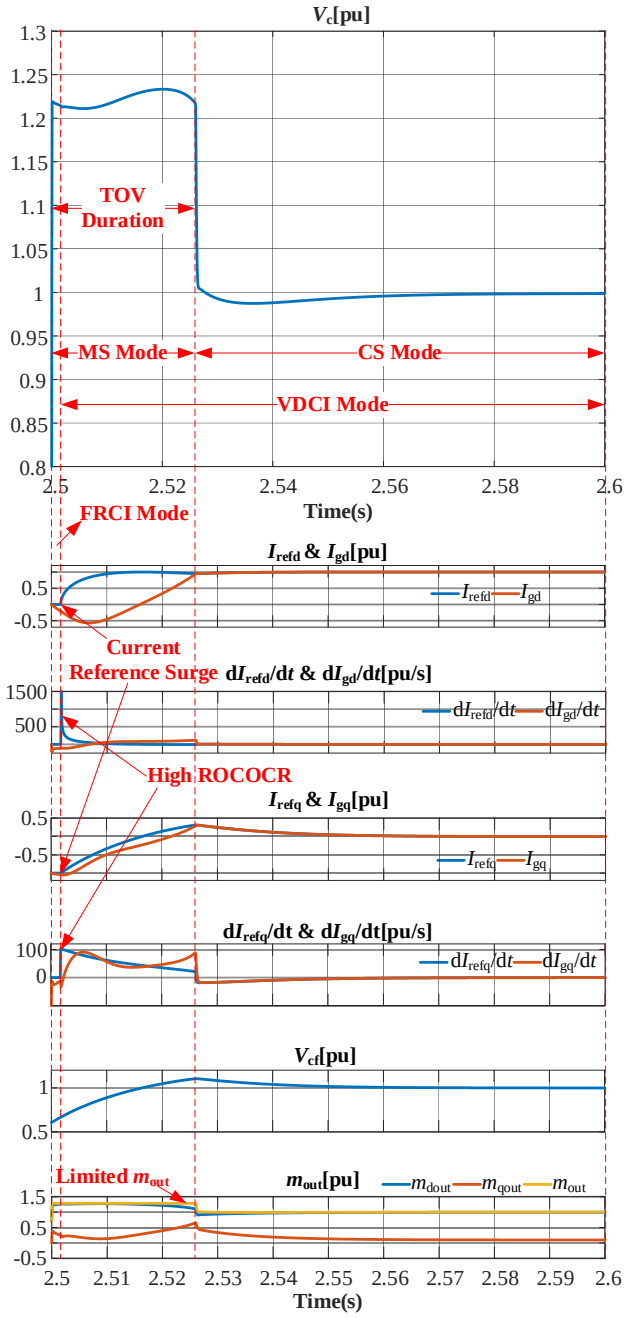

Figure 4.11. Detailed simulation waveforms from the instant of grid fault recovery to steady state to formulate current reference surge during MS mode (f_c=10Hz, K=3). Source: [C3].

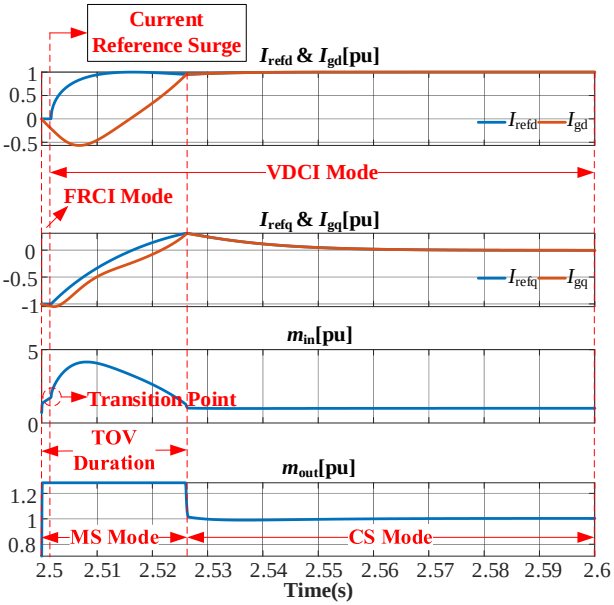

Figure 4.12. Extended TOV duration induced by current reference surge (f_c=10Hz, K=3). Source: [C3].

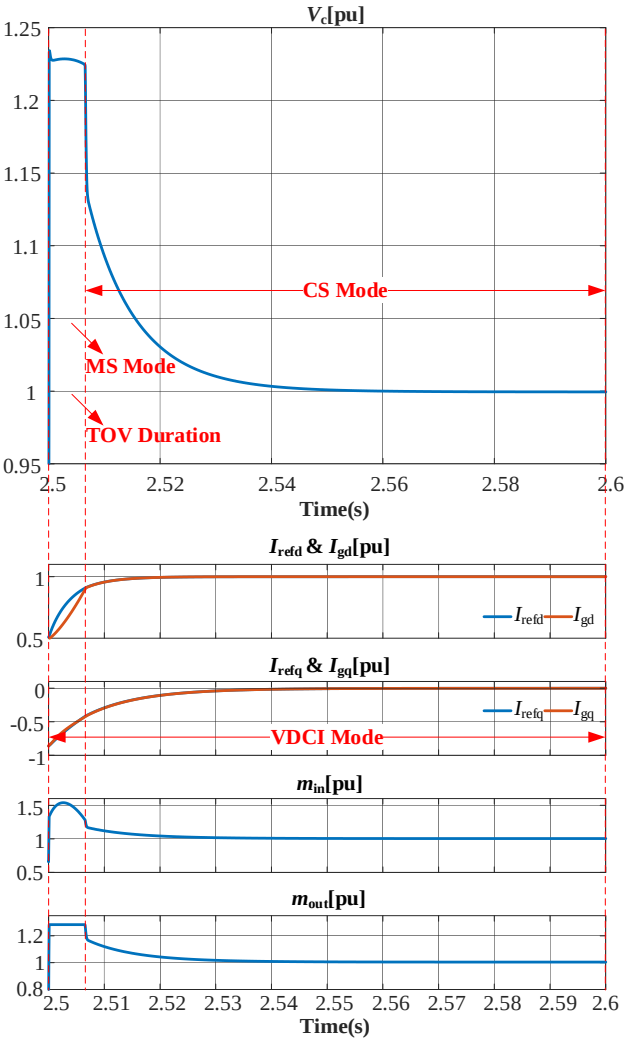

Figure 4.13. Shortened TOV duration by avoiding current reference surge (f_c=10Hz, K=2). Source: [C3].

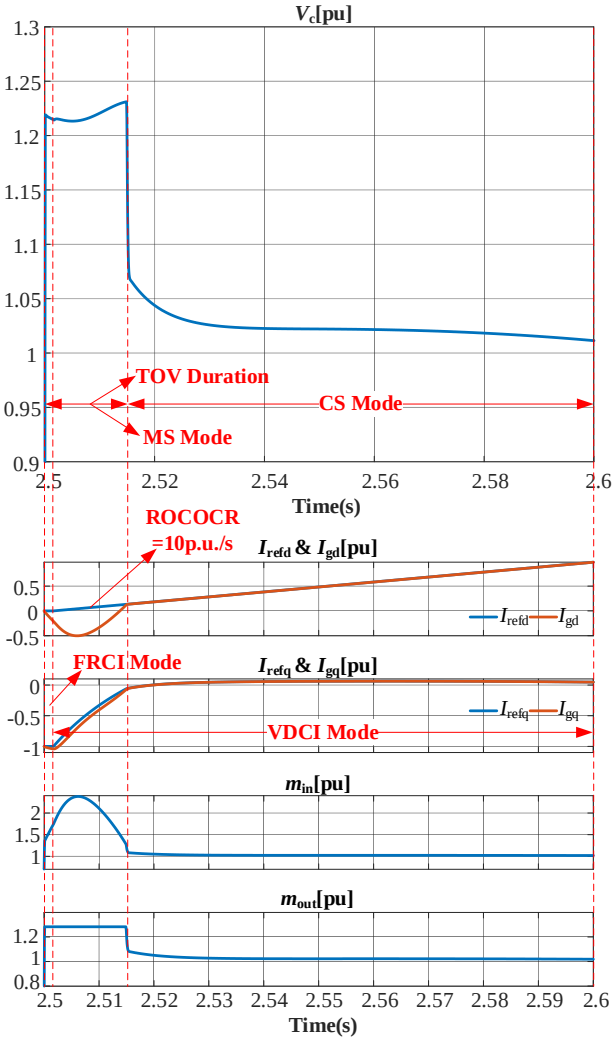

Figure 4.14. Simulation results with reduced ROCOCR (f_c=10Hz, K=3). Source: [C3].

CHAPTER 5. CONCLUSIONS AND FUTURE WORKS

5.1. CONCLUSIONS

This thesis conducted research on transient stability and overvoltage analysis of GFL-VSCs. Conclusions can be drawn as follows.

- The analysis of transient stability of GFL-VSCs under FRT conditions considering the influence of VDCI is achieved [J1], [C1]. The findings reveal that the *K*-factors employed in the VDCI algorithm have a notable influence on both the existence of EPs and the transient dynamics of the GFL-VSC during FRT [J1]. To provide insight for selecting appropriate *K*-factors ensuring the transient stability of VSCs, this study develops an analytical model of GFL-VSC that incorporates the dynamics of PLL and VDCI [J1]. The efficacy of the developed analytical model is validated through case studies involving EMT simulations and experiments, demonstrating its ability to provide accurate results for transient stability evaluation while maintaining computational efficiency.
- The investigation of the transient stability of GFL-VSCs under various reactive current injection modes is achieved [C2]. To this end, a comprehensive large-signal model is developed, incorporating the dynamics of PLL and current injection profile [C2]. The model is further utilized to assess transient stability of GFL-VSCs under various reactive current injection mode [C2]. It is revealed that the reactive current injection mode influences both the existence of EPs and the transient dynamics performance of GFL-VSC during FRT [C2]. Furthermore, the recommendation of selecting reactive current injection mode to ensure transient stability is provided [C2].
- The exploration for the TOV phenomenon in GFL-VSCs during fault recovery is achieved. The investigation reveals that the TOV is highly influenced by MS mode in both slow and fast current reference update case. It is also found that, for fast current reference update case, the duration of TOV is extended by the current reference surge caused by control mode switching [C3]. Moreover, reducing ROCOCR could potentially mitigate TOV [C3]. Theoretical findings are validated through case studies in EMT simulations.

5.2. FUTURE WORKS

Several future works based on this PhD project can be expected as below.

- The focus of this PhD project is centered on the investigation of symmetrical grid voltage sag and swell events as significant disturbances. These specific forms of disturbances have been studied to assess their impact on GFL-VSC. However, it is important to acknowledge that there are various other types of disturbances that can occur in practical grid. Examples of such disturbances include asymmetrical faults, cascaded faults, grid voltage phase jumps, and large load swings. Future research endeavors should consider these additional types of disturbances to comprehensively analyze the transient stability and overvoltage response of GFL-VSCs in diverse operational conditions.
- This PhD project focuses on a single converter-based system, but considering the cooperation of multiple converters in real power systems is important for gaining further insights into transient analysis. Understanding the interactions between multiple converters and the power grid can enhance the comprehension of system dynamics during transient events.
- This PhD project simplifies the analysis by considering an ideal grid condition, where the grid is represented by an ideal voltage source. However, for practical applications, it is necessary to model the grid side as a SG or a GFM-VSC to account for the dynamics and capture the complex interactions between the GFL-VSC and the grid. Further investigation is required to understand the mechanisms and dynamics of these complex interactions to meet the operational needs of real-world scenarios.
- The focus of this PhD project is on the synchronization stability of GFL-VSCs specifically under voltage sag conditions. However, in real power systems, ensuring system reliability requires considering not only synchronization stability but also voltage and frequency stability. Therefore, it is crucial to investigate various types of stability issues in future research to comprehensively address the stability challenges faced by GFL-VSCs in practical power systems.

REFERENCES

[1] F. Blaabjerg, Y. Yang, K.A. Kim, and J. Rodriguez, "Power electronics technology for large-scale renewable energy generation," *Proc. IEEE*., vol. 111, no. 4, pp. 335-355, Apr. 2023.

[2] Y. Lin, et al, "Pathways to the next-generation power system with inverterbased resources: Challenges and recommendations," *IEEE Electrific. Mag*., vol. 10, no. 1, pp. 10–21, Mar. 2022.

[3] D. Ramasubramanian, "Differentiating between plant level and inverter level voltage control to bring about operation of 100% inverter based resource grids," *Electric Power Syst. Res.*, vol. 205, 2022, Art. no. 107739.

[4] F. Blaabjerg, Y. Yang, D. Yang, and X. Wang, "Distributed power generation systems and protection," *Proc. IEEE.*, vol. 105, no. 7, pp. 1311–1331, Jul. 2017.

[5] M. O'Malley, et al, ''Enabling power system transformation globally: A system operator research agenda for bulk power system issues,'' *IEEE Power Energy Mag*., vol. 19, no. 6, pp. 45–55, Nov. 2021.

[6] D. B. Rathnayake, et al., "Grid forming inverter modeling, control, and applications," *IEEE Access*., vol. 9, pp. 114781–114807, Aug. 2021.

[7] J. Matevosyan, et al, "Grid-forming inverters: Are they the key for high renewable penetration?," *IEEE Power Energy Mag*., vol. 17, no. 6, pp. 89–98, Nov./Dec. 2019.

[8] A. Tuckey and S. Round, "Grid-forming inverters for grid-connected microgrids: Developing "good citizens" to ensure the continued flow of stable, reliable power," *IEEE Electrific. Mag*., vol. 10, no. 1, pp. 39–51, Mar. 2022.

[9] G. Custer, "Inverter protection and ride-through: Today's photovoltaic and energy storage inverters," *IEEE Electrific. Mag*., vol. 9, no. 2, pp. 43–49, June. 2021.

[10] Y. Lin, et al., "Research roadmap on grid-forming inverters," National Renewable Energy Lab (NREL), Golden, CO (U. S.), Tech. Rep. No. NREL/TP-5D00-73476, 2020.

[11] S. Xu, Y. Xue, and L. Chang, "Review of power system support functions for inverter-based distributed energy resources- standards, control algorithms, and trends," *IEEE Open J. Power Electron*., vol. 2, pp. 88–105, Feb. 2021.

[12] Y. Li, Y. Gu, and T. Green, “Revisiting grid-forming and grid-following inverters: A duality theory,” *IEEE Trans. Power Syst*., vol. 37, no. 6, pp. 4541-4554, Nov. 2022.

[13] R. W. Kenyon, et al., “Stability and control of power systems with high penetrations of inverter-based resources: An accessible review of current knowledge and open questions,” *Solar Energy*, vol. 210, pp. 149–168, Nov. 2020.

[14] S. Peyghami, et al., “The role of power electronics in modern energy system integration,” Foundations and Trends® in Electric Energy Systems, 5(1), pp.1-74, 2022.

[15] G. Buticchi1, et al., “The role of renewable energy system in reshaping the electrical grid scenario,” *IEEE Open J. Ind. Electron*. Soc., vol. 2, pp. 451–468, 2021.

[16] M.-A. Evans, C. Bono, and Y. Wang, “Toward net-zero electricity in europe: What are the challenges for the power system?,” *IEEE Power and Energy Magazine*, vol. 20, no. 4, pp. 44–54, 2022.

[17] J. A. P. Lopes, et al., ‘‘The future of power systems: Challenges, trends, and upcoming paradigms,’’ *WIREs Energy Environ*., vol. 9, no. 3, pp. 1-16, May. 2020.

[18] B. S. Hodge, et al., ‘‘Addressing technical challenges in 100% variable inverter-based renewable energy power systems,’’ *WIREs Energy Environ.*, vol. 9, no. 5, pp. 1–19, Sep. 2020.

[19] Y. Gu and T. C. Green, “Power system stability with a high penetration of inverter-based resources,” *Proc. IEEE*., early access, Jun. 15, 2022, doi: 10.1109/JPROC.2022.3179826.

[20] B. Badrzadeh, N. Modi, J. Lindley, A. Jalali, and J. Lu, ‘‘Power system operation with a high share of inverter-based resources: The Australian experience,’’ *IEEE Power Energy Mag*., vol. 19, no. 5, pp. 46–55, Sep. 2021.

[21] F. Blaabjerg, R. Teodorescu, M. Liserre, and A. V. Timbus, “Overview of control and grid synchronization for distributed power generation systems,” *IEEE Trans. Ind. Electron*., vol. 53, no. 5, pp. 1398–1409, Oct. 2006.

[22] M. E. T. Souza and L. C. G. Freitas, ‘‘Power electronics for modern sustainable power systems: Distributed generation, microgrids and smart grids—A review,’’ *Sustainability.*, vol. 14, no. 6, p. 3597, Mar. 2022.

[23] R. Rosso, X. Wang, M. Liserre, X. Lu, and S. Engelken, “Grid-forming converters: Control approaches, grid-synchronization, and future trends— A review,” *IEEE Open J. Ind. Appl*., vol. 2, pp. 93–109, Apr. 2021.

[24] J. Matevosyan et al., “A future with inverter-based resources: Finding strength from traditional weakness,” *IEEE Power Energy Mag*., vol. 19, no. 6, pp. 18–28, Nov./Dec. 2021.

[25] A. Yazdaninejadi, A. Hamidi, S. Golshannavaz, F. Aminifar, and S. Teimourzadeh, “Impact of inverter-based DERs integration on protection, control, operation, and planning of electrical distribution grids,” *Electr. J*., vol. 32, no. 6, pp. 43‑56, Jul. 2019.

[26] E. Bikdeli, M.R. Islam, M.M. Rahman, and K.M. Muttaqi, “State of the art of the techniques for grid forming inverters to solve the challenges of renewable rich power grids,” *Energies.*, vol. 15, no. 5, p.1879, Mar. 2022.

[27] B. Kroposki et al., “Achieving a 100% Renewable Grid: Operating Electric Power Systems with Extremely High Levels of Variable Renewable Energy,” *IEEE Power Energy Mag*., vol. 15, no. 2, pp. 61–73, Mar. 2017.

[28] X. Zhao, L. Chang, R. Shao, and K. Spence, “Power system support functions provided by smart inverters—A review,” *CPSS Trans. Power Electron. Appl*., vol. 3, no. 1, pp. 25–35, Mar. 2018.

[29] S.E. Razavi, E. Rahimi, M.S. Javadi, A.E. Nezhad, M. Lotfi, M. Shafie-khah, and J.P. Catalão, “Impact of distributed generation on protection and voltage regulation of distribution systems: A review,” *Renewable Sustainable Energy Rev*., vol. 2019, no. 105, pp.157-167, May. 2019.

[30] K. Guerra, P. Haro, R. E. Gutiérrez, and A. Gómez-Barea, “Facing the high share of variable renewable energy in the power system: Flexibility and stability requirements,” *Appl. Energy.*, vol. 310, p. 118561, Mar. 2022.

[31] N. Mararakanye and B. Bekker, “Renewable energy integration impacts within the context of generator type, penetration level and grid characteristics,” *Renewable Sustainable Energy Rev*., vol. 108, pp. 441–451, Jul. 2019.

[32] S. C. Johnson, J. D. Rhodes, and M. E. Webber, “Understanding the impact of non-synchronous wind and solar generation on grid stability and identifying mitigation pathways,” *Appl. Energy*., vol. 262, p. 114492, Mar. 2020.

[33] R. H. Lasseter, Z. Chen, and D. Pattabiraman, "Grid-forming inverters: a critical asset for the power grid," *IEEE Trans. Emerg. Sel. Topics Power Electron*., vol. 8, no. 2, pp. 925–935, Jun. 2020.

[34] M. Talha, A. Amir, S. R. S. Raihan, and N. Abd Rahim, "Grid‐connected photovoltaic inverters with low‐voltage ride through for a residential‐scale system: A review," *Int. Trans. Electr. Energy Syst*., vol. 31, no. 10, Sep. 2020.

[35] K. S. Ratnam, K. Palanisamy, and G. Yang, "Future low-inertia power systems: Requirements, issues, and solutions - A review," *Renewable Sustainable Energy Rev*., vol. 124, p. 109773, May. 2020.

[36] R. Domínguez, M. Carrión, and G. Oggioni, "Planning and operating a renewable-dominated European power system under uncertainty," *Appl. Energy.*, vol. 258, p. 113989, Jan. 2020.

[37] N. Hosseinzadeh, A. Aziz, A. Mahmud, A. Gargoom, and M. Rabbani, "Voltage stability of power systems with renewable-energy inverter-based generators: A review," Electronics, vol. 10, no. 2, p. 115, Jan. 2021.

[38] H. Kikusato et al., "Performance evaluation of grid-following and grid-forming inverters on frequency stability in low-inertia power systems by power hardware-in-the-loop testing," *Energy Reports*, vol. 9, pp. 381–392, Mar. 2023.

[39] Pattabiraman, D., Lasseter, R.H. and Jahns, T.M, "Comparison of grid following and grid forming control for a high inverter penetration power system. *In Proc. 2018 IEEE Power & Energy Society General Meeting (PESGM)*," pp. 1-5.

[40] A. Tayyebi, D. Gross, A. Anta, F. Kupzog, and F. Dorfler, "Frequency stability of synchronous machines and grid-forming power converters," *IEEE Trans. Emerg. Sel. Topics Power Electron*., vol. 8, no. 2, pp. 1004–1018, Jun. 2020.

[41] X. Liang, H. Chai, and J. Ravishankar, "Analytical methods of voltage stability in renewable dominated power systems: A review," *Electricity*, vol. 3, no. 1, pp. 75–107, Mar. 2022.

[42] T. Liu, and, X. Wang, "Physical insight into hybrid-synchronization-controlled grid-forming inverters under large disturbances," *IEEE Trans. Power Electron*., vol. 37, no. 10, pp. 11475-11480, Oct. 2022.

[43] D. Ramasubramanian, W. Baker, J. Matevosyan, S. Pant, and, S. Achilles, "Asking for fast terminal voltage control in grid following plants could provide benefits of grid forming behavior," *IET Gener. Transm. Distrib.*, vol.17, no. 2, pp.411-426, Feb. 2022.

[44] X. Wang and F. Blaabjerg, "Harmonic stability in power electronic based power systems: concept, modeling, and analysis," *IEEE Trans. Smart Grid*., vol. 10, no. 3, pp. 2858–2870, May. 2019.

[45] L. Harnefors, X. Wang, A. Yepes, and F. Blaabjerg, "Passivity-based stability assessment of grid-connected VSCs - an overview," *IEEE Jour. Emer. Select. Top. Power Electron.*, vol. 4, no. 1, pp. 116-125, Mar. 2016.

[46] W. Du, F.K. Tuffner, K.P. Schneider, R.H. Lasseter, J. Xie, Z. Chen, and B. Bhattarai, "Modeling of Grid-Forming and Grid-Following Inverters for Dynamic Simulation of Large-Scale Distribution Systems," *IEEE Trans. Power Deliv*., vol. 36, no. 4, pp. 2035–2045, Aug. 2021.

[47] H. Gong, X. Wang, and L. Harnefors, "Rethinking Current Controller Design for PLL-Synchronized VSCs in Weak Grids," *IEEE Trans. Power Electron.*, vol. 37, no. 2, pp. 1369–1381, Feb. 2022.

[48] "April and May 2018 Fault Induced Solar Photovoltaic Resource Interruption Disturbances Report Southern California Events: April 20, 2018 and May 11, 2018 Joint NERC and WECC Staff Report," NERC, USA, Jan. 2019. [Online]. Available: www.nerc.com.

[49] "Panhandle Wind Disturbance Texas Event: March 22, 2022 Joint NERC and Texas RE Staff Report," NERC, USA, Aug. 2022. [Online]. Available: www.nerc.com.

[50] "IEEE standard for interconnection and interoperability of distributed energy resources with associated electric power systems interfaces," IEEE Std 2800 (2022): 2800-2022.

[51] "System needs and services for systems with high IBR penetration," Global Power System Transformation Consortium (G-PST): Report. [Online]. Available: https://globalpst. org/wp-content/uploads/GPST-IBR-Research-Team-System-Services-and-Needs-for-High-IBR-Networks. pdf.

[52] X. Wang, M. G. Taul, H. Wu, Y. Liao, F. Blaabjerg and L. Harnefors, "Grid-synchronization stability of converter-based resources-An overview," *IEEE Open J. Ind. Appl*, vol. 1, pp. 115-134, 2020.

[53] L. Hadjidemetriou, E. Kyriakides, and F. Blaabjerg, "An adaptive tuning mechanism for phase-locked loop algorithms for faster time performance of interconnected renewable energy sources," *IEEE Trans. Ind. Appl*., vol. 51, no. 2, pp. 1792-1804, Mar. 2015.

[54] N. Hatziargyriou. et al. "Definition and classification of power system stability-revisited & extended," *IEEE Trans. Power Syst*., vol. 36, no. 4, pp. 3271-3281, Jul. 2021.

[55] D. Dong, B. Wen, D. Boroyevich, P. Mattavelli and Y. Xue, "Analysis of phase-locked loop low-frequency stability in three-phase grid-connected power converters considering impedance interactions," *IEEE Trans. Ind. Electron*., vol. 62, no. 1, pp. 310-321, Jan. 2015.

[56] M. G. Taul, C. Wu, S. Chou and F. Blaabjerg, "Optimal controller design for transient stability enhancement of grid-following converters under weak-grid conditions," *IEEE Trans. Power Electron*., vol. 36, no. 9, pp. 10251-10264, Sept. 2021.

[57] H. Wu and X. Wang, "Design-oriented transient stability analysis of PLL-synchronized voltage-source converters," *IEEE Trans. Power Electron*., vol. 35, no. 4, pp. 3573-3589, Apr. 2020.

[58] Z. Yang, R. Ma, S. Cheng and M. Zhan, "Nonlinear modeling and analysis of grid-connected voltage-source converters under voltage dips," *IEEE Trans. Emerg. Sel. Topics Power Electron.*, vol. 8, no. 4, pp. 3281-3292, Dec. 2020.

[59] Z. Zhang, R. Schuerhuber, L. Fickert, F. Katrin, C. Guochu and Z. Yongming, "Domain of attraction's estimation for grid connected converters with phase-locked loop," *IEEE Trans. Power Syst*., vol. 37, no. 2, pp. 1351-1362, Mar. 2022.

[60] Ö. Göksu, R. Teodorescu, C. L. Bak, F. Iov and P. C. Kjær, "Instability of wind turbine converters during current injection to low voltage grid faults and pll frequency based stability solution," *IEEE Trans. Power Syst*., vol. 29, no. 4, pp. 1683-1691, Jul. 2014.

[61] J. Pei, J. Yao, R. Liu, D. Zeng, P. Sun, H. Zhang, and Y. Liu, "Characteristic analysis and risk assessment for voltage–frequency coupled transient instability of large-scale grid-connected renewable energy plants during LVRT," *IEEE Trans. Ind. Electron*., vol. 67, no. 7, pp. 5515-5530, Jul. 2020.

[62] C. Zhang, X. Cai, and Z. Li, “Transient stability analysis of wind turbines with full-scale voltage source converter,” *Proc. CSEE*, vol. 37, no. 14, pp. 4018-4026, Jul. 2017.

[63] G. Han, C. Zhang, and X. Cai, “Mechanism of frequency instability of full-scale wind turbines caused by grid short circuit fault and its control method,” *Trans. China Electrotech. Soc*., vol. 33, no. 10, pp. 2168–2174, May 2018.

[64] Q. Hu, L. Fu, F. Ma and F. Ji, “Large signal synchronizing instability of pll-based vsc connected to weak ac grid,” *IEEE Trans. Power Syst*., vol. 34, no. 4, pp. 3220-3229, Jul. 2019.

[65] X. He, H. Geng, R. Li and B. C. Pal, “Transient stability analysis and enhancement of renewable energy conversion system during LVRT,” *IEEE Trans. Sustain. Energy*, vol. 11, no. 3, pp. 1612-1623, Jul. 2020.

[66] M. G. Taul, X. Wang, P. Davari and F. Blaabjerg, “An overview of assessment methods for synchronization stability of grid-connected converters under severe symmetrical grid faults,” *IEEE Trans. Power Electron*., vol. 34, no. 10, pp. 9655-9670, Oct. 2019.

[67] J. Zhao, M. Huang, H. Yan, C. K. Tse and X. Zha, “Nonlinear and transient stability analysis of phase-locked loops in grid-connected converters,” *IEEE Trans. Power Electron*., vol. 36, no. 1, pp. 1018-1029, Jan. 2021.

[68] Z. Tian, Y. Tang, X. Zha; J. Sun, M. Huang, X. Fu, F. Liu, “Hamilton-based stability criterion and attraction region estimation for grid-tied inverters under large-signal disturbances,” *IEEE Trans. Emerg. Sel. Topics Power Electron*., vol. 10, no. 1, pp. 413-423, Feb. 2022.

[69] J. Chen, M. Liu, T. O'Donnell and F. Milano, “Impact of current transients on the synchronization stability assessment of grid-feeding converters,” *IEEE Trans. Power Syst*., vol. 35, no. 5, pp. 4131-4134, Sept. 2020.

[70] Q. Hu, L. Fu, F. Ma, F. Ji and Y. Zhang, “Analogized synchronous-generator model of PLL-based VSC and transient synchronizing stability of converter dominated power system,” *IEEE Trans. Sustain. Energy*., vol. 12, no. 2, pp. 1174-1185, Apr. 2021.

[71] C. Pan, X. Lin, X. Quan and Y. Zheng. “Transient stability analysis of grid-connected converter under remote voltage sag with reactive power compensation devices,” in *Proc. 2020 IEEE/IAS Ind and Commercial Power Syst Asia (I&CPS Asia).*, 2020, pp. 1304-1308.

[72] Technical Connection Rules for High-Voltage (VDE-AR-N 4120).[Online] Available: https://www.vde.com/en/fnn/topics/technical-connection-rules/tar-for-high-voltage.

[73] Weise, Bernd. "Impact of K-factor and active current reduction during fault-ride-through of generating units connected via voltage-sourced converters on power system stability," *IET Renew. Power Gener*., vol. 9, no. 2, pp. 25-36, Jan. 2015.

[74] S. Golestan, J. M. Guerrero and J. C. Vasquez, "Three-phase PLLs: A review of recent advances," *IEEE Trans. Power Electron*., vol. 32, no. 3, pp. 1894-1907, Mar. 2017.

[75] Requirements for Offshore Grid Connections in the Grid of TenneT TSO GmbH, 21st December 2012, Tennet.

[76] System Service Ordinance, 2009, SDLWindV. [Online] Available: http://www.ichgmbh.com/wpcontent/uploads/2016/06/doc_Deutsch_ordinance-on-system-services-by-wind-energy-plants.pdf.

[77] R. Teodorescu, M. Liserre, and P. Rodriguez, Grid converters for photovoltaic and wind power systems. John Wiley & Sons, 2011.

[78] Y. Liu, J. Yao, J. Pei, Y. Zhao, P. Sun, D. Zeng and S. Chen, "Transient stability enhancement control strategy based on improved PLL for grid connected VSC during severe grid fault, " *IEEE Trans. Energy Convers*., vol. 36, no. 1, pp. 218-229, March 2021.

[79] X. He, H. Geng, J. Xi, and J. M. Guerrero, "Resynchronization analysis and improvement of grid-connected VSCs during grid faults," *IEEE Trans. Emerg. Sel. Topics Power Electron.*, vol. 9, no. 1, pp. 438-450, Feb. 2021.

[80] W. Wang, G. M. Huang, D. Ramasubramanian, and E. Farantatos, "Transient stability analysis and stability margin evaluation of phase-locked loop synchronised converter-based generators," *IET Gener. Transm. Distrib.*, vol. 14, no. 22, pp. 5000-5010, Sep. 2020.

[81] O. Abdoli, M. Gholipour, and R. Hooshmand, "A novel method for synchronization stability enhancement of grid connected converters based on equal area criterion," *Int. J. Electr. Power Energy Syst.*, vol. 139, p. 108062, Jul. 2022.

[82] C. Zhang, X. Cai, A. Rygg, and M. Molinas, “Modeling and analysis of grid-synchronizing stability of a Type-IV wind turbine under grid faults,” *Int. J. Electr. Power Energy Syst.*, vol. 117, p. 105544, May. 2020.

[83] R. Ma, J. Li, J. Kurths, S. Cheng, and M. Zhan, “Generalized swing equation and transient synchronous stability with PLL-based VSC,” *IEEE Trans. Energy Convers*., vol. 37, no. 2, pp. 1428-1441, Jun. 2022.

[84] X. Li, Z. Tian, X. Zha, P. Sun, Y. Hu, and M. Huang, “An iterative equal area criterion for transient stability analysis of grid-tied converter systems with varying damping,” *IEEE Trans. Power Syst*., early access, Jan. 31, 2023, doi: 10.1109/TPWRS.2023.3241079.

[85] X. He, H. Geng, and S. Ma, “Transient stability analysis of grid-tied converters considering PLL’s nonlinearity,” *CPSS Trans. Power Electron. Appl*., vol. 4, no. 1, pp. 40-49, Mar. 2019.

[86] Z. Wang, L. Ding, X. Gao, G. Zhu, X. Wang, and V. Terzija, “Improved active current control scheme of wind energy conversion systems with PLL synchronization during grid faults,” *IEEE Trans. Sustain Energy*., vol. 14, no. 1, pp. 717-729, Jan. 2023.

[87] H. Wu and X. Wang, “An adaptive phase-locked loop for the transient stability enhancement of grid-connected voltage source converters,” in *Proc. IEEE Energy Convers. Congr. Expo*., 2018, pp. 5892-5898.

[88] H. Wu and X. Wang, “Transient stability impact of the phase-locked loop on grid-connected voltage source converters,” in *Proc. Int. Power Electron. Conf*., 2018, pp. 2673-2680.

[89] M. G. Taul, X. F. Wang, P. Davari, and F. Blaabjerg, “Robust fault ride through of converter-based generation during severe faults with phase jumps,” *IEEE Trans. Ind. Appl*., vol. 56, no. 1, pp. 570–583, Sep. 2019.

[90] S. Ma, H. Geng, L. Liu, G. Yang, and B. C. Pal, “Grid-synchronization stability improvement of large scale wind farm during severe grid fault,” *IEEE Trans. Power Syst*., vol. 33, no. 1, pp. 216–226, Jan. 2018.

[91] M. Z. Mansour, S. P. Me, S. Hadavi, B. Badrazadeh, A. Karimi, andB. Bahrani, “Nonlinear transient stability analysis of phase-locked loop based grid-following voltage source converters using Lyapunov’s direct method,” *IEEE Trans. Emerg. Sel. Topics Power Electron*., vol. 10, no. 3, pp. 2699–2709, Jun. 2022.

[92] Y. Zhang, C. Zhang, and X. Cai, "Large-signal grid-synchronization stability analysis of PLL-based VSCs using Lyapunov's direct method," *IEEE Trans. Power Syst.*, vol. 37, no. 1, pp. 788–791, Jan. 2022.

[93] T. Wu, Q. Jiang, M. Huang, and X. Xie, "Synchronization stability of grid-following converters governed by saturation nonlinearities," *IEEE Trans. Power Syst.*, vol. 37, no. 5, pp. 4102-4105, May. 2022.

[94] Y. Li, X. Wang, J. Guo, H. Wu, B. Zhao, S. Wang, G. Wu and T. Wang, "PLL Synchronization Stability Analysis of MMC-Connected Wind Farms Under High-Impedance AC Faults," *IEEE Trans. Power Syst.*, vol. 36, no. 3, pp. 2251-2261, May. 2021.

[95] C. He, X. He, H. Geng, H. Sun, and S. Xu, "Transient stability of low-inertia power systems with inverter-based generation," *IEEE Trans. Energy Convers.*, vol. 37, no. 4, pp. 2903-2912, Dec. 2022.

[96] J. Chen, M. Liu, H. Geng, T. O'Donnell, and F. Milano, "Impact of PLL frequency limiter on synchronization stability of grid feeding converter," *IEEE Trans. Power Syst.*, vol. 37, no. 3, pp. 2487–2490, May 2022.

[97] Y. Tang, Y. Li, Y. Lu, and J. Li, "Phase portrait-based stability region estimation for grid-connected VSC with PLL," *IET Gener. Transm. Distrib.*, vol. 17, no. 3, pp. 730‑741, Nov. 2022.

[98] Y. Xia, Z. Lv, W. Wei, and H. He, "Large-signal stability analysis and control for small-scale AC microgrids with single storage," *IEEE Trans. Emerg. Sel. Topics Power Electron.*, vol. 10, no. 4, pp. 4809-4820, Aug. 2022.

[99] J. Xu, Y. Hu, H. Qian, and S. Xie, "Delay-based phase-locked loop parameters design based on stability region of grid-connected single-phase inverter under grid voltage sags," *IEEE Trans. Ind. Electron.*, vol. 69, no. 11, pp. 11324–11334, Nov. 2022.

[100] P. Hu, Z. Chen, Y. Yu, and D. Jiang, "On transient instability mechanism of PLL-based VSC connected to a weak grid," *IEEE Trans. Ind. Electron.*, vol. 70, no. 4, pp. 3836–3846, Apr. 2023.

[101] C. Wu, X. Xiong, M. G. Taul, and F. Blaabjerg, "Enhancing transient stability of PLL-synchronized converters by introducing voltage normalization control," *IEEE J. Emerg. Sel. Top. Circuits Syst.*, vol. 11, no. 1, pp. 69–78, Mar. 2021.

[102] O. Abdoli, M. Gholipour, and R. Hooshmand, "Improving synchronization stability of grid connected converters by virtual impedance," *IET Gener. Transm. Distrib.*, vol. 15, no. 7, pp. 1136–1143, Dec. 2020.

[103] Z. Zhang, R. Schuerhuber, L. Fickert, and K. Friedl, "Study of stability after low voltage ride-through caused by phase-locked loop of grid-side converter," *Int. J. Electr. Power Energy Syst.*, vol. 129, p. 106765, Jul. 2021.

[104] J. Yang, C. K. Tse, M. Huang, and D. Liu, "Bifurcations of grid-following rectifiers and routes to voltage instability in weak ac grids," *IEEE Trans. Power Syst.*, vol. 38, no. 2, pp. 1702–1713, Mar. 2023.

[105] I. R. S. Priyamvada and S. Das, "Online assessment of transient stability of grid connected PV generator with dc link voltage and reactive power control," *IEEE Access.*, vol. 8, pp. 220606–220619, Dec. 2020.

[106] Y. Li, C. Lin, J. Hu, and J. Guo, "PLL synchronization stability of grid-connected VSCs under asymmetric ac faults," *IEEE Trans. Energy Convers.*, vol. 37, no. 4, pp. 2438–2448, Dec. 2022.

[107] Y. Li, Y. Tang, Y. Lu, F. Hua, and Z. Du, "Synchronization stability of grid-connected VSC with limits of PLL," *IEEE Trans. Power Syst.*, early access, Sep. 21, 2022, doi: 10.1109/TPWRS.2022.3208244.

[108] X. Fu, M. Huang, C. K. Tse, J. Yang, Y. Ling, and X. Zha, "Synchronization stability of grid-following VSC considering interactions of inner current loop and parallel-connected converters," *IEEE Trans. Smart Grid*., early access, Mar. 29, 2023, doi: 10.1109/TSG.2023.3262756.

[109] X. Li, Z. Wang, Y. Liu, Z. Wang, L. Zhu, L. Guo, C. Zhang, J. Zhu, and C. Wang, "The largest estimated domain of attraction and its applications for transient stability analysis of PLL synchronization in weak-grid-connected VSCs," *IEEE Trans. Power Syst.*, early access, Jul. 6, 2022, doi: 10.1109/TPWRS.2022.3188887.

[110] X.,Yi, Y. Peng, Q. Zhou, W. Huang, L. Xu, Z.J. Shen, and Z. Shuai, "Transient synchronization stability analysis and enhancement of paralleled converters considering different current injection strategies," *IEEE Trans. Sustain Energy.*, vol. 13, no. 4, pp. 1957–1968, Oct. 2022.

[111] "Odessa Disturbance Texas Events: May 9, 2021, and June 26, 2021, Joint NERC and Texas RE Staff Report" NERC, USA, Sep. 2021. [Online]. Available: www.nerc.com.

[112] "2022 Odessa Disturbance Texas Event: June 4, 2022 Joint NERC and Texas RE Staff Report" NERC, USA, Dec. 2022. [Online]. Available: www.nerc.com.

[113] "Southern California Event: October 9, 2017, Joint NERC and WECC Staff Report" NERC, USA, Feb. 2018. [Online]. Available: www.nerc.com.

[114] B. Lou, L. Wang, R. Zhang, W. Hua and J. Hu, "Emergency control strategy of PV for suppressing transient overvoltage peak in LCC-HVDC infeed power system," in *Proc. 8th Renew. Power Gener. Conf. (RPG).*, 2019, pp. 1–6.

[115] Y. Zhang, Q. Li, J. Zhang, and S. Qin, "Wind farm HVRT capability improvement based on coordinated reactive power control strategy," *J. Eng.*, vol. 2017, no. 13, pp. 756-761, Dec. 2017.

[116] Y. Li, J. Guo, X. Zhang, S. Wang, S. Ma, B. Zhao, G. Wu, and T. Wang, "Over-voltage suppression methods for the MMC-VSC-HVDC wind farm integration system," *IEEE Trans. Circuits Syst. II Express Briefs.*, vol. 67, no. 2, pp. 355-359, Feb. 2019.

[117] H. Ghoddami and A. Yazdani. "A mitigation strategy for temporary overvoltages caused by grid-connected photovoltaic systems," *IEEE Trans. Energy Convers*., vol. 30, no. 2, pp. 413-420, June. 2014.

[118] Y. Zhang, C. Mensah-Bonsu, P. Walke, S. Arora and J. Pierce. "Transient over-voltages in high voltage grid-connected PV solar interconnection," in *Proc. IEEE Power and Energy Society General Meeting.*, 2010, pp. 1-6.

[119] X. Lin, Y. Zheng, Z. Liang and Y. Kang, "The suppression of voltage overshoot and oscillation during the fast recovery process from load short-circuit fault for three-phase stand-alone inverter," *IEEE Trans. Emerg. Sel. Topics Power Electron.*, vol. 9, no. 1, pp. 858-871, Feb. 2021.

[120] J. Tu, Y. Pan, X. Lu, T. Liu, X. Xu, and J. Cai, "Mechanism analysis of transient overvoltage after large disturbance considering dynamic characteristic of wind turbine generators," In *Proc. IEEE 4th International Electrical and Energy Conference (CIEEC).*, 2021, pp. 1-6.

[121] H. Saad, and S. Dennetière, "Study on TOV after Fault Recovery in VSC based HVDC systems," In *Proc. IEEE Milan PowerTech.*, 2019, pp. 1-6.

[122] S. Xu, H. Sun, S. Wang, J. Wang and J. Bi, "Overvoltage of the power system integrated with high proportion of power electronics equipment (II) -- mechanistic analysis and factor analysis of temporary power frequency

overvoltage caused by AC fault," In *Proceeding of the CSEE.*, DOI : 10.13334/j.0258-8013.pcsee.222402.

[123] C. Yin and F. Li, "Analytical expression on transient overvoltage peak value of converter bus caused by DC faults," *IEEE Trans. Power Syst*,vol. 36, no. 3, pp. 2741-2744, May 2021.

[124] W. Liang, C. Shen, H. Sun, and S. Xu, "Overvoltage mechanism and suppression method for LCC-HVDC rectifier station caused by sending end AC faults," *IEEE Trans. Power Deliv*., early access, Jun. 17, 2022, doi: 10.1109/TPWRD.2022.3184121.

[125] X. Jin and H. Nian, "Overvoltage suppression strategy for sending ac grid with high penetration of wind power in the LCC-HVdc system under commutation failure," *IEEE Trans. Power Electron.*, vol. 36, no. 9, pp. 10265–10277, Sep. 2021.

[126] C. Zhang, M. Molinas, J. Lyu, H. Zong, and X. Cai, "Understanding the nonlinear behaviour and synchronizing stability of a grid-tied VSC under grid voltage sags," In *Proc. 8th Renewable Power Generation Conference (RPG 2019).*, 2019, pp 1-8.

ISSN (online): 2446-1636
ISBN (online): 978-87-7573-669-0

AALBORG UNIVERSITY PRESS